

ABSTRACT

Title of dissertation: TUNABLE NONLINEAR
SUPERCONDUCTING METAMATERIALS:
EXPERIMENT AND SIMULATION

Melissa Trepanier, Doctor of Philosophy, 2015

Dissertation directed by: Professor Steven M. Anlage
Department of Physics

I present experimental and numerical simulation results for two types of non-linear tunable superconducting metamaterials: 2D arrays of rf SQUIDs (radio frequency superconducting quantum interference devices) as magnetic metamaterials and arrays of Josephson junction-loaded wires as electric metamaterials.

The effective inductance of a Josephson junction is sensitive to dc current, temperature, and rf current. I took advantage of this property to design arrays of Josephson junction-loaded wires that present a tunable cutoff frequency and thus a tunable effective permittivity for propagating electromagnetic waves in a one-conductor waveguide. I measured the response of the metamaterial to each tuning parameter and found agreement with numerical simulations that employ the RCSJ (resistively and capacitively shunted junction) model.

An rf SQUID is an analogue of an SRR (split ring resonator) with the gap capacitance replaced with a Josephson junction. Like the SRR the SQUID is a resonant structure with a frequency-dependent effective permeability. The differ-

ence between the SQUID and the SRR is that the effective inductance and thus effective permeability of the SQUID can be tuned with dc and rf flux, and temperature. Individual rf SQUID meta-atoms and two-dimensional arrays were designed and measured as a function of each tuning parameter and I have found excellent agreement with numerical simulations. There is also an interesting transparency feature that occurs for intermediate rf flux values.

The tuning of SQUID arrays has a similar character to the tuning of individual rf SQUID meta-atoms. However, I found that the coupling between the SQUIDs increases the resonant frequency, decreases dc flux tuning, and introduces additional resonant modes. Another feature of arrays is disorder which suppresses the coherence of the response and negatively impacts the emergent properties of the metamaterial. The disorder was experimentally found to be mainly due to a dc flux gradient across the metamaterial. I investigated methods to recover the coherence, specifically by varying the coupling between the SQUID meta-atoms, increasing the amplitude of the applied rf flux, and increasing temperature.

In this thesis I successfully demonstrate both electric and magnetic tunable superconducting metamaterials based on the Josephson effect. The tuning of these metamaterials occurs over a larger range, on faster time scales, and with lower losses than previous tunable metamaterials.

TUNABLE NONLINEAR SUPERCONDUCTING
METAMATERIALS: EXPERIMENT AND SIMULATION

by

Melissa Trepanier

Dissertation submitted to the Faculty of the Graduate School of the
University of Maryland, College Park in partial fulfillment
of the requirements for the degree of
Doctor of Philosophy
2015

Advisory Committee:
Professor Steven M. Anlage, Chair/Advisor
Professor Thomas M. Antonsen Jr.
Professor Christopher J. Lobb
Professor Frederick C. Wellstood
Assistant Professor James R. Williams

© Copyright by
Melissa Trepanier
2015

Acknowledgments

First and foremost I would like to thank my advisor, Steven M. Anlage, for allowing me this wonderful experience and his guidance along every step. I would like to thank the members of my committee Thomas M. Antonsen, Christopher J. Lobb, Frederick C. Wellstood, James R. Williams for their time and help improving this thesis.

I would like to thank the other members of my group: Jen-Hao Yeh, Tamin Tai, John Abrahams, Stephen Remillard, Benhood Ghamsari, Bo Xiao, Bakhrom Oripov, Rahul Gogna, Seokjin Bae, Yuewen Tan, Biniyam Taddese, Ziyuan Fu, and Matt Frazier. In particular, I'd like to thank Daimeng Zhang, who has worked side-by-side with me on this project from the beginning.

I would like to thank our collaborators: Oleg Mukhanov, Masoud Radparvar and Georgy Prokopenko at Hypres for their help with understanding their process and with designing our samples; Vassili Savinov, Kaveh Delfanazari, and Nikolay Zheludev at University of Southampton for the use of their mm-wave setup and their expertise with performing those measurements; Alexey Ustinov, Philipp Jung, and Suzanne Butz at Karlsruhe Institute of Technology for the use of their samples, introducing me to Python, and productive discussion on how to simulate rf SQUIDs; V. P. Koshelets at IREE for preparing samples; Edward Ott and Tom Antonsen for discussions of coherence, the Kuramoto model, and linear eigenmodes. I would also like to thank Nikos Lazarides and George Tsironis for productive discussions and Brian Straughn and Doug Bensen for their help getting equipment working.

I'd like to thank my mother and father, Sallyann and Marc Trepanier, who have always put me (along with my brother and sister) first in their priorities, particularly when it comes to our education. I'd also like to thank my partner, Ryan Moss, for his support and tea-fetching.

This work is financially supported by the NSF-GOALI and OISE programs through grant #ECCS-1158644, and the Center for Nanophysics and Advanced Materials (CNAM). The University of Maryland supercomputing resources were made available for conducting the research reported in this thesis. I'd also like to thank H. J. Paik and M. V. Moody for use of the pulsed tube refrigerator.

Table of Contents

List of Tables	vii
List of Figures	viii
1 Background	1
1.1 Superconductivity	1
1.1.1 Fluxoid Quantization	2
1.1.2 Josephson Junctions	3
1.1.3 rf SQUIDs	6
1.2 Metamaterials	7
1.2.1 Tunable Negative Effective Permeability	9
1.2.2 Tunable Negative Effective Permittivity	12
1.2.3 Tunable Negative Index Metamaterials	14
1.3 What Follows	16
2 Model and Simulations	17
2.1 Single Josephson Junction	17
2.2 Single rf SQUID	19
2.2.1 Low rf Flux Limit	20
2.2.2 High rf Flux Limit	21
2.3 Pair of rf SQUIDs	22
2.4 rf SQUID Arrays	23
2.5 Calculating Transmission	25
2.5.1 Dissipated Power	25
2.5.2 Effective Medium	25
2.6 Quantifying Coherence in rf SQUID Arrays	28
3 Experimental Details	30
3.1 Sample Design	30
3.1.1 rf SQUIDs	30
3.1.2 JJ-loaded wire arrays	35
3.2 Sample Fabrication	36

3.2.1	Hypres Process	36
3.2.2	IREE Process	36
3.3	Measurement Setup	37
3.3.1	Microwave Path	38
3.3.2	Sample and Waveguide Mounting	40
4	Individual rf SQUID Measurements	46
4.1	Tunability with dc Flux	46
4.2	Tunability with Temperature	48
4.3	Tunability with rf Flux	51
4.4	Tuning Speed	58
4.5	Summary	59
5	rf SQUID Array Measurements	60
5.1	Pair of rf SQUIDs	60
5.2	rf SQUID Arrays	67
5.2.1	Coupling	70
5.2.2	Magneto-Inductive Modes	76
5.2.3	dc Flux Disorder	88
5.3	Summary	99
6	JJ-Loaded Wire Array Measurements	102
6.1	Low dc and rf Current	102
6.2	Beyond the Small Current Limits	106
6.3	Summary	112
7	Conclusions	113
7.1	rf SQUID Metamaterials	113
7.2	JJ-loaded Wire Array Metamaterials	115
7.3	Combined Metamaterial	117
7.4	Josephson Metamaterials in the Quantum Limit	117
A	Justification of dc Flux Gradient	119
A.1	Other Possible Forms of Disorder	119
A.2	Additional Gradient Worsens Coherence	121
A.3	Direction of dc Flux Gradient	122
B	Other Samples	125
B.1	Individual SQUIDs	125
B.2	Arrays with Low Coherence	126
B.3	SQUID Arrays: mm-Wave Free Space Measurements	128
B.4	First Generation JJ-Loaded Wire Arrays	135

C	Assigning Simulation Parameters	137
C.1	rf SQUIDs	137
C.1.1	Input Flux	137
C.1.2	Mutual and Self-Inductance	138
C.1.3	Fit Parameters	140
C.2	JJ-Loaded Wire Array	142
D	Scripts	144
E	Results for Unmodified Kuramoto Order Parameter	147
E.1	Relationship Between Transmission and Coherence	147
E.2	Pair of SQUIDs in the High rf Flux Limit	147
E.2.1	Effect of Coupling on Coherence and Transparency	148
E.2.2	Effect of Unequal dc Flux on Coherence and Transparency	150
	Bibliography	152
	Curriculum Vitae	

List of Tables

3.1	Parameters of measured SQUID and SQUID arrays	31
3.2	Layers in Hypres process	37
3.3	Layers in IREE process	38
3.4	Waveguide properties	40
6.1	Transition currents	104
B.1	Unmeasured individual rf SQUID design parameters	126
C.1	Comparison of nominal and fit values	142

List of Figures

1.1	Schematic and circuit diagram of Josephson junction	4
1.2	Circuit diagram of rf SQUID	7
1.3	Schematic and circuit diagram of SRR	10
1.4	1D and 2D Josephson junction arrays	14
1.5	Combined tunable index metamaterial	15
2.1	Circuit diagram of pair of rf SQUIDs	22
2.2	Reflected and transmitted waves in effective medium calculation	27
3.1	Individual rf SQUID meta-atom	32
3.2	11x11 and 27x27 rf SQUID arrays	33
3.3	21x21 rf SQUID arrays	34
3.4	JJ-loaded wire array	35
3.5	Microwave setup	39
3.6	Waveguides	40
3.7	Interior of cryostat	42
3.8	Waveguide clamps	43
3.9	Mount for Josephson junction-loaded wire arrays	44
3.10	Orientation of samples in the waveguide	45
4.1	dc flux tuning of individual rf SQUID	47
4.2	Flux dependence of effective permeability	49
4.3	Temperature dependence of individual rf SQUID	50
4.4	Temperature dependence of dc flux tuning of effective permeability	52
4.5	rf flux dependence of dc flux tuning of individual rf SQUID	53
4.6	rf flux tuning of individual rf SQUID	54
4.7	Hysteresis in individual rf SQUID	57
4.8	58
5.1	Comparison of resonant frequency in coupled and uncoupled SQUID pairs	61
5.2	Comparison of coherence and resonant modes in coupled and uncoupled SQUID pairs	64

5.3	Two-SQUID modes in rf high flux limit	65
5.4	Effect of coupling on range and magnitude of transparency	66
5.5	Temperature and dc flux tuning of 27x27 array	68
5.6	rf flux and dc flux tuning of 21x21 array	69
5.7	Comparison of nearest neighbor and complete coupling	71
5.8	Dependance of Q on coupling	72
5.9	Resonant frequency dependence on coupling	73
5.10	Coupling dependence of dc flux tuning of effective permeability	75
5.11	Magneto-inductive modes in arrays	77
5.12	Frequency dispersion of magneto-inductive modes	78
5.13	Frequency range of MI modes	79
5.14	Characterization of MI modes in tightly coupled array	81
5.15	Characterization of MI modes in loosely coupled array	82
5.16	Visualization of the eigenvectors	84
5.17	Coherence increases with rf flux	85
5.18	Characterization of MI modes above the low rf flux limit	86
5.19	Transmission and coherence at higher rf flux	87
5.20	Resonant modes of array on primary resonance at high rf flux	88
5.21	dc flux dependence of coherence	90
5.22	Comparison of coherence in data and simulation	92
5.23	Effective permeability as a function of coherence	93
5.24	Hysteretic transparency in 11x11 array	94
5.25	Non-hysteretic transparency in 27x27 array	95
5.26	Coherence as a function of coupling and linear dc flux gradient	96
5.27	Increased rf flux improves coherence	98
5.28	Increased temperature improves coherence	100
6.1	dc current dependence of transmission, cutoff frequency, and permit- tivity	103
6.2	Temperature dependence of transmission, cutoff frequency, and per- mittivity	105
6.3	dc voltage vs dc current	107
6.4	Size of the small voltage steps	108
6.5	Hysteretic dependence of transmission on input power and dc current	110
6.6	Intermodulation	111
7.1	Next generation of wire arrays	116
A.1	Coherence as a function of dc flux for various types of disorder	120
A.2	Increasing the flux gradient worsens coherence	123
A.3	Direction of dc flux gradient	124
B.1	Five unmeasured individual rf SQUIDs	127
B.2	Largest unmeasured individual rf SQUID	128
B.3	7x7 and 2x2 rf SQUID arrays	129
B.4	Comparison of coherence in different arrays	130

B.5	mm-wave experimental setup	132
B.6	SQUID arrays designed for mm-wave experiment	133
B.7	Predicted response for mm-wave samples	134
C.1	Coherence of magneto-inductive modes with unequal coupling in each direction	141
D.1	Symmetry in 2D array	145
E.1	Relationship between coherence and transmission	148
E.2	Effect of coupling on rf flux tuning in rf SQUID pair	149
E.3	Effect of dc flux disorder on rf flux tuning in rf SQUID pair	151

Chapter 1: Background

In this chapter, I provide the background in superconductivity and metamaterials necessary to understand the motivation of my work and its connection with previous work. The chapter begins with a discussion of the relevant macroscopic quantum effects of superconductors. I then establish the potential benefits of superconducting metamaterials and review relevant literature with a focus on tunability. Compared with other tunable superconducting metamaterials, the Josephson metamaterials I examined exhibit high speed tuning without relying on mechanisms that increase loss.

1.1 Superconductivity

There are three classic hallmarks of superconductivity: zero resistance (for dc current), perfect diamagnetism, and macroscopic quantum effects. The last of these effects is the least well-known and the most relevant for my research on superconducting metamaterials. Under many circumstances a superconductor can be described by a single macroscopic quantum wavefunction with a well-defined position-dependent amplitude and phase $\Psi = |\Psi|e^{i\theta}$ [1,2]. This wavefunction inherits the phase from the underlying microscopic BCS (Bardeen, Cooper, Schrieffer)

wavefunction describing the Cooper pairing of electrons in the metal. Two important consequences are the Josephson effect and fluxoid quantization.

1.1.1 Fluxoid Quantization

A fluxoid is defined as

$$\Phi' = \Phi + \frac{mc}{e^2} \oint \frac{\vec{J}_s \cdot d\vec{s}}{|\Psi|^2} \quad (1.1)$$

where Φ is the magnetic flux through a closed superconducting loop, m and e are the mass and charge of an electron, \vec{J}_s is the supercurrent density, and the contour is taken around the closed loop [2]. If the contour is inside the superconductor away from the currents on the surface, $\vec{J}_s = 0$ and the fluxoid is simply the flux $\Phi' = \Phi$.

Inside the superconductor the supercurrent velocity is also zero

$$m^* \vec{v}_s = \hbar \left(\nabla \theta - \frac{2\pi \vec{A}}{\Phi_0} \right) = 0 \quad (1.2)$$

where $\Phi_0 = h/2e \cong 2.07 \times 10^{-15} \text{ Tm}^2$ is the flux quantum and \vec{A} is the magnetic vector potential ($\Phi = \oint \vec{A} \cdot d\vec{s}$) [2]. From Eq. 1.2 one finds

$$\vec{A} = \frac{\Phi_0}{2\pi} \nabla \theta \quad (1.3)$$

and thus:

$$\Phi = \oint \vec{A} \cdot d\vec{s} = \frac{\Phi_0}{2\pi} \oint \nabla \theta \cdot d\vec{s} \quad (1.4)$$

Since the phase must be single-valued, integrating around a closed loop must be $0 \text{ mod } (2\pi)$ and the flux through a closed superconducting loop must be an integer number of flux quanta.

$$\Phi = n\Phi_0 \quad (1.5)$$

1.1.2 Josephson Junctions

A Josephson junction can be made from an insulating barrier sandwiched between two superconductors (Fig. 1.1 (a)) if the barrier is thin enough (\sim nm) for Cooper pairs to tunnel across the junction [2, 3]. The dynamics of the junction depend on the gauge-invariant phase difference,

$$\delta(t) = \theta_1(t) - \theta_2(t) - \frac{2\pi}{\Phi_0} \int_1^2 \vec{A}(\vec{r}, t) \cdot d\vec{l} \quad (1.6)$$

where $\vec{A}(\vec{r}, t)$ is the magnetic vector potential in the region between the superconductors, θ_1 and θ_2 are the phases of the macroscopic quantum wave function of the superconductor on either side of the junction, and the integral is on a path in the superconductor that connects the two points.

The superconducting current through the junction is given by the dc Josephson equation

$$I_J = I_c \sin \delta(t) \quad (1.7)$$

where I_c is the critical current of the junction [3].

The voltage across the junction is given by the ac Josephson equation [3],

$$V = \frac{\Phi_0}{2\pi} \frac{d\delta}{dt} \quad (1.8)$$

One implication of these two equations is that there can be a dc current through the junction even with no voltage. A dc voltage results in an ac current with frequency of $\omega_0 = 2\pi V_{dc}/\Phi_0$. This frequency is derived by integrating Eq. 1.8 and substituting into Eq. 1.7.

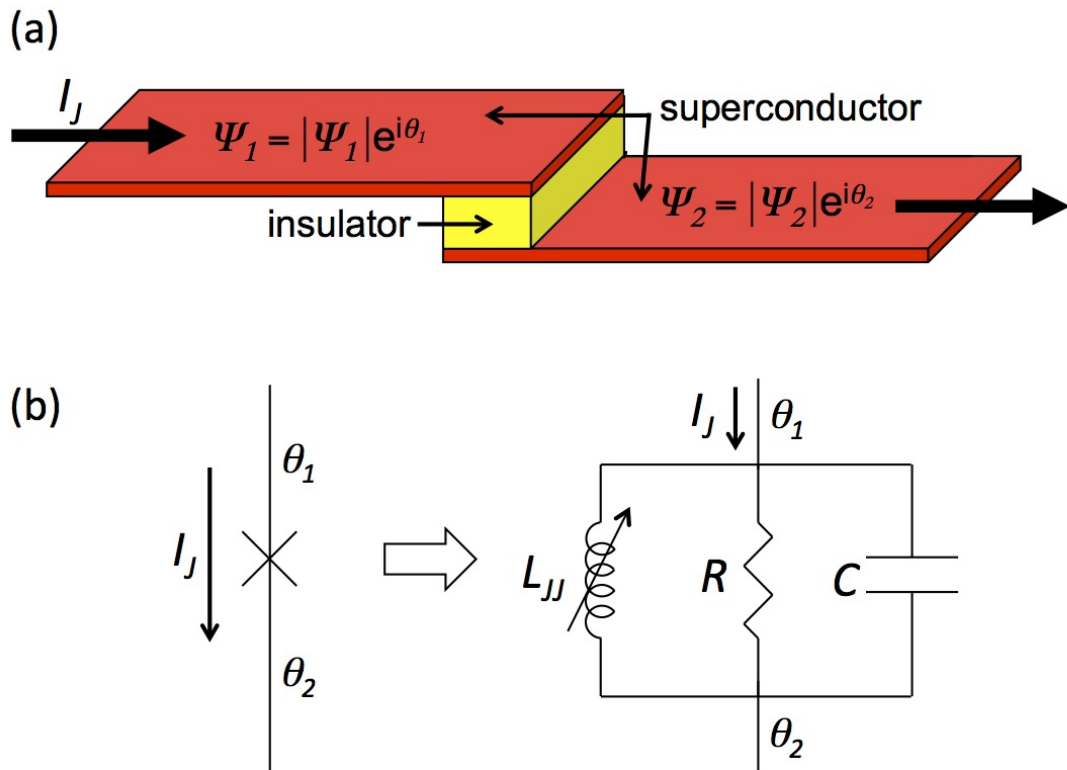


Figure 1.1: (a) Schematic of a Josephson junction. (b) Circuit diagram of a Josephson junction using the RCSJ model.

When there is an applied ac voltage $V = V_{dc} + V_{ac} \cos \omega t$, steps can appear in the dc current as a function of dc voltage; these are known as Shapiro steps [2] and are the basis for the standard volt [4]. The steps can be revealed by integrating Eq. 1.8 and substituting into Eq. 1.7. By expanding the sine of the sine in terms of Bessel functions one finds

$$I_J = I_c \sum (-1)^n J_n \left(\frac{2\pi V_{ac}}{\Phi_0 \omega} \right) \sin(\delta_0 + \omega_0 t - n\omega t) \quad (1.9)$$

where δ_0 is a constant of integration [2]. There is a contribution to the dc current when $\omega_0 = n\omega$, *i.e.* $V_{dc} = n\Phi_0\omega/2\pi$. Thus the dc current as a function of dc voltage has a series of spikes. To get true steps rather than spikes requires additional circuit elements in the analysis.

Combining the ac and dc Josephson equations (Eqs. 1.7 and 1.8) yields an expression for the inductance of the junction [1]. The time-derivative of the dc Josephson equation Eq. 1.7 is

$$\frac{dI_J}{dt} = I_c \cos \delta \frac{d\delta}{dt} \quad (1.10)$$

This equation can be solved for $d\delta/dt$ and substituted into the ac Josephson equation Eq. 1.8 to yield

$$V = \frac{\Phi_0}{2\pi I_c \cos \delta} \frac{dI_J}{dt}. \quad (1.11)$$

The Josephson inductance can be defined as

$$L_{JJ} \equiv \frac{V}{dI_J/dt} = \frac{\Phi_0}{2\pi I_c \cos \delta} \quad (1.12)$$

This approximation is only useful if δ is well-defined and the time-varying part of δ is small. It is not a useful quantity if the rf current is large and δ has a large

amplitude of oscillation; or if the dc current is above the critical current ($I_{dc} > I_c$) and δ increases with time.

An ideal Josephson junction can be treated as an inductor with a variable inductance given by Eq. 1.12. A more realistic model shunts the junction with a sub-gap resistance R due to loss, for example from the tunneling of normal state electrons across the junction. In addition real junctions are shunted by capacitance C (the capacitance of two overlapping conductors separated by an insulator) [1]. This defines the resistively and capacitively shunted junction (RCSJ) model with a circuit diagram as shown in Fig. 1.1 (b).

This model works reasonably well as long as the temperature is not too low, the critical current is not too small, and the voltage across the junction is less than the gap voltage $V < V_g$. The model can be extended to higher voltages by using a voltage-dependent resistance.

$$R = \begin{cases} R_{SG} & : V < V_g \\ R_N & : V > V_g \end{cases} \quad (1.13)$$

The normal tunneling resistance R_N is typically much less than the sub-gap resistance R_{SG} to represent loss due to quasiparticle generation, *i.e.* $R_N \ll R_{SG}$ [2]. For the junctions considered in this thesis $R_{SG}/R_N \cong 10$.

1.1.3 rf SQUIDS

An rf SQUID (radio frequency superconducting quantum interference device) is a superconducting loop interrupted by a single Josephson junction. The rf SQUID can be modeled as an RCSJ in parallel with an inductor representing the inductance

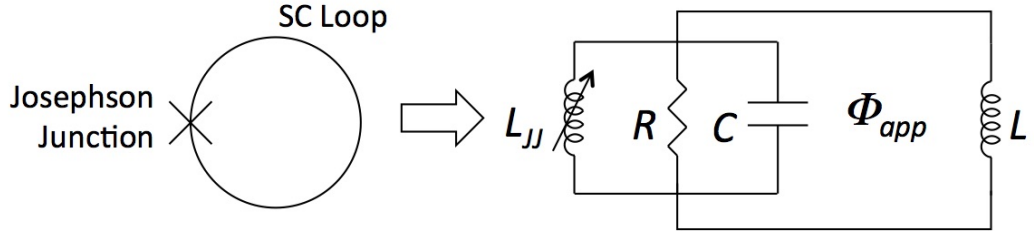


Figure 1.2: Circuit diagram of rf SQUID using the RCSJ model

L of the superconducting loop. The resulting RLC circuit, depicted in Fig. 1.2, has a resonant frequency given by

$$f_0 = \frac{1}{2\pi \sqrt{\left(\frac{1}{L} + \frac{1}{L_{JJ}}\right)^{-1} C}}, \quad (1.14)$$

The flux through an rf SQUID loop must be an integer number of flux quanta. Taking into account the additional phase from the junction, Eq. 1.5 can be written as

$$\Phi = n\Phi_0 + \frac{\Phi_0\delta}{2\pi} = \frac{\Phi_0\delta}{2\pi} \quad (1.15)$$

Setting $n = 0$ amounts to choosing the origin for the phase δ .

1.2 Metamaterials

Metamaterials are artificially structured media with electromagnetic properties arising from both the structure of individual meta-atoms and the interactions between them. Metamaterials can have interesting emergent properties that are not

seen in natural materials *e.g.* a negative index of refraction [5–7], cloaking [8, 9], super-resolution imaging [10, 11], and perfect absorption [12].

Superconducting metamaterials have several potential advantages over those made of normal metals, including low loss, small meta-atom size, and tunability [13, 14]. Low ohmic loss is important because many of the exciting features of metamaterials such as evanescent wave amplification [15] and negative refraction are strongly suppressed by even small amounts of loss [15–20]. Nonsuperconducting metamaterials in both the visible and microwave regimes, often have meta-atoms that approach the scale of the wavelength to minimize losses [21, 22]. Because of the way losses scale with size, superconducting meta-atoms can be made much smaller than the wavelength allowing them to operate well within the metamaterial limit, as opposed to the photonic crystal limit. In particular, I take advantage of the tunability and nonlinearity that superconductors afford to create metamaterials with tunable effective permeability and permittivity.

Superconducting metamaterials also have some limitations; they are confined to low temperatures and frequencies, and the extreme sensitivity to magnetic flux that makes them attractive for tuning applications also means that they require magnetic shielding to protect them from stray fields. Superconducting metamaterials are limited to low frequencies because superconductivity is destroyed above the gap frequency $f_{gap} = 2\Delta/h$, where Δ is the superconducting gap energy; $f_{gap} \approx 1.5$ THz for Nb, the superconductor used in this work. Superconducting metamaterials also require a cryogenic environment; the critical temperature of Nb is 9.2 K and the current record for high temperature superconductors (HTS) is $T_c = 133$ K [23].

(Recent progress has been made in producing high quality Josephson junctions with consistent critical currents in HTS [24].) This limitation is mitigated by progress made in closed-cycle cryocooler systems which have become small, efficient, and inexpensive. Such systems can operate for 5 years unattended, and can accommodate the heat load associated with microwave input and output transmission lines to room temperature [25].

1.2.1 Tunable Negative Effective Permeability

A metamaterial with a negative index of refraction

$$n = \sqrt{\epsilon\mu} \tag{1.16}$$

requires a negative effective permeability. $\mu = \mu_0(1 + \chi_m)$, where χ_m is the magnetic susceptibility. A conducting loop is diamagnetic by Lenz's law so the magnetic susceptibility is negative $\chi_m < 0$ but $|\chi_m| \ll 1$ so the effective permeability remains positive. The magnitude of the magnetic susceptibility can be enhanced by adding a resonance.

The SRR (split ring resonator), a well-studied resonant structure, is composed of a metallic ring with a gap on one side, Fig. 1.3 (a) [26]. The SRR is an LC resonator with the inductance coming from the loop and the capacitance from the gap. Similar resonant structures with inductive and capacitive elements have been used as meta-atoms, as shown in Fig. 1.3 (b). The properties of these meta-atoms are dependent on their geometry and fixed after fabrication

This limitation can be overcome by embedding the resonator in a nonlinear

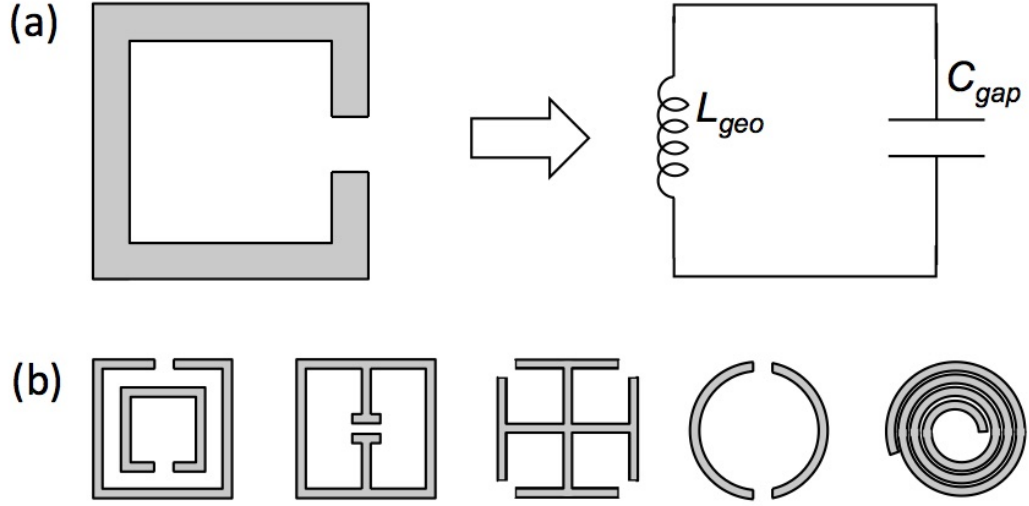


Figure 1.3: (a) Schematic and circuit diagram of basic SRR. (b) Schematics of similar resonant structures that have been used as meta-atoms.

medium [27] or by using a nonlinear inclusion instead of a gap in the ring *e.g.* a varactor diode which has a capacitance and conductivity that depend on the voltage across it [28, 29]. These techniques allow the properties of the metamaterial to be tuned after fabrication. However, tuning the nonlinear element increases losses which can be mitigated by using superconductors.

Superconducting metamaterials can be tuned via the kinetic inductance, the component of the inductance that comes from the kinetic energy stored in the supercurrent. The kinetic inductance can be increased by disrupting superconductivity which can be achieved by increasing temperature or by introducing currents or magnetic fields. However, these tuning techniques are slow and increase the dissipation.

Temperature tuning by exploiting the change in the kinetic inductance has

been demonstrated in SRRs [30, 31] and other superconducting metamaterials with meta-atoms shown in Fig. 1.3 [32–40]. However, temperature tuning is slow since the thermal inertia of the meta-atoms can be large, even at low temperatures. Typical estimates for temperature tuning response times are on the order of $10 \mu\text{s}$ [35].

Applied currents can tune superconducting metamaterials, by causing superfluid depairing which increases the kinetic inductance [41]. For example, applied currents can tune sub-THz transmission of a metamaterial composed of a network of resonators connected by a superconducting wire loop [35]. rf current can be induced in resonators designed to couple to electric field, suppressing superconductivity [40, 42, 43]. However, current often induces magnetic vortices in the superconductor before the depairing critical current is reached [35, 44]. These vortices move under the influence of the high-frequency current, enhancing dissipation.

Both dc and rf magnetic fields can tune superconducting metamaterials; an rf magnetic field creates enhanced rf screening currents at discrete locations in the SRR, enhancing inductance and dissipation as magnetic flux moves into and out of the superconducting film at high frequency [38, 45–49]. However, the insertion of magnetic flux into superconducting materials is often too slow and too dissipative for tuning applications.

The rf SQUID, which has a Josephson junction instead of the gap in the SRR, is a significant improvement over the meta-atoms described above; the resonance can be tuned quickly over a wide range without a substantial increase in losses. Using an rf SQUID as a meta-atom was first proposed theoretically [50–52]. In addition to the dc flux tuning of an individual SQUID meta-atom first experimentally demonstrated

by Jung *et al.* [53], we have shown tuning with rf flux and temperature [54]. We have also demonstrated a novel transparency behavior for intermediate values of rf flux.

Previous experimental work on rf SQUID metamaterials has been limited to 1D arrays and theoretical work has only considered nearest neighbor coupling between the SQUIDs. dc flux tuning has been experimentally demonstrated in 1D rf SQUID metamaterials [55, 56]. Multistability in the intermediate rf flux regime has been demonstrated experimentally in 1D arrays [57] and explored in 2D arrays theoretically [58]. Magneto-inductive modes have been theoretically predicted assuming nearest neighbor coupling in 1D [59] and 2D arrays of rf SQUIDs [60, 61]. Chimera states have also been theoretically predicted [62]. In this thesis, I consider fully coupled 2D arrays and the behavior resulting from the complex interactions between the SQUIDs, not seen in 1D.

1.2.2 Tunable Negative Effective Permittivity

To have a negative refractive index (Eq. 1.16), a material must have a negative effective permittivity at the same frequency it has negative effective permeability. The effective permittivity as a function of frequency in a loss-less plasmonic medium is given by,

$$\epsilon = 1 - \left(\frac{\omega_p}{\omega}\right)^2 \quad (1.17)$$

Negative effective permittivity in a metal can be achieved by stimulating it with an electromagnetic wave that has a frequency below the plasma frequency,

$\omega < \omega_p$. However, the plasma frequency is typically in the UV or optical range and I wish to make metamaterials in the GHz range.

Similar behavior has been observed in the GHz range by using an array of thin wires [63]. The permittivity obeys Eq. 1.17 but with the plasma frequency ω_p replaced with a cutoff frequency ω_c representing the LC resonance of the wire array [64]. Tuning of the permittivity in the GHz range has been demonstrated in superconducting wire arrays in an X-band waveguide [65]. The properties of these wire array metamaterials are determined by the size and spacing of the wires. I add Josephson junctions to the wires to allow tunability after fabrication with current and temperature.

Josephson junctions arrays have been extensively studied in 1D and 2D (Fig. 1.4) to make the junctions coherently emit microwaves in response to a dc voltage bias [66,67]. The Kuramoto model (which I use to quantify coherence in rf SQUID arrays in Sec. 2.6) has been applied to this system [68,69]. Experimental measurements have focused on IV dependence and microwave emission in the absence of a uniform drive [70–72].

When a uniform drive is applied to an array of Josephson junctions there are giant Shapiro steps, *i.e.* regular voltage steps as a function of dc current at $V = nN\Phi_0\omega/2\pi$ where N is the number of junctions. These steps are used as a voltage standard because they are easier to measure than those of a single junction and they are regular even when there is a spread in critical currents [4]. 2D Josephson junction arrays can also exhibit fractional giant Shapiro steps [73].

I am interested in how Josephson junction arrays behave as a metamaterial

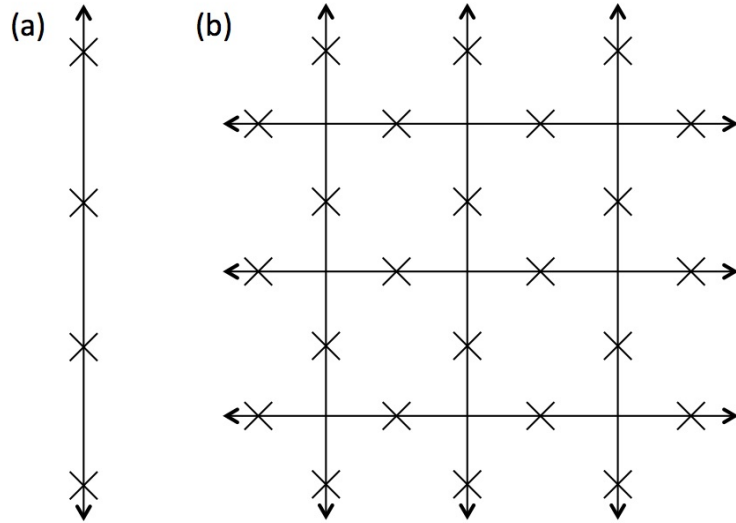


Figure 1.4: (a) 1D Josephson junction array. (b) 2D Josephson junction array.

and so primarily measure transmission of microwaves through the effective medium. The metamaterial considered in this thesis is an array of wires containing 100 junctions in the classical limit and has not previously been experimentally measured or considered in detail theoretically.

1.2.3 Tunable Negative Index Metamaterials

SRR arrays and arrays of thin wires have been successfully combined to produce a negative index material [6, 7]. Superconducting SRRs and wires have also been combined and show some tuning in response to temperature and magnetic field [65]. My goal was to build on this work by combining rf SQUIDS arrays and arrays of Josephson junction-loaded wires into a single metamaterial as illustrated

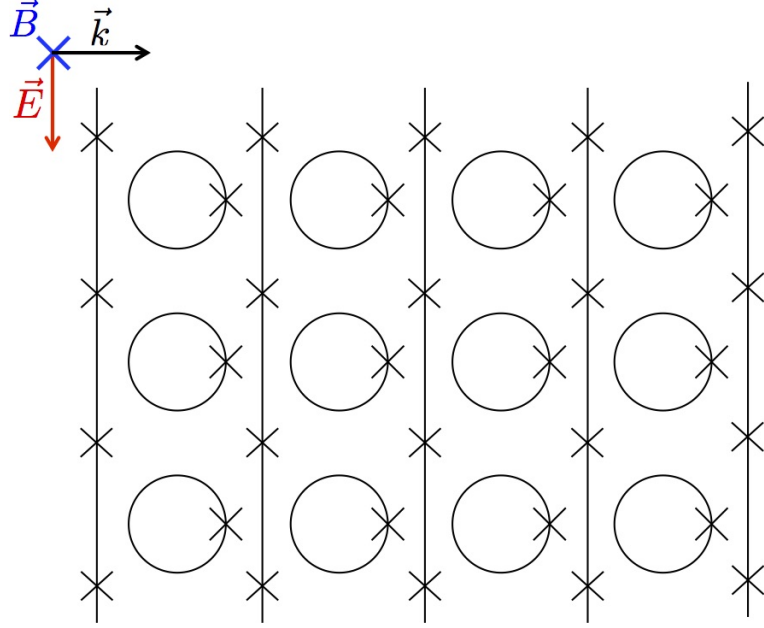


Figure 1.5: The rf SQUID and JJ-loaded wire arrays combined into a single metamaterial with a tunable refractive index. The full 3D structure would have layers stacking out of the page. The incident waves are oriented so the electric field interacts with the wires and the magnetic field with the SQUIDS

in Fig. 1.5. This metamaterial would have an index of refraction (Eq. 1.16) which could be tuned over a larger range and faster than previous implementations without increasing losses.

1.3 What Follows

The remainder of the thesis is organized as follows. Chapter 2 explains how to calculate quantities of interest *i.e.* transmission S_{21} and coherence r_A . Chapter 3 provides details of the samples (both their design and preparation) and the experimental setup. Chapter 4 shows how the resonant frequency and the permeability of a single rf SQUID tune with dc flux, temperature, and rf flux and provides estimates of the tuning speed. Chapter 5 shows how the tuning properties of a 2D array are similar to the single SQUID and how the arrays differ *i.e.* coupling between the SQUIDs, magneto-inductive modes, and disorder. Chapter 6 shows how the JJ-loaded wire array tunes as designed in the low rf and dc current limits and briefly explores the complicated hysteretic and nonlinear behavior beyond these limits. Chapter 7 summarizes what I've done, discusses possible applications, and suggests directions for future work.

Chapter 2: Model and Simulations

The key to understanding the dynamics of Josephson metamaterials is the gauge-invariant phase difference across a junction $\delta(t)$. In this chapter, I describe how to calculate $\delta(t)$ for single junctions, individual SQUIDs, two coupled SQUIDs, and coupled 2D SQUID arrays. From $\delta(t)$ any quantity of interest can be calculated, *e.g.* transmission S_{21} which can be compared to measurements. For details on how the parameters were chosen for these simulations see Sec. C and for details on the Python scripts I used to perform these calculations see Sec. D.

2.1 Single Josephson Junction

A model for the JJ-loaded wire arrays begins with the gauge-invariant phase difference across a single junction $\delta(t)$. The applied current (both dc and rf parts) must be equal to the sum of the currents through the junction, the resistor, and the capacitor (using the RCSJ model, Fig. 1.1 (b)), which written in terms of δ has the following form

$$I_{dc} + I_{rf} \sin \omega t = I_c \sin \delta + \frac{1}{R} \frac{\Phi_0}{2\pi} \frac{d\delta}{dt} + C \frac{\Phi_0}{2\pi} \frac{d^2\delta}{dt^2} \quad (2.1)$$

where I_{dc} is the applied dc current and I_{rf} and ω are the amplitude and angular frequency of the applied rf current. This equation can be recast in dimensionless

form as

$$\frac{I_{dc}}{I_c} + \frac{I_{rf}}{I_c} \sin \Omega \tau = \sin \delta + \gamma \frac{d\delta}{d\tau} + \frac{d^2\delta}{d\tau^2} \quad (2.2)$$

where

$$\begin{aligned} \tau &= \omega_{jp} t & \Omega &= \omega / \omega_{jp} \\ \omega_{jp} &= \sqrt{\frac{1}{L_{JJ}(\delta=0)C}} & \gamma &= \frac{1}{R} \sqrt{\frac{L_{JJ}(\delta=0)}{C}} \end{aligned}$$

ω_{jp} is the plasma frequency of the junction. $\delta(t)$ can be used to calculate values of interest such as the cutoff frequency of the metamaterial ω_c and the effective permittivity as shown in Sec. 2.5.2.

Equation 2.2 can have chaotic solutions if any of the following conditions are not met [74]:

$$\beta_c = \frac{2\pi I_c R^2 C}{\Phi_0} \ll 1 \quad (2.3)$$

$$\omega \gg \omega_{jp} \quad (2.4)$$

$$I_{rf}/I_c \ll 1 \quad (2.5)$$

For the junctions I designed $\beta_c = 70$ and $\omega_{jp}/2\pi = 9$ GHz (slightly lower than the measurement range), so chaotic behavior is possible for sufficiently high values of rf current, but the JJ-loaded wire arrays are designed to operate in the low rf current limit, $I_{rf}/I_c \ll 1$. A well-studied mechanical analogue of the Josephson junction is the driven and damped pendulum [75].

2.2 Single rf SQUID

A similar equation for the gauge-invariant phase difference $\delta(t)$ can be derived for the rf SQUID. The total flux Φ is the sum of the applied flux Φ_{app} and the current-induced flux

$$\Phi = \Phi_{app} - LI \quad (2.6)$$

where L is the geometric inductance of the superconducting loop and I is the current through the loop, which (using the RCSJ model) is the sum of the currents through the junction, the resistor, and the capacitor. Equation 2.6 can be rewritten in the terms of δ (using flux quantization to substitute for Φ using Eq. 1.15)

$$\Phi_{dc} + \Phi_{rf} \sin \omega t = \frac{\Phi_0 \delta}{2\pi} + L \left(I_c \sin \delta + \frac{1}{R} \frac{\Phi_0}{2\pi} \frac{d\delta}{dt} + C \frac{\Phi_0}{2\pi} \frac{d^2 \delta}{dt^2} \right) \quad (2.7)$$

where Φ_{dc} is the applied dc magnetic field and Φ_{rf} and ω are the amplitude and angular frequency of the applied rf flux. This equation can be recast in dimensionless form as

$$\frac{2\pi}{\Phi_0} (\Phi_{dc} + \Phi_{rf} \sin \Omega \tau) = \delta + \beta_{rf} \sin \delta + \gamma \frac{d\delta}{d\tau} + \frac{d^2 \delta}{d\tau^2} \quad (2.8)$$

where

$$\begin{aligned} \tau &= \omega_{geo} t & \Omega &= \omega / \omega_{geo} & \omega_{geo} &= \sqrt{1/LC} \\ \beta_{rf} &= \frac{2\pi L I_c}{\Phi_0} & \gamma &= \frac{1}{R} \sqrt{\frac{L}{C}} \end{aligned}$$

This equation is very similar to Eq. 2.2 for a single Josephson junction; however, incorporating the junction into a superconducting loop subject to flux quantization introduces an additional term linear in δ on the right-hand side of Eq.

2.8. Unlike the single Josephson junction and its mechanical analogue, the driven damped pendulum, this equation is linear in the high rf flux limit in addition to the low rf flux limit, assuming $\beta_{rf} < 1$ (all of the SQUIDs discussed here fulfill that condition). The solutions for $\delta(t)$ are sinusoidal with the same frequency as the rf driving flux; there are no chaotic solutions for $\beta_{rf} < 1$ [76].

2.2.1 Low rf Flux Limit

Equation 2.8 can be linearized in the limit $\Phi_{rf} \ll \Phi_0$ by separating the phase difference into dc and rf components $\delta(\tau) = \delta_{dc} + \delta_{rf}(\tau)$ where it is assumed that the time-varying component of the phase difference is very small *i.e.* $\delta_{rf}(\tau) \ll 1$.

$$\sin \delta = \sin(\delta_{dc} + \delta_{rf}) = \sin \delta_{dc} \cos \delta_{rf} + \cos \delta_{dc} \sin \delta_{rf} \approx \sin \delta_{dc} + \delta_{rf} \cos \delta_{dc} \quad (2.9)$$

By substituting Eq. 2.9 for the sine term in 2.8, the equation can be linearized and separated into the following time-independent and time-dependent equations:

$$2\pi \frac{\Phi_{dc}}{\Phi_0} = \delta_{dc} + \beta_{rf} \sin \delta_{dc} \quad (2.10)$$

$$2\pi \frac{\Phi_{rf}}{\Phi_0} \sin \Omega\tau = \eta \delta_{rf} + \gamma \frac{d\delta_{rf}}{d\tau} + \frac{d^2\delta_{rf}}{d\tau^2} \quad (2.11)$$

where $\eta = 1 + \beta_{rf} \cos \delta_{dc}$. Equation 2.11 has an analytic solution for δ_{rf} given by

$$\delta_{rf} = 2\pi \frac{\Phi_{rf}}{\Phi_0} \frac{(\eta - \Omega^2) \sin \Omega\tau - (\Omega\gamma) \cos \Omega\tau}{(\eta - \Omega^2)^2 + (\Omega\gamma)^2}. \quad (2.12)$$

The resonant frequency can be calculated by using the solution for δ_{dc} (Eq. 2.10) to calculate the Josephson inductance L_{JJ} (Eq. 1.12), and then f_0 (Eq. 1.14). The resonant frequency is periodic in dc flux with a range of the dc flux tunability

given by

$$f_0 \left(\frac{\Phi_{dc}}{\Phi_0} = 0 \right) = f_{geo} \sqrt{1 + \beta_{rf}} \quad (2.13)$$

$$f_0 \left(\frac{\Phi_{dc}}{\Phi_0} = \frac{1}{2} \right) = f_{geo} \sqrt{1 - \beta_{rf}} \quad (2.14)$$

where $f_{geo} = \omega_{geo}/2\pi$.

The resonant frequency is temperature dependent because the critical current is temperature dependent and goes to zero at T_c . In the high temperature limit $\beta_{rf} = 0$, the resonance cannot be tuned by dc flux, and $f_0 = f_{geo}$.

2.2.2 High rf Flux Limit

Equation 2.8 is also linear in the high rf flux limit (where it is assumed $\delta_{rf} \gg 1$) because $\beta_{rf} \sin \delta + \delta \approx \delta$ for $\beta_{rf} < 1$. The equation can be separated into the following time dependent and time independent equations:

$$2\pi \frac{\Phi_{dc}}{\Phi_0} = \delta_{dc} \quad (2.15)$$

$$2\pi \frac{\Phi_{rf}}{\Phi_0} \sin(\Omega\tau) = \delta_{rf} + \gamma \frac{d\delta_{rf}}{d\tau} + \frac{d^2\delta_{rf}}{d\tau^2} \quad (2.16)$$

Equation 2.16 has the same analytic solution as Eq. 2.12 with η replaced by 1, so unlike Eq. 2.12 it has no dependence on temperature or dc flux. The resonant frequency is simply the geometric resonant frequency f_{geo} as it is in the high temperature limit.

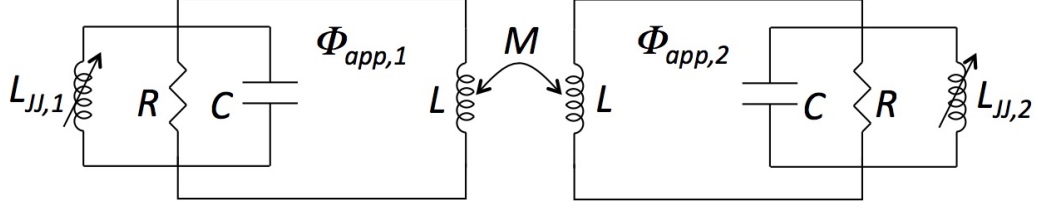


Figure 2.1: Circuit diagram of a pair of rf SQUIDs showing the mutual inductance between them.

2.3 Pair of rf SQUIDs

The difference in the behavior of one SQUID and two SQUIDs is caused by the coupling between them; there is an additional flux term that needs to be added to Eq. 2.6 due to the mutual inductance between the loops M , see Fig. 2.1. The flux in each SQUID is then

$$\Phi_1 = \Phi_{app,1} + MI_2 - LI_1 \quad (2.17)$$

$$\Phi_2 = \Phi_{app,2} + MI_1 - LI_2 \quad (2.18)$$

where I_1 and I_2 are the currents through each loop. $M < 0$ because the SQUID's magnetic field induces an opposing response in its neighbor for the coplanar geometry used here.

Following a procedure similar to the one used above, Eqs. 2.17 and 2.18 can be rewritten as a pair of dimensionless coupled differential equations in terms of the

gauge-invariant phase difference across each junction δ_1 and δ_2

$$\begin{aligned} \frac{2\pi}{\Phi_0} (\Phi_{dc,1} + \Phi_{rf} \sin \Omega\tau) &= \delta_1 + \beta_{rf} \sin \delta_1 + \gamma \frac{d\delta_1}{d\tau} \\ &+ \frac{d^2\delta_1}{d\tau^2} + \kappa \left(\beta_{rf} \sin \delta_2 + \gamma \frac{d\delta_2}{d\tau} + \frac{d^2\delta_2}{d\tau^2} \right) \end{aligned} \quad (2.19)$$

$$\begin{aligned} \frac{2\pi}{\Phi_0} (\Phi_{dc,2} + \Phi_{rf} \sin \Omega\tau) &= \delta_2 + \beta_{rf} \sin \delta_2 + \gamma \frac{d\delta_2}{d\tau} \\ &+ \frac{d^2\delta_2}{d\tau^2} + \kappa \left(\beta_{rf} \sin \delta_1 + \gamma \frac{d\delta_1}{d\tau} + \frac{d^2\delta_1}{d\tau^2} \right) \end{aligned} \quad (2.20)$$

where $\kappa = M/L$ is the ratio of the mutual inductance to the self-inductance. As before the equations can be linearized in the limit of low and high rf flux.

2.4 rf SQUID Arrays

For each additional SQUID there is an additional applied flux term

$$\Phi = \Phi_{app} + \sum_{j \neq i}^N (M_{ij} I_j) - L I_i \quad (2.21)$$

where N is the total number of SQUIDS and M_{ij} is the mutual inductance between SQUIDS i and j .

An array of N coupled rf SQUIDS can be described by the following set of coupled nonlinear differential equations:

$$\frac{2\pi}{\Phi_0} (\hat{\Phi}_{dc} + \hat{\Phi}_{rf} \sin \Omega\tau) = \hat{\delta} + \bar{\kappa} \left(\beta_{rf} \sin \hat{\delta} + \gamma \frac{d\hat{\delta}}{d\tau} + \frac{d^2\hat{\delta}}{d\tau^2} \right) \quad (2.22)$$

where $\hat{\delta}$ is a vector of length N representing the gauge-invariant phase difference across the junction for each of the N SQUIDS. $\hat{\Phi}_{dc}$ and $\hat{\Phi}_{rf}$ are vectors representing

the the dc and rf applied flux in each SQUID respectively. $\bar{\kappa}$ is $N \times N$ 2D matrix that describes the coupling between every pair of SQUIDs where

$$\kappa_{ij} = \begin{cases} 1 & : i = j \\ M_{ij}/L & : i \neq j \end{cases} \quad (2.23)$$

The following values are assumed to be identical for all SQUIDs: β_{rf} , γ , ω , and Φ_{rf} because the lithographic process to define the SQUIDs has little variation and the measurement conditions assure uniform rf flux and frequency [54]. However, the edge-effects present in the coupling matrix $\bar{\kappa}$ are preserved and non-uniform Φ_{dc} is considered.

Equation 2.22 can also be linearized in the limit $\Phi_{rf}/\Phi_0 \ll 1$ yielding the following system of equations

$$\hat{\delta}_{dc} + \beta_{rf} \bar{\kappa} \sin \hat{\delta}_{dc} = \frac{2\pi}{\Phi_0} \hat{\Phi}_{dc} \quad (2.24)$$

$$\begin{bmatrix} \bar{K} & -\gamma\Omega\bar{I} \\ \gamma\Omega\bar{I} & \bar{K} \end{bmatrix} \begin{bmatrix} \hat{a} \\ \hat{b} \end{bmatrix} = \begin{bmatrix} \hat{F} \\ \hat{0} \end{bmatrix} \quad (2.25)$$

where

$$\bar{K} = \bar{\kappa}^{-1} + \beta_{rf} \cos \bar{\delta}_{dc} - \Omega^2 \bar{I}$$

$$\hat{F} = 2\pi \bar{\kappa}^{-1} \frac{\hat{\Phi}_{rf}}{\Phi_0}$$

$$\hat{\delta}_{rf}(t) = \hat{a} \sin \Omega\tau + \hat{b} \cos \Omega\tau$$

From the solutions for the gauge-invariant phase difference any value of interest can be calculated, including transmission S_{21} and coherence r_A , discussed below.

2.5 Calculating Transmission

I used two methods for calculating transmission S_{21} from the solution for $\delta(t)$ ($\hat{\delta}(t)$ in SQUID arrays).

2.5.1 Dissipated Power

A simple method for estimating S_{21} focuses on the power dissipated in the resistor of the RCSJ model.

$$S_{21} = \sqrt{\frac{P_T}{P_0}} = \sqrt{1 - \frac{\sum_j^N V_j^2/R}{P_0}} \quad (2.26)$$

where P_T is the transmitted power, P_0 is the incident power, and V_j is the voltage across the j th junction. This equation assumes that the only power not transmitted through the waveguide is the power dissipated in the resistors; it does not account for reflection or other loss mechanisms.

2.5.2 Effective Medium

An alternate method for determining transmission considers the metamaterial an effective medium with an effective relative permeability μ_r (in the case of the rf SQUIDS) or an effective relative permittivity ϵ_r (in the case of the JJ-loaded wire arrays). This block of material is bordered on each side by a section of empty waveguide.

To calculate ϵ_r for JJ-loaded wire arrays, the Josephson inductance is found (Eq. 1.12) by using the time-averaged value of $\delta(t)$ (Eq. 2.2) and this is used to

find the cutoff frequency

$$\omega_c = \frac{1}{d} \sqrt{\frac{l}{(L_{geo} + NL_{JJ})\epsilon_0}} \quad (2.27)$$

where d is the spacing between the wires, l is the length of the wires, L_{geo} is the geometric inductance of the superconductor, and N is the number of junctions per wire [77]. This model is only valid when Eq. 1.12 is a good approximation *i.e.* low rf current I_{rf} and $I_{dc} < I_c$. This model also assumes that all the junctions are identical, and that they only interact through their shared current. The effective permittivity can be calculated from the cutoff frequency ω_c

$$\epsilon_r = 1 + F \left(\frac{\omega_c}{\omega} \right)^2 \quad (2.28)$$

where F is the filling fraction of the metamaterial in the waveguide.

The effective permeability of SQUIDs and SQUID arrays can be calculated directly from the solution for δ

$$\mu_r = 1 + F \left(\frac{\sum_j^N (a_j + ib_j)}{2\pi\Phi_{rf}/\Phi_0} - 1 \right), \quad (2.29)$$

where $\delta_j(t) = a_j \sin \Omega\tau + b_j \cos \Omega\tau$.

Once the properties of the effective medium have been determined, the transmission through a uniform block of this material embedded in a waveguide can be calculated. E and H fields must be continuous at the boundaries of the effective medium and the empty waveguide. Enforcing these boundary conditions yields the

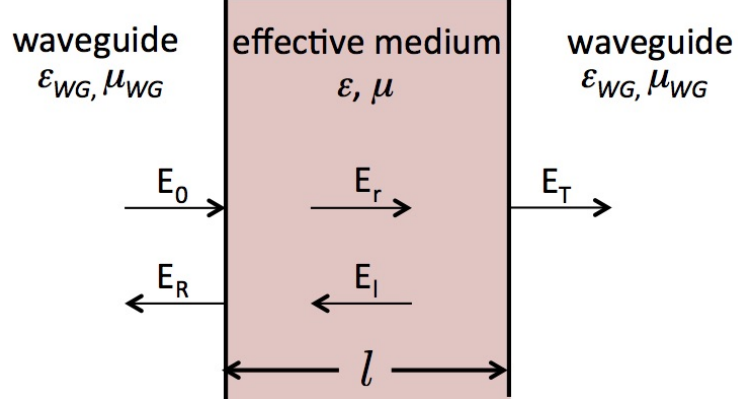


Figure 2.2: Reflected and transmitted waves in effective medium calculation.

following four equations.

$$E_0 + E_R = E_r + E_l \quad (2.30)$$

$$E_r e^{ikl} + E_l e^{-ikl} = E_T e^{ik_0 l} \quad (2.31)$$

$$\frac{1}{\mu_0 c} (E_0 - E_R) = \frac{1}{\mu v} (E_r - E_l) \quad (2.32)$$

$$\frac{1}{\mu v} (E_r e^{ikl} - E_l e^{-ikl}) = \frac{1}{\mu_0 c} E_T e^{ik_0 l} \quad (2.33)$$

The reflected and transmitted waves are illustrated in Fig. 2.2.

These equations can be solved for transmission S_{21} and reflection S_{11} through the waveguide

$$S_{21} = \frac{E_T}{E_0} = \frac{1}{\cos kl - \frac{i}{2} \left(\frac{1}{\beta} + \beta \right) \sin kl} \quad (2.34)$$

$$S_{11} = \frac{E_R}{E_0} = S_{21} \frac{i}{2} \left(-\frac{1}{\beta} + \beta \right) \sin kl \quad (2.35)$$

where

$$\beta = \frac{k}{\mu_r \epsilon_r k_0}$$

$$k = \sqrt{\mu_r \epsilon_r \left(\frac{\omega}{c}\right)^2 - \left(\frac{\pi}{a_{dim}}\right)^2}, \quad \text{wavenumber in the medium}$$

$$k_0 = k(\mu_r = \epsilon_r = 1), \quad \text{wavenumber in the empty waveguide}$$

l is the length of the medium, c is the speed of light, and a_{dim} is the longer of the two waveguide dimensions.

2.6 Quantifying Coherence in rf SQUID Arrays

The typical Kuramoto system is a collection of linear harmonic oscillators with a Gaussian distribution of self-resonant frequencies [78]. These oscillators interact through nonlinear uniform all-to-all coupling and their dynamics are described by the following system of equations:

$$\dot{\alpha}_i = \omega_i + \frac{K}{N} \sum_{j=1}^N \sin(\alpha_j - \alpha_i) \quad (2.36)$$

where α_j is the phase of the j th oscillator, ω_i is its self-resonant frequency, K is the strength of the coupling between the oscillators, and N is the number of oscillators.

The Kuramoto model quantifies coherence with an order parameter,

$$r = \left| \frac{1}{N} \sum_j e^{i\alpha_j} \right| \quad (2.37)$$

Perfect coherence ($r = 1$) is achieved when the SQUIDs are all oscillating in phase at the same frequency despite the differences in self-resonant frequencies. $r = 0$ represents complete incoherence. The Kuramoto model order parameter has been

used to quantify coherence in numerical studies of 1D rf SQUID metamaterials [58].

I have found that a modified order parameter is more useful.

There are several differences between the basic Kuramoto system and the 2D array of rf SQUIDs. The Kuramoto model considers linear oscillators that are nonlinearly coupled where rf SQUIDs are nonlinear oscillators that are linearly coupled. The basic Kuramoto model only considers uniform coupling, although it has been extended to consider coupling that has a power law dependence on the separation between the oscillators which is more like the coupling between the SQUIDs [79]. The basic Kuramoto model also doesn't include an rf drive or second order dynamics, but these extensions to the original model have been considered [80, 81].

The most important difference (*i.e.* the one that motivates the modification to the order parameter) is that the Kuramoto model only considers phase information and assumes that the amplitudes of all the oscillators are the same. Simulations of rf SQUID arrays show that the amplitudes of oscillation can have a wide distribution. Consequently, I use a modified coherence order parameter that gives greater weight to the phase of oscillators with greater amplitude

$$r_A = \left| \frac{\sum_j^N A_j e^{i\alpha_j}}{\sum_j^N A_j} \right| \quad (2.38)$$

where A_j is the amplitude of oscillation of $\delta_j(t)$ for the j th rf SQUID and the phase is measured relative to the phase of the drive. This modified parameter still falls between 0 and 1 with $r_A = 1$ representing perfect coherence.

Chapter 3: Experimental Details

In this chapter, I describe how the Josephson metamaterials were designed, prepared, and measured. Details of samples which were prepared but do not have results appearing in the main body of this thesis can be found in Sec. B.

3.1 Sample Design

3.1.1 rf SQUIDS

The superconducting loop of each rf SQUID is composed of two Nb films that are connected by a via and a Nb/AlO_x/Nb Josephson junction. There is additional capacitance where these layers overlap (with SiO₂ dielectric) which is necessary to bring the resonant frequency within the measurable range. When designing the SQUIDS, I control the loop inductance L (by controlling inner and outer radii of the loop), the critical current of the junction I_c , and the overlap capacitance C . Values for L , I_c , and C were chosen to maximize tunability within the measurable frequency range 6.5 – 26.5 GHz while keeping the SQUIDS non-hysteretic $\beta_{rf} < 1$, and low noise [82]:

$$\Gamma = \frac{2\pi k_B T}{\Phi_0 I_c} < 1 \qquad L_F = \frac{1}{k_B T} \left(\frac{\Phi_0}{2\pi} \right)^2 \gg L$$

The individual meta-atom presented in this thesis has parameter values listed first in Tab. 3.1. (See Sec. C for details on how each parameter is fit to data.) This rf SQUID has 3 μm diameter holes in the Nb film every 10 μm to pin vortices [83]. The holes do not affect the inductance of the SQUID because the current is concentrated on the inner edge of the loop. HFSS simulations confirmed this, showing no change in the resonant response or current distribution in the rf SQUID when the holes were present. HFSS could not provide insight into how these holes interact with vortices because HFSS is not equipped to handle superconductivity in detail. Later generations of samples lack these holes because it is more important that there are no vortices coupling flux into the SQUID loop than that they are pinned.

Table 3.1: Parameters of measured SQUID and SQUID arrays.

	made by	Λ	$ \kappa_0 $	L (nH)	C (pF)	I_c (μA)	R ($k\Omega$)	β_{rf}	Fig.
single	Hypres	—	—	0.33	0.42	0.75	0.25	0.55	3.1
11x11	Hypres	180	0.003	0.056	2.1	5.4	0.5	0.86	3.2 (a)
21x21	IREE	270	0.006	0.13	2.1	2.0	1.0	0.77	3.3 (a)
21x21	IREE	380	0.02	0.13	2.1	2.0	1.0	0.77	3.3 (b)
27x27	Hypres	350	0.03	0.12	0.93	2.2	1.5	0.80	3.2 (b)

In addition to the individual rf SQUID, several 2D arrays of nominally identical rf SQUIDs were measured; in the body of this thesis I present results from an 11x11, 27x27, and two 21x21 arrays. The parameters of these arrays are listed in Tab. 3.1. The large ratio of the wavelength to the lattice parameter shows that these arrays are well-within the metamaterial limit, $\Lambda \gg 1$.

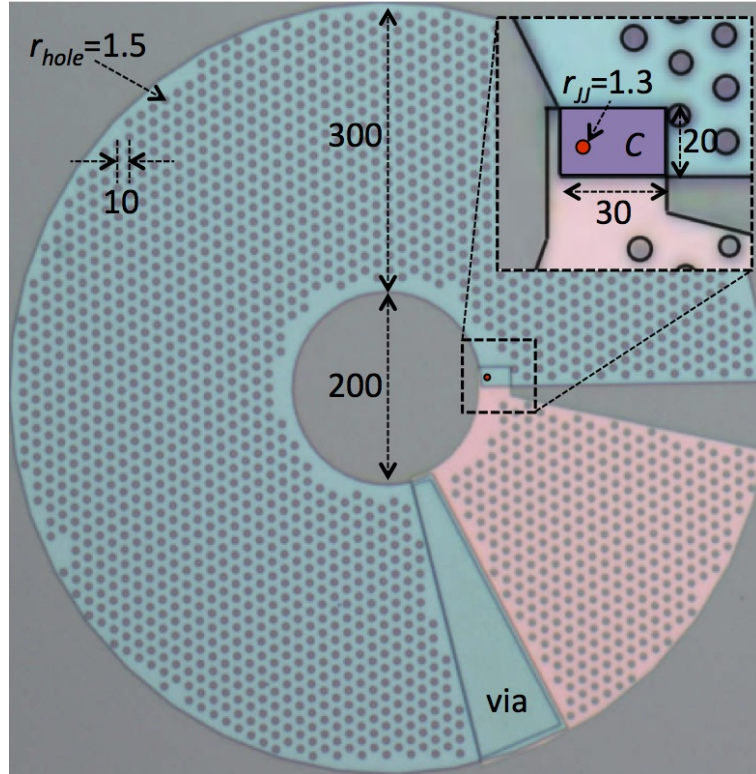


Figure 3.1: Individual rf SQUID meta-atom. Inset: An enlargement showing the junction (red) and overlap capacitance (purple). All dimensions in μm .

The two 21×21 arrays were designed by Philipp Jung¹ and are identical except for the spacing (and therefore the coupling) between the SQUIDs. The maximum coupling of these SQUIDs, determined by FastHenry calculations [84], is $\kappa_0 = -0.06$ (when the SQUIDs are as close together as possible).

¹Physikalisches Institut, Karlsruhe Institute of Technology, Germany

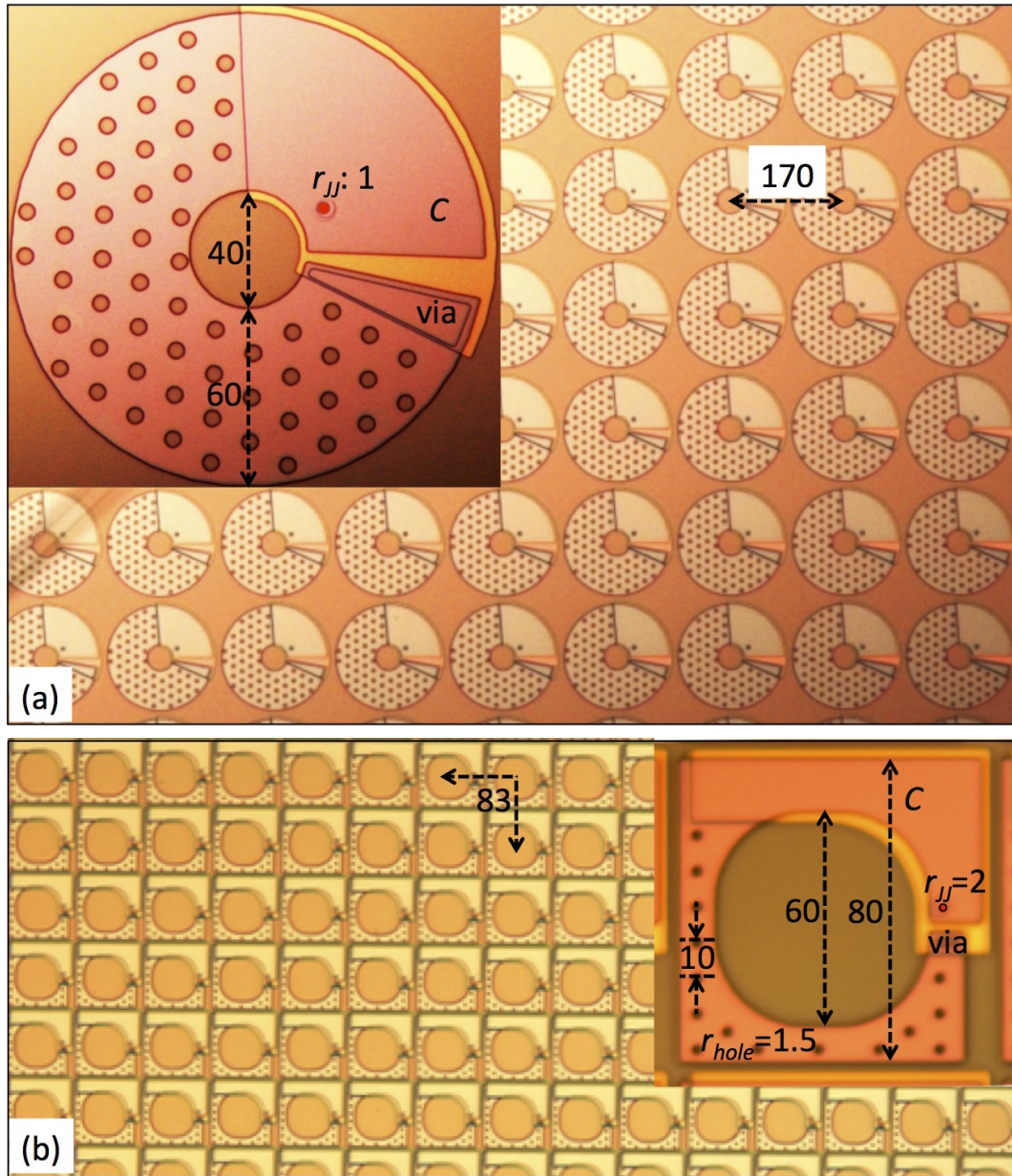


Figure 3.2: (a) 11x11 rf SQUID array. (b) 27x27 rf SQUID array. Inset: Enlargement of SQUID. All dimensions in μm .

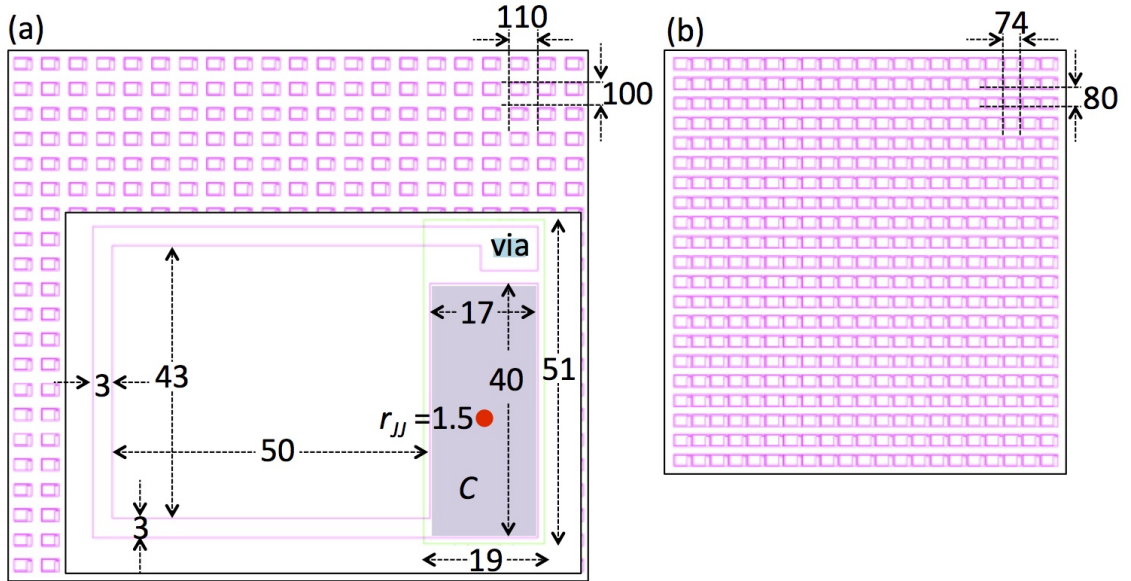


Figure 3.3: 21x21 rf SQUID arrays. (a) Loosely coupled sample $|\kappa_0| = 0.006$. (b) Tightly coupled sample $|\kappa_0| = 0.02$. Inset: SQUID for both the loosely and tightly coupled arrays, including the junction (red) and the overlap capacitance (purple). All dimensions in μm .

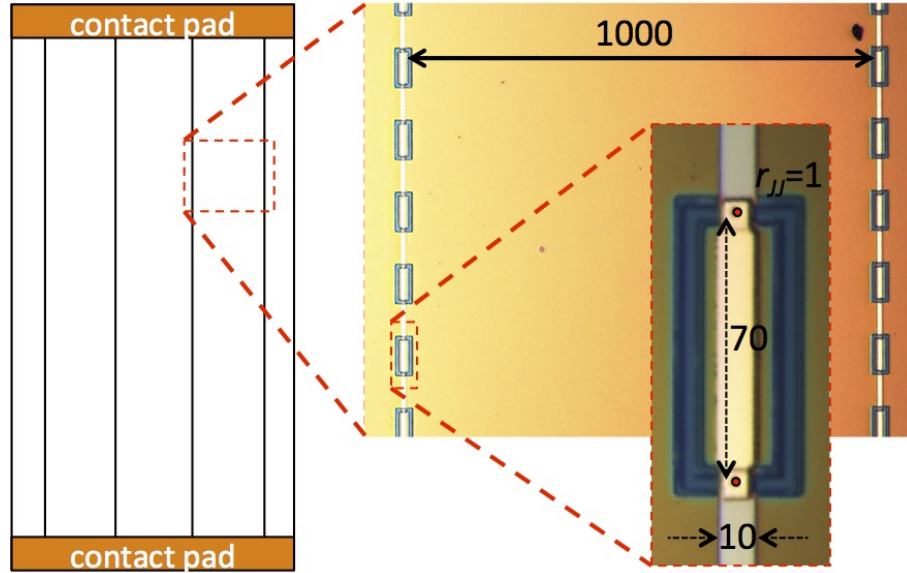


Figure 3.4: Josephson junction-loaded wire arrays. All dimensions in μm .

3.1.2 JJ-loaded wire arrays

The electric metamaterials prepared by IREE (Fig. 3.4) are designed to have a cutoff frequency that tunes through the measurable frequency range, 6.5 – 26.5 GHz. There are four equally spaced wires of 100 junctions each on a 4x8 mm² silicon chip. The junctions are nominally identical with critical currents of $I_c(T = 4.5 \text{ K}) = 0.25 \mu\text{A}$ and the minimum amount of overlap capacitance. There are gold contact pads at each end to apply dc current bias; the contacts are normal metal so the wires are not part of superconducting loops. The blue features in Fig. 3.4 are the “ghost contacts” from the anodization step and not structures that affect operation.

3.2 Sample Fabrication

Samples were fabricated using two slightly different processes: one by Hypres² and the other by IREE³.

3.2.1 Hypres Process

The individual rf SQUID sample, 11x11 array, and 27x27 SQUID array described above were prepared using the Hypres 0.3 $\mu\text{A}/\mu\text{m}^2$ Nb/ AlO_x /Nb junction process on silicon substrates [85–87]. (Measurements of other junctions from this run suggest the critical current density is closer to 0.2 $\mu\text{A}/\mu\text{m}^2$ at 4.2 K.) The penetration depth of the Nb is 90 nm. The layers of the process are listed in Tab.

3.2.

3.2.2 IREE Process

The 21x21 rf SQUID arrays and Josephson junction-loaded wire arrays were prepared by IREE using a similar process with a higher critical current density, 1 $\mu\text{A}/\mu\text{m}^2$ [88–92]. There are some minor differences in the thicknesses of various layers and the penetration depth of the Nb at 85 nm. The layers are listed in Tab.

3.3.

The largest difference between the two processes is that in the IREE process the anodization of the Nb_2O_5 that protects the junction occurs after the junction is

²175 Clearbrook Road, Elmsford, NY 10523, USA

³Institute of Radio Engineering and Electronics, Moscow, Russia

Table 3.2: Layers in Hypres process.

Layer Name	Material	Thickness (nm)	Layer Description
M0	Nb	100	Ground plane
I0	SiO ₂	150	Insulator, capacitance: 0.28 fF/ μm^2
M1	Nb	135	Trilayer base electrode
I1A	AlO _x /Nb	50	Trilayer counter electrode and tunnel barrier
A1	Nb ₂ O ₅	40	Insulation around the junction
	SiO ₂	100	Insulator, capacitance: 0.42 fF/ μm^2
R2	Ti/AuPd/Ti	100	resistance: 2 $\Omega/\mu\text{m}^2$
	SiO ₂	100	Insulator, capacitance: 0.42 fF/ μm^2
I1B			Contact hole through SiO ₂ layers
M2	Nb	300	
	SiO ₂	500	Insulator, capacitance: 0.08 fF/ μm^2
I2			Contact hole through SiO ₂ layer
M3	Nb	600	
R3	Ti/Pd/Au	350	Contact pads

defined instead of before. This necessitates additional metal structures that connect areas that require anodization to leads on the edge of the wafer. These structures are removed later in the process but residual “ghost contacts” are still visible.

3.3 Measurement Setup

The experiment was conducted in a two-stage (40 K and 4 K) pulsed-tube cryostat with a base temperature of 4.5 K.

Table 3.3: Layers in IREE process.

Layer Name	Material	Thickness (nm)	Layer Description
M0	Nb	150	Ground plane
I0	SiO ₂	170	Insulator, capacitance: 0.25 fF/ μm^2
M1	Nb	200	Trilayer base electrode
I1	AlO _x /Nb	80	Trilayer counter electrode and tunnel barrier
	Nb ₂ O ₅	40	Insulation around the junction
	SiO ₂	250	Insulator, capacitance: 0.17 fF/ μm^2
ETCH			
RES	Mo	variable	
	SiO ₂	100	Insulator, capacitance: 0.42 fF/ μm^2
M2	Nb	350	
I2	SiO ₂	400	Insulator, capacitance: 0.11 fF/ μm^2
M3	Nb	450	
Cont	Al/Au	200	Contact pads

3.3.1 Microwave Path

Figure 3.5 shows the microwave setup. A microwave signal is first generated by an Agilent N5242A (E8364C for single SQUID measurements) network analyzer. The microwaves pass through a 20 dB attenuator before entering the cryogenic environment. The signal travels semi-rigid non-magnetic coax cables (made by Coax [93]) to a 6-way switch (Radiall R591722605) on the 4 K stage that sends the signal to one of two waveguides. The signal is coupled to the waveguide, exciting a TE₁₀ mode in the 76 mm copper rectangular waveguide, operating between cutoff and the frequency of the next highest mode (see Tab. 3.4 and Fig. 3.6 for details of

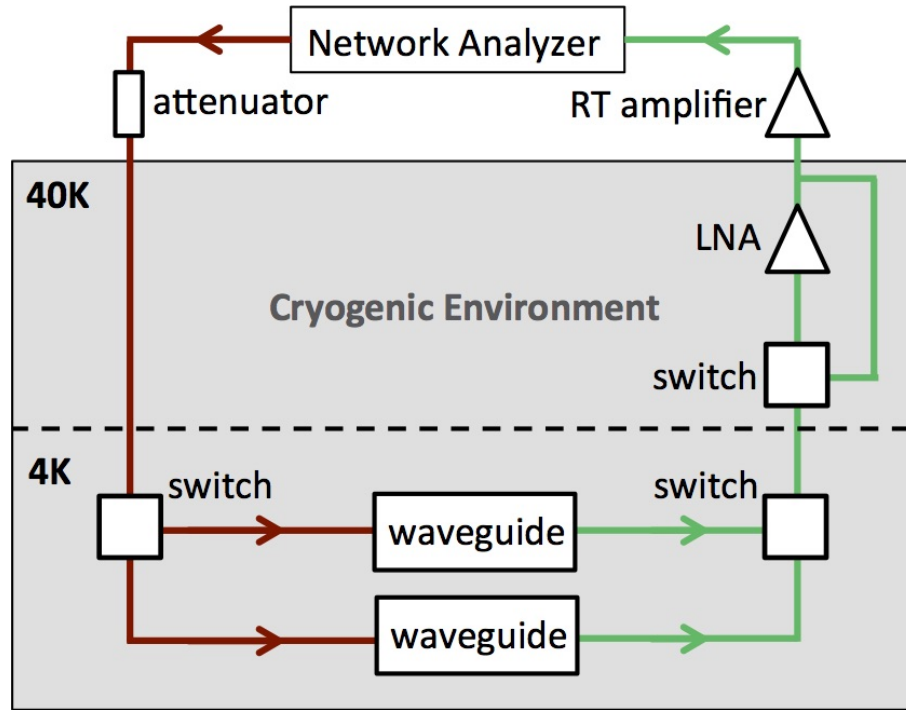


Figure 3.5: Microwave setup.

the X, Ku, and K waveguides). The microwaves interact with the sample mounted in the center of the waveguide before being coupled back to the output coax line and passing through another 6-way switch. On the way out there is cryogenic low noise amplifier (Low Noise Factory LNF-LNC6.20A) on the 40 K stage which provides 32 dB of gain. There is also a single-pole double-throw switch on this stage (Radiall R595F33115) which allows the amplifier to be bypassed, see Fig. 3.7 (a). Once outside the cryogenic environment, the microwaves pass through another amplifier (HP 83020A) for an additional 23 dB of gain before returning to the network analyzer.

Table 3.4: Waveguide properties.

	Cutoff Frequency (GHz)	Frequency of Next Highest Mode (GHz)	Dimensions (mm)
X band	6.56	13.11	22.86 x 10.16 x 76
Ku band	9.49	18.98	15.80 x 7.90 x 76
K band	14.05	28.10	10.67 x 4.32 x 76

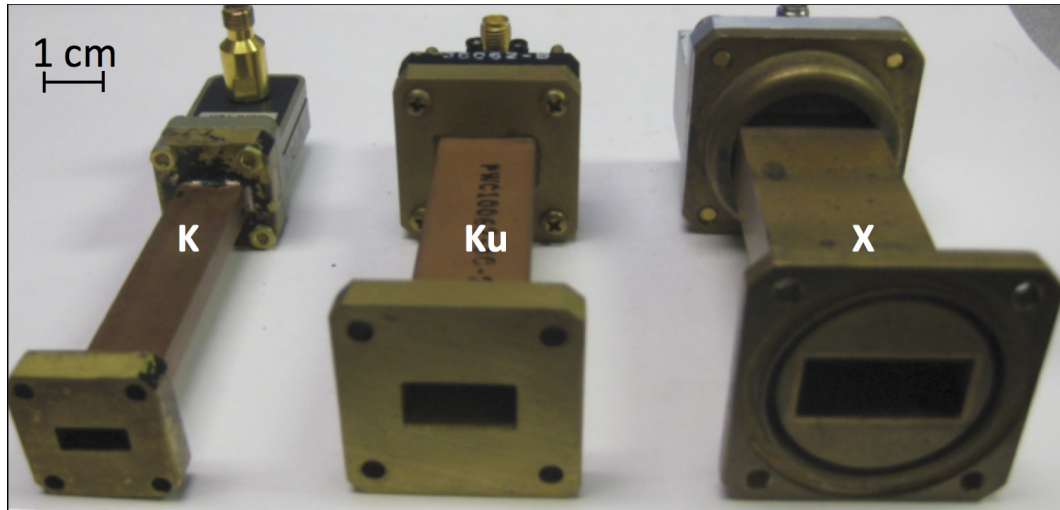


Figure 3.6: Waveguides.

3.3.2 Sample and Waveguide Mounting

The samples are mounted in waveguides that are clamped to the bottom of the 4 K plate and surrounded by magnetic shielding, which can be seen in Fig. 3.7 (b). Braided straps connect the base of the waveguides to the 4 K plate to provide additional thermal grounding. Switches allow multiple samples to be measured in each cooldown (there is room for two shielded waveguides).

Magnetic shielding is necessary because rf SQUIDs are extremely sensitive to magnetic field; their properties can change significantly even for fields smaller than $1 \mu\text{T}$. The waveguides are surrounded by a mu-metal cylinder 1 mm thick manufactured by Amuneal. There is also a 0.1 mm thick superconducting niobium open cylinder inside the smallest can of the cryostat.

The waveguides are attached to the 4 K plate with OHFC (oxygen free high conductivity) copper clamps, shown in Fig. 3.8 (a). A solenoid made from superconducting NbTi wire surrounds the waveguide with the clamp shown in Fig. 3.8 (c) providing additional thermal contact. The coil biases the SQUID by generating a perpendicular dc magnetic field.

A Lakeshore 340 temperature controller controls the temperature with heaters and thermometers on the waveguides. The heater attaches to the waveguide with the clamp shown in Fig. 3.8 (c).

The arrays of the Josephson junction-loaded wires are oriented so that the wires are parallel to the electric field in the waveguide, Fig. 3.10 (a). The samples are mounted in a OHFC copper piece (Fig. 3.9) that clamps between two K waveguides. The chips lie inside the pocket and the remaining area is filled with Rohacell (a foam with dielectric constant 1.07 at 10 GHz). The contact pads on the edges of the samples connect to wires for applying dc bias current; one of the contact pads attaches to the waveguide and the other is connected to a wire that passes through a hole in the waveguide.

The rf SQUIDs are oriented in the waveguide such that the magnetic fields are perpendicular to the plane of the SQUIDs see Fig. 3.10 (b). They are held in

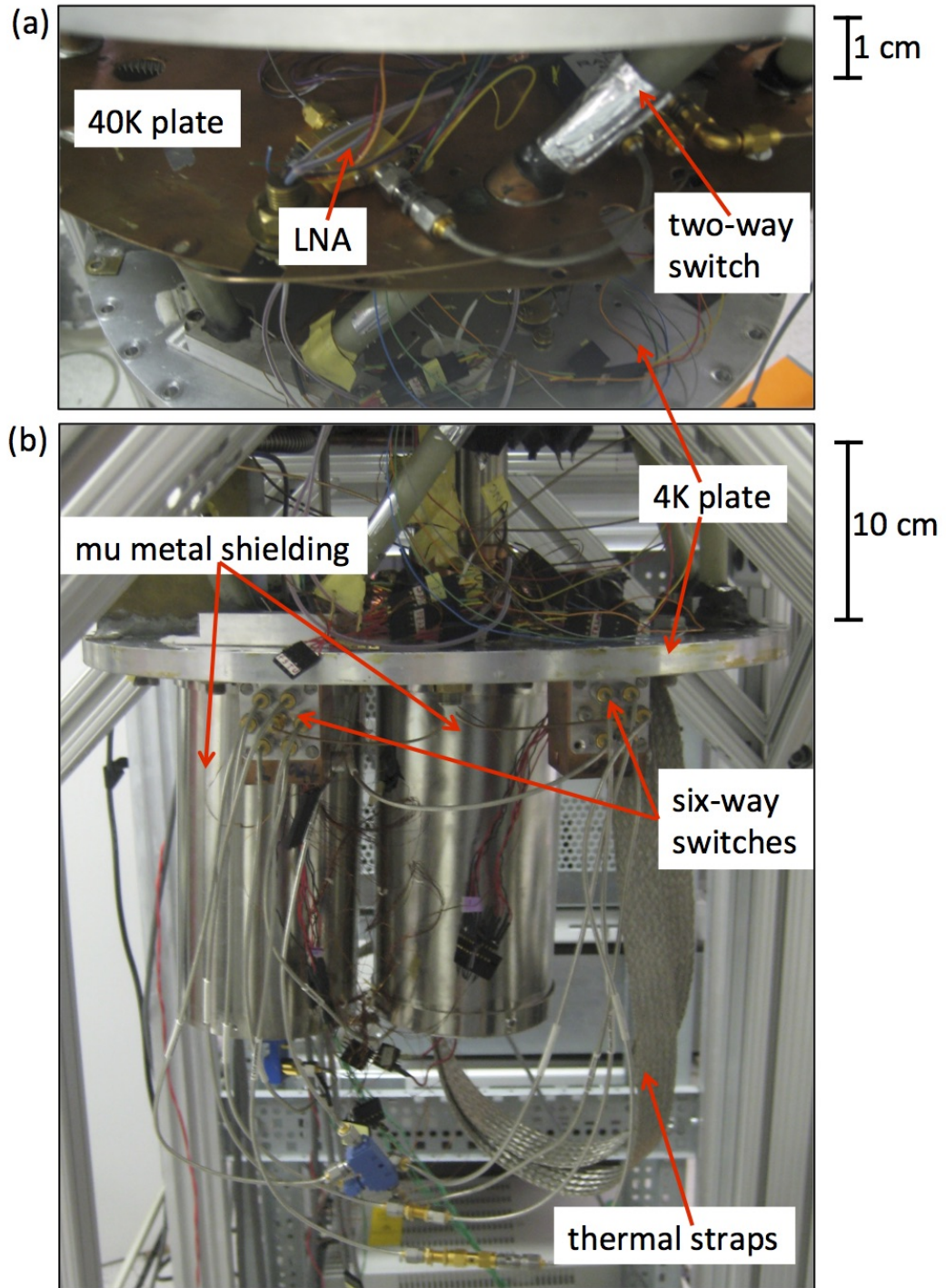


Figure 3.7: Interior of cryostat. (a) top of the 40 K plate. (b) the structures hanging below the 4 K plate.

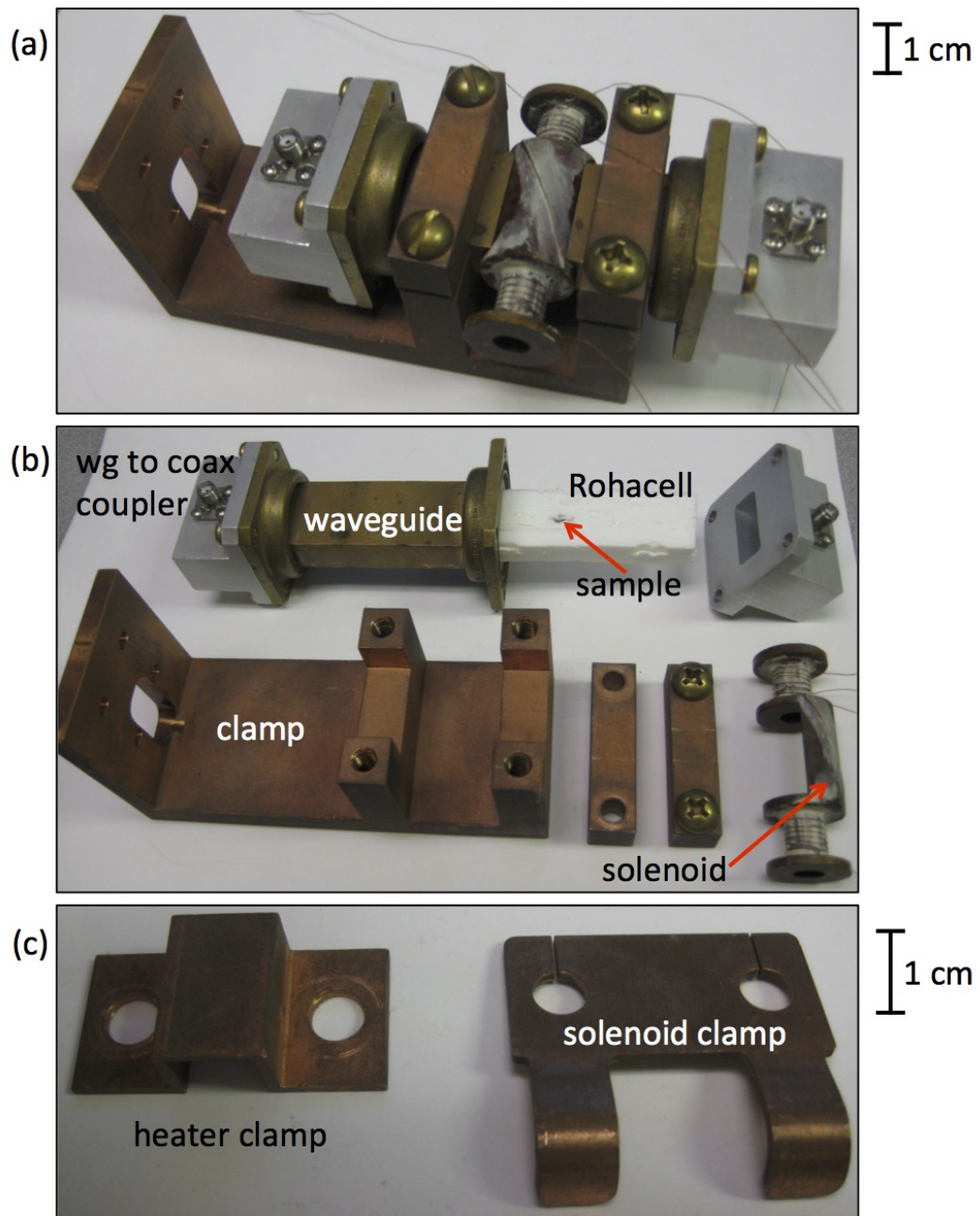


Figure 3.8: (a) X-band waveguide clamp assembled (b) and separated. (c) K clamps that secure heater and solenoid to the waveguide clamp

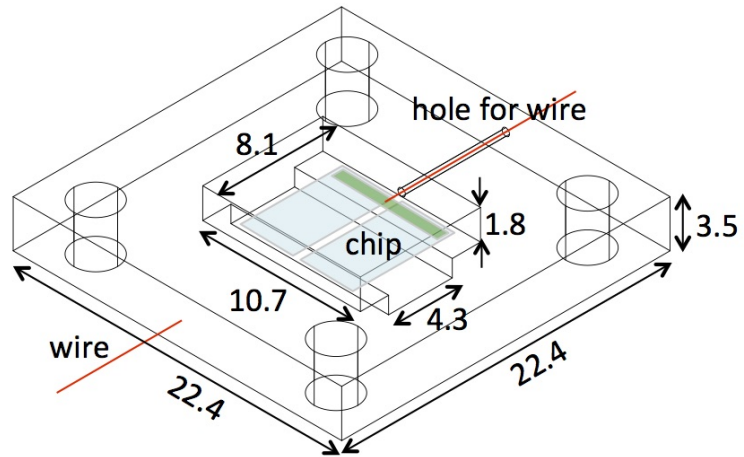


Figure 3.9: Mount for Josephson junction-loaded wire arrays. All dimensions in mm.

place by Rohacell which provides adequate mechanical stability but poor thermal contact, shown in Fig. 3.8 (b).

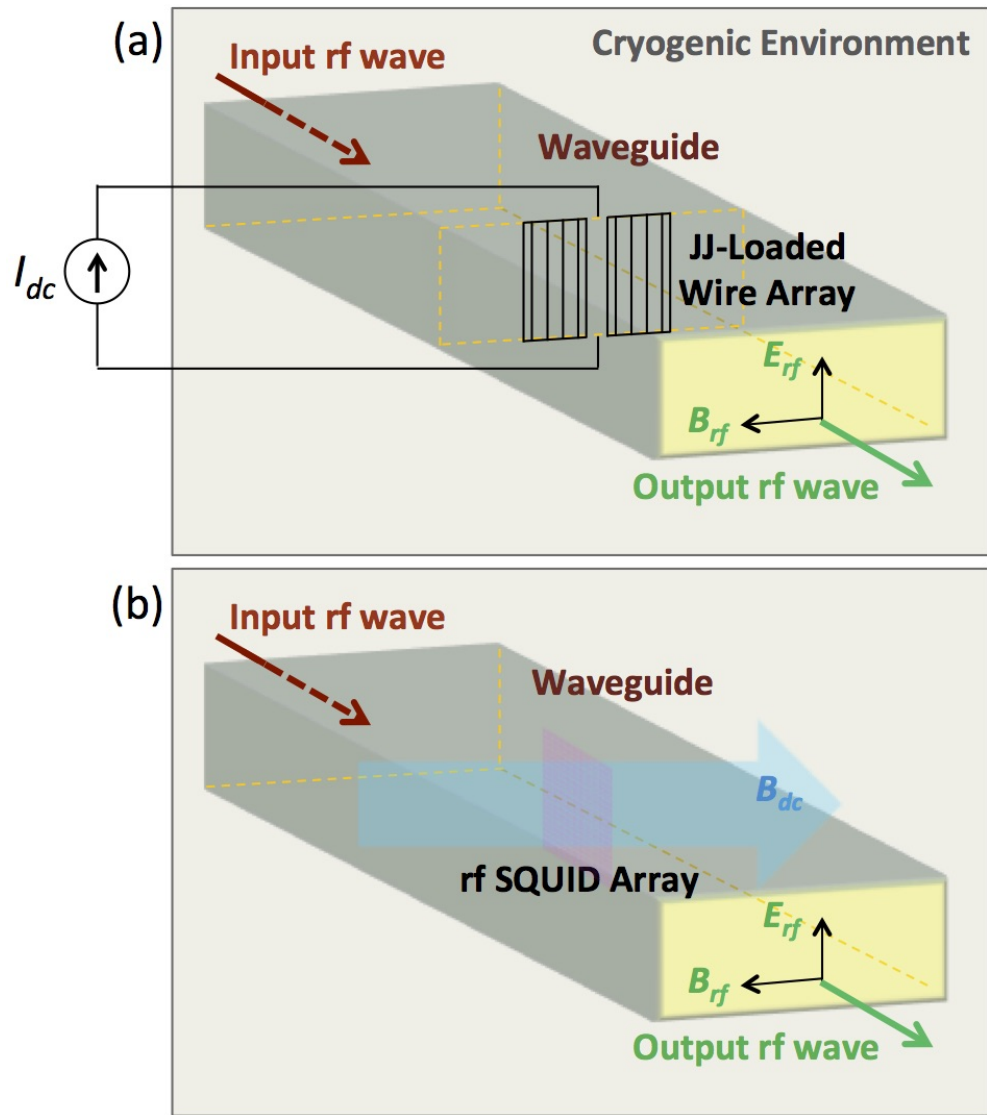


Figure 3.10: (a) orientation of the JJ-loaded wire array (b) and rf SQUIDs in the waveguide.

Chapter 4: Individual rf SQUID Measurements

To understand the rf SQUID metamaterial it is necessary to first understand a single meta-atom. In this chapter, I show with measurement and simulation results how the resonance of an rf SQUID tunes with dc magnetic field, temperature, and rf flux. This tunable resonance will allow for tunable effective permeability of the rf SQUID metamaterial.

4.1 Tunability with dc Flux

The measured tuning of the resonance with dc flux in the limit $\Phi_{rf}/\Phi_0 \ll 1$ is shown in Fig. 4.1 (a). The resonance dips in $|S_{21}(\omega)|$ appear as red features against a yellow background of unaffected (fully transmitted) signals ($|S_{21}| = 0$ dB). The signal was extracted by subtracting $|S_{21}|$ at 16 K (well above the critical temperature) from $|S_{21}|$ at 6.5 K, removing a background variation, and applying a threshold to identify the resonance. The small magnitude of the resonance dips can be attributed to the small size of the SQUID relative to the waveguide.

The resonance shows periodicity with dc flux, with a maximum resonant frequency of 16.9 ± 0.3 GHz and a minimum below 10 GHz. The cutoff frequency of the Ku waveguide imposes a lower frequency limit on this measurement. The minimum

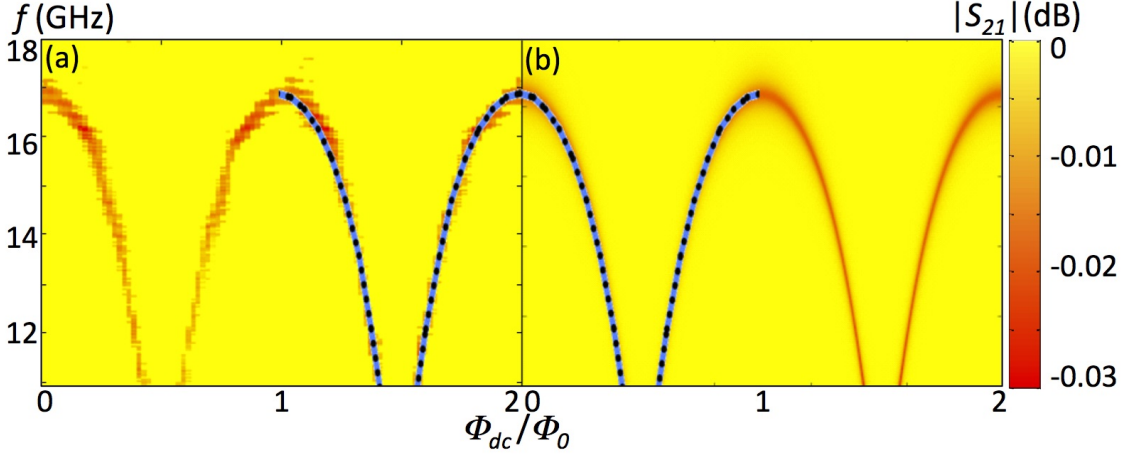


Figure 4.1: (a) Measured transmission of a single rf SQUID meta-atom as a function of frequency and dc flux at $T = 6.5$ K in the limit $\Phi_{rf}/\Phi_0 \ll 1$. The resonant response is indicated by the red features. (b) Simulated transmission from the effective medium method (Sec. 2.5.2). Black line: simulated minimum in $S_{21}(\omega)$. Blue line: resonant frequency from Eq. 1.14.

resonant frequency (measured in an X band waveguide) is 9.5 ± 0.5 GHz.

Treating the rf SQUID as an effective medium, simulated transmission is shown in Fig. 4.1 (b). The resonant frequency shows the same dc flux dependence in both the model and the data, which is emphasized by the lines that run through both parts of Fig 4.1. The model also replicates the depth and width of the resonant dip and how the shape of the resonance changes with dc flux, *i.e.* becoming wider near integer flux quanta. For details on how model parameters were chosen to match the

data see Sec. C.1.

The dc flux tuning of the SQUID meta-atom is remarkably sensitive. At its maximum value, the flux tunability (defined as the frequency change divided by the change in magnetic field) is approximately 80 THz/Gauss. Very little magnetic flux is necessary to make substantial changes in the properties of the meta-atom *e.g.* the effective permeability.

Simulations show that the effective permeability tunes with dc flux within the range of resonant frequencies, Fig. 4.2. Increasing dc flux can increase or decrease the effective permeability. The tuning is very frequency dependent and is most sensitive near the resonance. The biggest range of tuning occurs at $\Phi_{dc}/\Phi_0 = 1/2$ and the smallest at $\Phi_{dc}/\Phi_0 = 0$.

The effective permeability has a limited range of tuning for the same reason that the S_{21} signals are so small: this SQUID takes up only a small fraction of the waveguide, with a filling fraction F of only 0.0004. Increasing the number of SQUIDs and raising the filling fraction should increase the range of effective permeability.

4.2 Tunability with Temperature

The measured dc flux tuning of the resonance is modified by temperature, as shown in Fig. 4.3 (a). The flux tunability is reduced from 7 GHz at 6.5 K, to 3 GHz at 7.6 K, and 1 GHz at 8.3 K. The model predicts the reduction in dc flux tunability; the increased temperature suppresses the critical current which increases the magnitude of the Josephson inductance (Eq. 1.12) so that it has a smaller effect

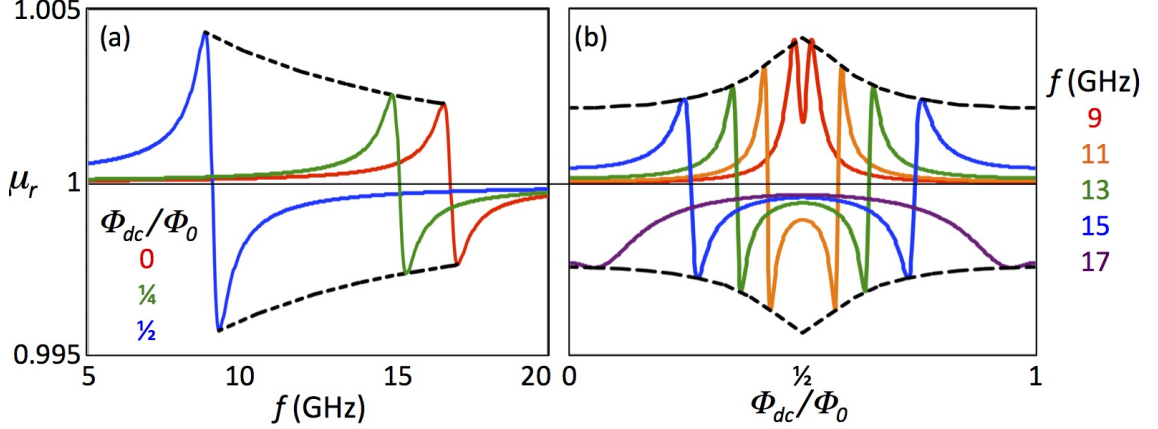


Figure 4.2: (a) Simulated relative effective permeability for a single rf-SQUID meta-atom in the limit $\Phi_{rf}/\Phi_0 \ll 1$ as a function of frequency at fixed dc flux (b) and dc flux at fixed frequency. Dashed lines follow the maximum and minimum values.

on the resonant frequency (Eq. 1.14).

I extracted the temperature dependence of the critical current $I_c(T)$ from the flux dependence of the resonant frequency at different fixed temperatures, Fig 4.3 (c). The critical current of the junction at each temperature was calculated by substituting the maximum resonant frequency as a function of flux into Eqs. 1.12 and 1.14. The results for $I_c(T)$ are consistent with previous results on Nb/ AlO_x /Al/Nb tunnel junctions [94].

Transmission as a function of frequency and dc flux was measured for various fixed temperatures; the extracted maximum (at $\Phi_{dc}/\Phi_0 = 0$) resonant frequencies and minimum (at $\Phi_{dc}/\Phi_0 = 1/2$) resonant frequencies (if above waveguide cutoff)

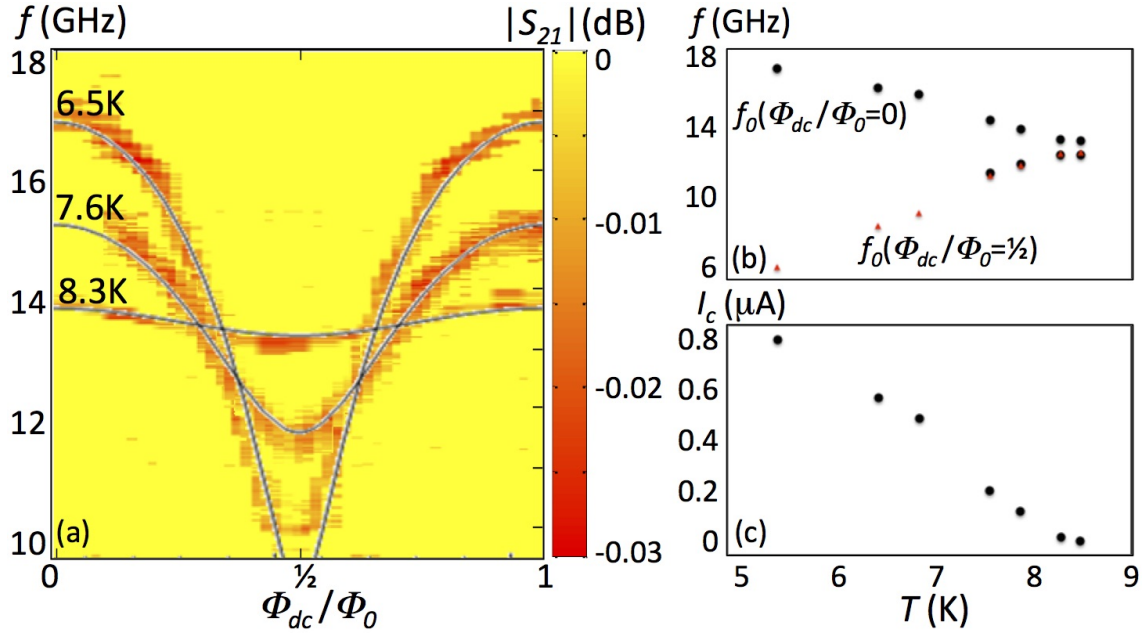


Figure 4.3: (a) Measured transmission of a single rf SQUID meta-atom as a function of frequency and dc flux at three temperatures in the limit $\Phi_{rf}/\Phi_0 \ll 1$. The solid lines are the resonant frequency from Eq. 1.14. (b) Maximum and minimum resonant frequency as a function of temperature, black dots: extracted from measurement, red triangles: from Eq. 1.14. (c) Critical current extracted from the measured maximum resonant frequency as a function of temperature.

are plotted in Fig 4.3. (In principle this measurement could be done by increasing temperature at a fixed dc flux. In practice changing the temperature also changes the dc flux because of the field generated by the current through the heater.) Increasing the temperature from 5.5 to 8.5 K decreases the maximum resonant frequency from 18 to 13.5 GHz and increases the minimum resonant frequency from < 9.5 to 13.5 GHz. In the high temperature limit the resonant frequency saturates at $f_{geo} = 13.5 \pm 0.2$ GHz regardless of applied dc flux as predicted by the model.

The slope of temperature tuning of f_0 can be large or small, and either positive or negative depending on the applied dc flux. The effective permeability is qualitatively similar to the resonant frequency. The effective permeability also has reduced dc flux tuning at higher temperatures and the slope of temperature tuning can take on a wide range of value depending on the dc flux and frequency, Fig 4.4.

4.3 Tunability with rf Flux

Increasing the magnitude of rf flux decreases the range of dc flux tunability, as shown in Fig. 4.5. The maximum resonant frequency (at $\Phi_{dc}/\Phi_0 = 0$) decreases monotonically with increased rf flux from its low rf flux value 16.5 GHz, to its high rf flux value $f_{geo} = 13.5$ GHz. The minimum resonant frequency (at $\Phi_{dc}/\Phi_0 = 1/2$) increases with increasing rf flux from its low rf flux value below the cutoff of the waveguide, to the same high rf flux value $f_{geo} = 13.5$ GHz. The saturation of the resonant frequency at f_{geo} in the high rf flux limit agrees with the model (see Sec. 2.2.2).

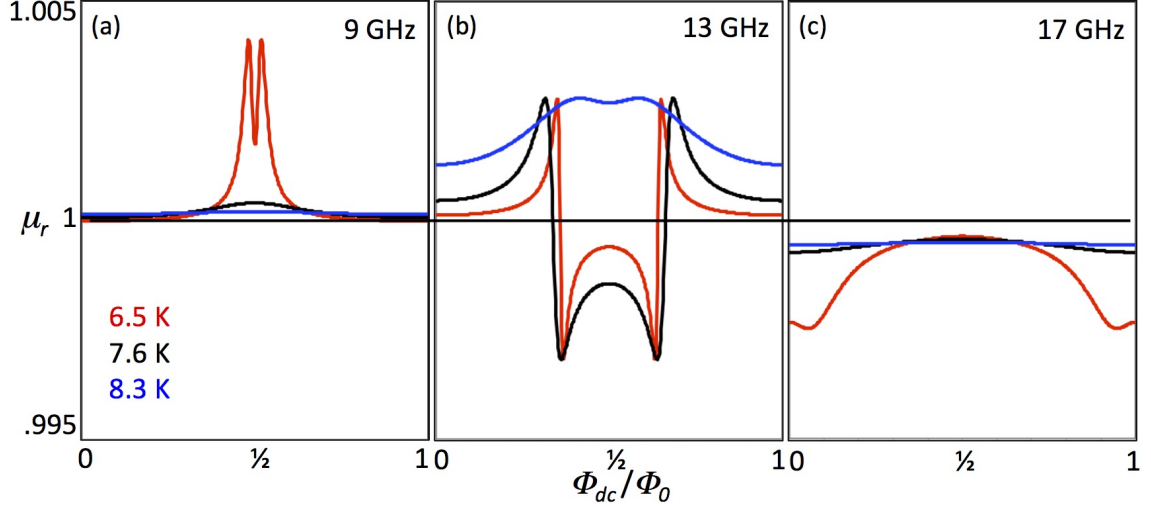


Figure 4.4: Simulated relative effective permeability of a single rf-SQUID meta-atom as a function of dc flux at various fixed temperatures and frequencies in the limit $\Phi_{rf}/\Phi_0 \ll 1$.

Like tuning with temperature, increasing the rf flux can either increase or decrease the resonant frequency, depending on the applied dc flux and at high rf flux the resonant frequency saturates at the geometric frequency $f_{0,geo} = 13.5$ GHz regardless of dc flux, Fig 4.6 (a). Simulated transmission, plotted in Fig. 4.6 (b), was calculated using the effective medium method (see Sec. 2.5.2) and the full numerical solution of the nonlinear equation (Eq. 2.8) (necessary outside of the low rf flux regime). The model agrees with the data, in terms of both the frequency and depth of the resonance.

Unlike with temperature tuning, the strength of the resonance response varies with rf flux, Fig. 4.6 (a). For the low dc flux case, when the rf flux is low

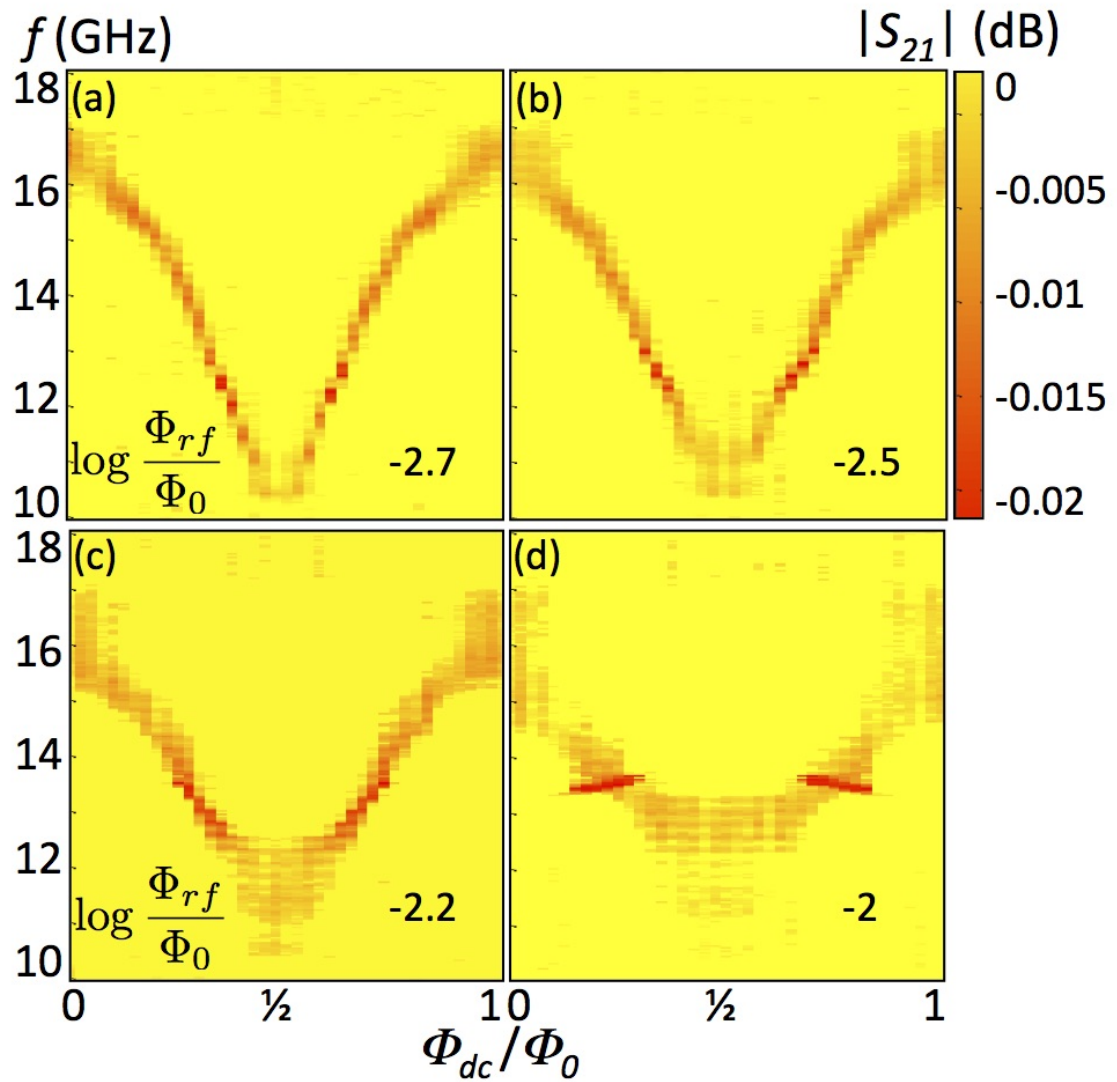


Figure 4.5: Measured transmission of a single rf-SQUID meta-atom as a function of frequency and dc flux for four different values of rf flux at fixed temperature $T = 6.5$ K.

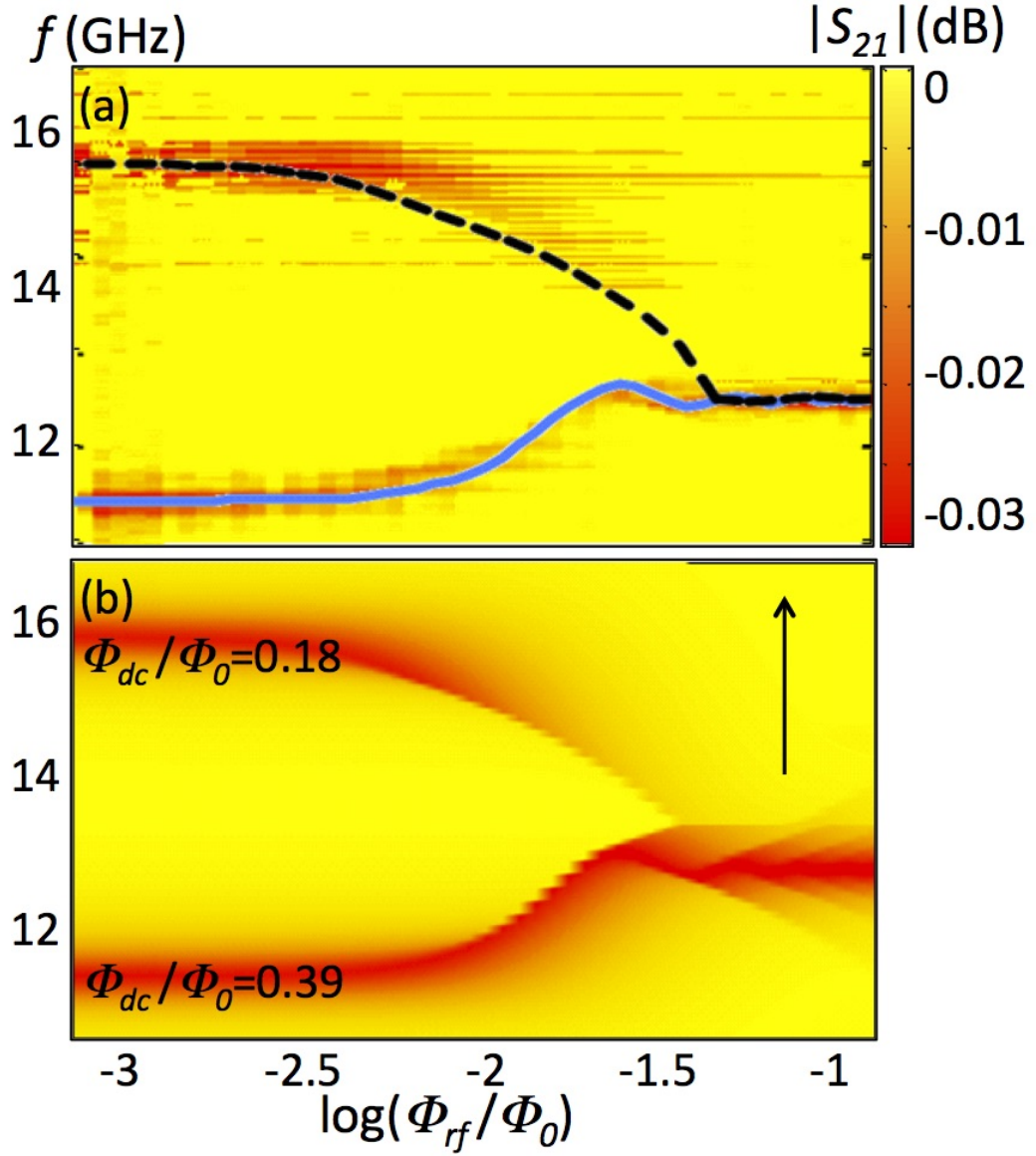


Figure 4.6: (a) Measured transmission of a single rf-SQUID meta-atom as a function of frequency and rf flux at two fixed dc flux values, and temperature $T = 6.5$ K. The lines indicate the model-determined resonant frequency (minimum of $|S_{21}(\omega)|$). (b) Simulated transmission using the effective medium calculation. Arrow indicates direction of frequency sweep.

($\log(\Phi_{rf}/\Phi_0) < -1.7$) the resonant frequency remains fixed at 16 GHz, and the resonance dip has a constant depth. The resonance does not change with increasing rf flux because S_{21} (Eq. 2.26) does not depend on input rf flux, $P_0 \propto V^2$ ($V \propto \Phi_{rf}$ in Eq. 2.12 and $\Phi_{rf} \propto \sqrt{P_0}$ in Eq. C.1). As the rf flux increases, the resonant frequency decreases and the resonance dip becomes shallower. The resonance disappears at intermediate rf flux; for details on the mechanism behind this transparent regime and its onset see [95]. The resonance reappears at high rf flux ($\log(\Phi_{rf}/\Phi_0) > -1$) where δ oscillates with an amplitude exceeding 2π on resonance and the Josephson junction undergoes multiple phase slips in each rf period. This is the high rf flux limit (Eq. 2.16), where the tunable resonant frequency reduces to a fixed value, $f_{0,geo} = 13.5$ GHz. The $S_{21}(\omega)$ dip is deep in this regime because the phase slips are dissipative and the losses are greater.

Similar behavior has been observed in single qubits coupled to microwave cavities containing a small number of photons [96, 97]. The Janes-Cummings Hamiltonian shows such behavior at high photon excitation number [98].

In the limit of low and high rf flux, the meta-atom has a resonant interaction with electromagnetic radiation, but at intermediate values of rf flux it becomes transparent. This effect is similar to metamaterial-induced transparency in which a tunable “spectral hole” is created by interfering resonant processes in two or more meta-atoms making up a meta-molecule [99–102]. The transparency in the superconducting meta-molecule could be suppressed in a switching transition at high rf flux [103]. For the rf SQUID, the transparency is due to the nonlinear Josephson effect and is self-induced, making it simpler than previous implementations.

Also unlike other realizations, the transparency arises from a decrease in dissipation without enhancement in loss at nearby frequencies [104]. As such the rf SQUID is potentially useful as a power limiter for sensitive front-end receivers [105].

The model predicts that the transparency depends on whether rf flux is increasing or decreasing as shown in Fig. 4.7 (b). In the model the SQUID is in a transparent state for increasing rf flux and a dissipative state for decreasing rf flux. However, the measurement of a single SQUID does not show this hysteretic dependence; the SQUID is in a transparent state regardless of rf sweep direction, Fig. 4.7 (a). (The expected hysteresis is apparent in some measurements of SQUID arrays, Sec. 5.2.3).

The only hysteresis apparent in the measurement of a single SQUID is the onset of the geometric resonance, the border between the yellow and orange regions of Fig. 4.8. At zero dc flux where the hysteresis is greatest, the onset of the geometric frequency occurs at $\log \Phi_{rf}/\Phi_0 = -2.5$ for increasing rf flux, but for decreasing rf flux the transition occurs at $\log \Phi_{rf}/\Phi_0 = -2.25$. This hysteresis is contained in the model and reflects the sensitivity to initial conditions of the solution to the nonlinear differential equation (Eq. 2.8). For details on how initial conditions are handled in the simulation see Sec. D.

Figure 4.7 (c) shows how the effective permeability tunes with rf power. There is a reduction in the range of effective permeability in the transparent region as the maximum of $\mu(\omega)$ decreases and the minimum of $\mu(\omega)$ increases. As with transmission, the effective permeability is sensitive to rf flux tuning in the transparent region and insensitive to rf flux in the low and high rf flux limits.

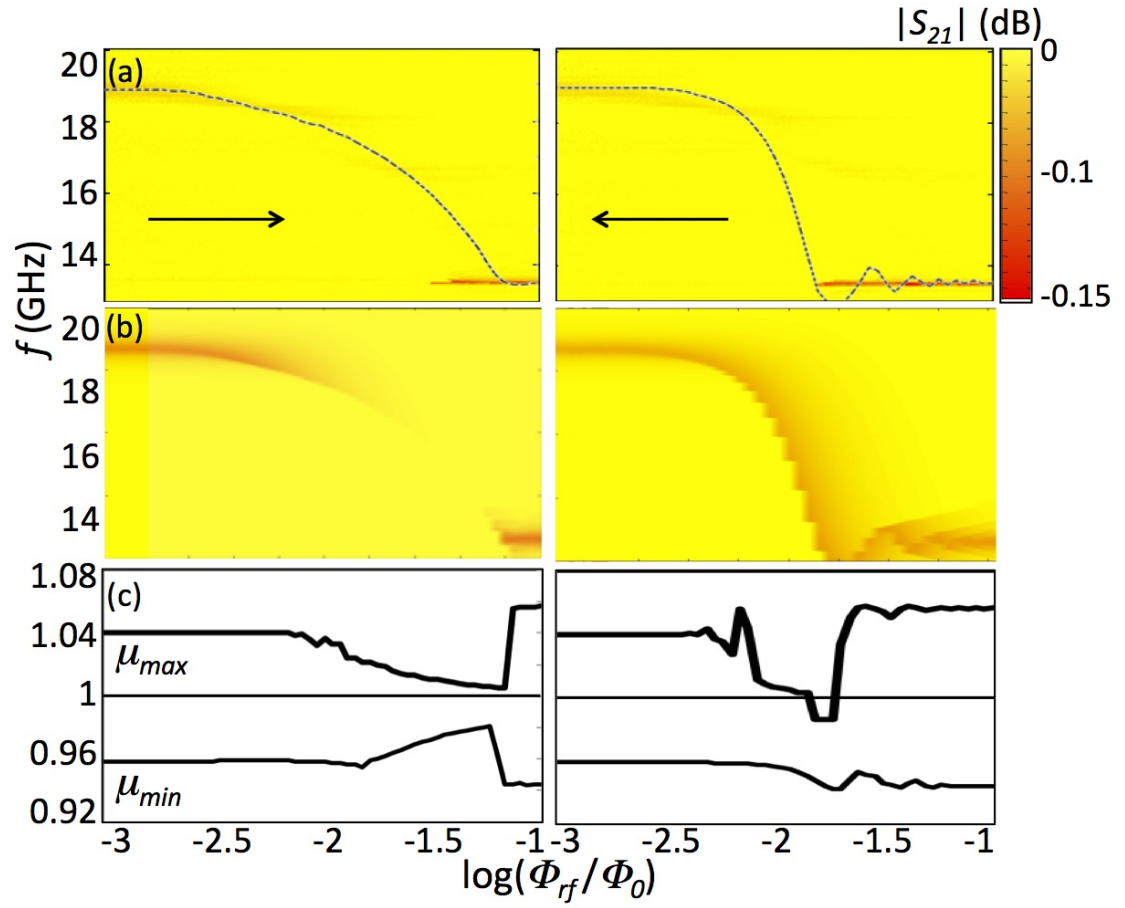


Figure 4.7: (a) Measured (b) and simulated transmission as a function of frequency and increasing and decreasing rf flux at $\Phi_{dc}/\Phi_0 = 0$ and $T = 4.5$ K. The dashed line indicates the model-determined resonant frequency (minimum of $|S_{21}(\omega)|$). Arrows indicate rf flux sweep direction. (c) Simulated maximum and minimum of effective permeability.

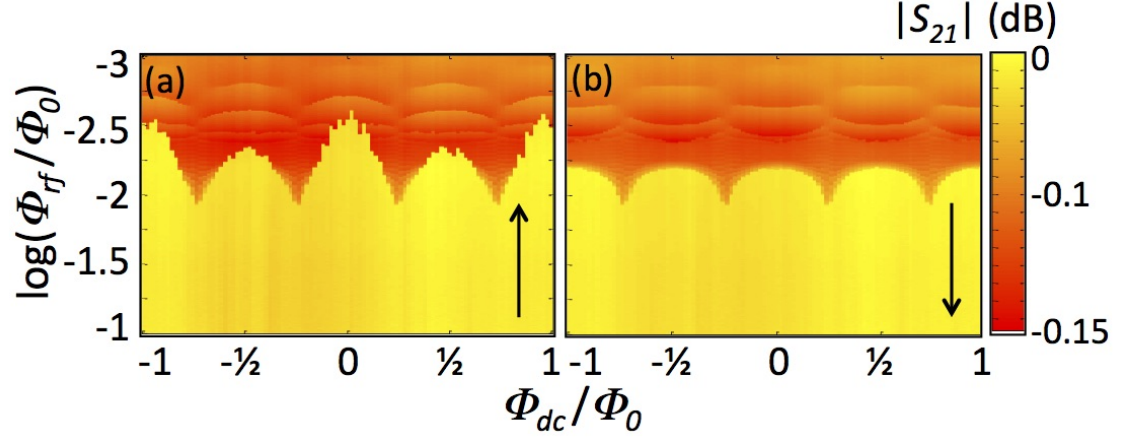


Figure 4.8: Measured transmission for a single rf-SQUID meta-atom as a function of (a) increasing (b) and decreasing rf flux and dc flux at the geometric frequency and $T = 5.5$ K. The border between the yellow and orange regions indicates the onset of the geometric resonance. Arrows indicate rf flux sweep direction.

4.4 Tuning Speed

The shortest time scale for tuning a superconductor without destroying the superconducting state is $\hbar/\Delta \sim 1$ ps, where Δ is the energy gap. The RC time constant of the SQUID is 0.3 ns (L/R time constant 0.4 ps) which imposes an upper limit on the intrinsic switching speed. Tuning with temperature depends on changes to the critical current of the junction and is relatively slow, on the order of $10 \mu\text{s}$ [106].

A pulsed rf flux measurement of the SQUID meta-atom is consistent with a

response time less than 500 ns. Hence the rf flux tuning time is in the sub- μ s range perhaps only limited by the RC time. Flux tuning of SQUID-like superconducting qubits has been accomplished on nano-second time scales limited only by the rise-time of the applied current pulse [107, 108]. Tuning the Josephson inductance with applied flux is much faster than tuning the kinetic inductance of previous superconducting metamaterials.

4.5 Summary

I found that individual rf SQUIDs exhibit the overall behavior that I expect. The resonance and effective permeability of an individual rf SQUID tune over a wide range with dc flux, temperature, and rf flux. The dc flux tuning can be achieved at high speeds. I designed the SQUIDs for this behavior with the intension of making a superior tunable superconducting metamaterial. In addition to the tunable effective permeability I set out to achieve, the individual rf SQUID meta-atom also exhibited a novel transparency feature at intermediate rf flux.

Chapter 5: rf SQUID Array Measurements

In this chapter, I compare the behavior of 2D rf SQUIDs with that of a single rf SQUID. The arrays exhibit similar tuning behavior, but have additional features which impact their behavior: coupling between the SQUIDs, additional magneto-inductive resonant modes, and disorder. I begin with a discussion of two coupled rf SQUIDs.

5.1 Pair of rf SQUIDs

No experiments were performed on a pair of rf SQUIDs; the scenario was only explored in simulation to bridge the gap between individual SQUIDs and arrays. The primary difference between one SQUID and two SQUIDs is the coupling between them. This coupling causes an increase in the resonant frequency and the depth of the $S_{21}(\omega)$ resonance dip which can be shown analytically as follows.

If the SQUIDs are identical $I_1 = I_2$ and Eq. 2.17 becomes

$$\Phi = \Phi_{app} - L_{eff}I \quad (5.1)$$

where the effective inductance $L_{eff} = L + M = L(1 + \kappa_0)$ is less than the self-inductance of the SQUID (because $M < 0$).

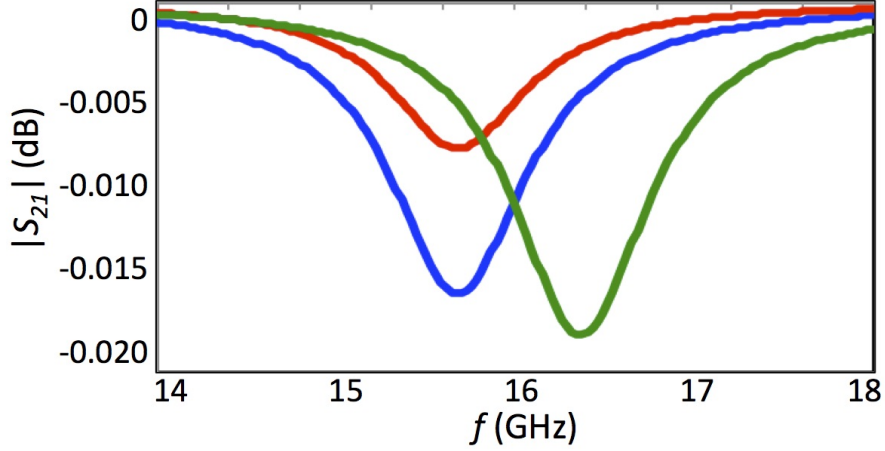


Figure 5.1: Simulated transmission in the limit $\Phi_{rf}/\Phi_0 \ll 1$ using dissipated power method; red) a single SQUID; blue) two identical uncoupled SQUIDs; green) two identical strongly coupled SQUIDs, $|\kappa_0| = 0.06$.

The resonant frequency is given by

$$f_0 = \frac{1}{2\pi \sqrt{\left(\frac{1}{L_{eff}} + \frac{1}{L_{JJ}}\right)^{-1} C}} \quad (5.2)$$

A decrease in the effective inductance causes an increase in the resonant frequency and the quality of the resonance, Fig. 5.1. The resonance of two uncoupled SQUIDs (blue curve) occurs at the same frequency and exactly twice the depth of a single SQUID (red curve), but when the SQUIDs are strongly coupled (green curve) the resonance dip becomes deeper and shifts to a higher frequency.

How much the resonant frequency shifts depends on the dc flux. Equations 2.13 and 2.14 for the maximum and minimum resonant frequency values can be

modified to include coupling:

$$f_0 \left(\frac{\Phi_{dc}}{\Phi_0} = 0 \right) = f_{geo} \sqrt{\frac{1}{\kappa_0} + \beta_{rf}} \quad (5.3)$$

$$f_0 \left(\frac{\Phi_{dc}}{\Phi_0} = \frac{1}{2} \right) = f_{geo} \sqrt{\frac{1}{\kappa_0} - \beta_{rf}} \quad (5.4)$$

Coupling decreases the dc flux tunability because the maximum frequency increases less than the minimum. The effect is small for the parameter values chosen here with a range of 7.8 GHz at no coupling and 7.5 GHz at strong coupling $|\kappa_0| = 0.06$.

The effective geometric resonant frequency (*i.e.* in the high temperature and high rf flux limits) also increases with coupling

$$f_{geo,eff} = \frac{1}{2\pi\sqrt{L_{eff}C}} = \frac{1}{2\pi\sqrt{(1+\kappa_0)LC}} = \frac{f_{geo}}{\sqrt{1+\kappa_0}} \quad (5.5)$$

With more than one SQUID the possibility arises for them to be non-identical, which gives rise to different resonant modes. Consider the case of two SQUIDs with identical parameters but with different dc flux bias, one with $\Phi_{dc}/\Phi_0 = 0$ and the other $\Phi_{dc}/\Phi_0 = 1/4$. In the uncoupled case, illustrated in Fig 5.2 (a-c), each SQUID does exactly what it would if alone; transmission is simply the sum of each individual SQUID, the phase of each SQUID shifts by π on resonance, and the coherence is suppressed between the two resonant frequencies.

When the SQUIDs are strongly coupled, illustrated in Fig 5.2 (d-f), the resonant oscillation of one SQUID affects the other so that both SQUIDs are oscillating at both resonant frequencies. These modes resemble those of any two linear coupled oscillators; there is one mode where both SQUIDa are in phase and another mode where there is a π phase difference between them, Fig. 5.2 (e). At the higher resonant frequency, where the SQUIDs are oscillating in phase and coherent, the $S_{21}(\omega)$

dip is deeper because this mode has a relatively large magnetic moment and is easily excited by the uniform driving force. At the lower frequency the SQUIDs are out of phase by π and relatively incoherent. This resonant mode has a lower magnetic moment making it harder for the uniform drive to excite and consequently having a smaller dip in $S_{21}(\omega)$.

For both coupled and uncoupled SQUIDs the coherence is suppressed by the same amount and over a comparable range of frequencies. However when the SQUIDs are coupled the coherence curve shifts lower in frequency such that the higher resonance is coherent ($r_A \approx 1$) and the lower resonance is relatively incoherent; compare Fig. 5.2 (c) and Fig. 5.2 (f).

When the rf flux is increased at fixed frequency, the primary mode (with the SQUIDs in phase) eventually dominates, regardless of the dominant mode in the limit $\Phi_{rf}/\Phi_0 \ll 1$ and regardless of the coupling between the SQUIDs, Fig. 5.3. Increasing rf flux at the frequency that the lower mode dominates in the limit $\Phi_{rf}/\Phi_0 \ll 1$ causes an initial decrease in the coherence; the SQUIDs are being stimulated at a frequency between the resonances (where coherence is low) because increasing rf flux shifts both resonances lower. When the rf flux increases to the point where both SQUIDs are being driven at a frequency higher than their resonant frequency the coherence saturates at $r_A = 1$. The higher the coupling the higher the rf flux must be before this transition occurs.

The coupling between two identical SQUIDs does not have a strong effect on the magnitude of the transparency but it does affect the range of rf flux over which transparency occurs. The transparency can be quantified as $U = 1 - S_{21}/S_{21,lin}$

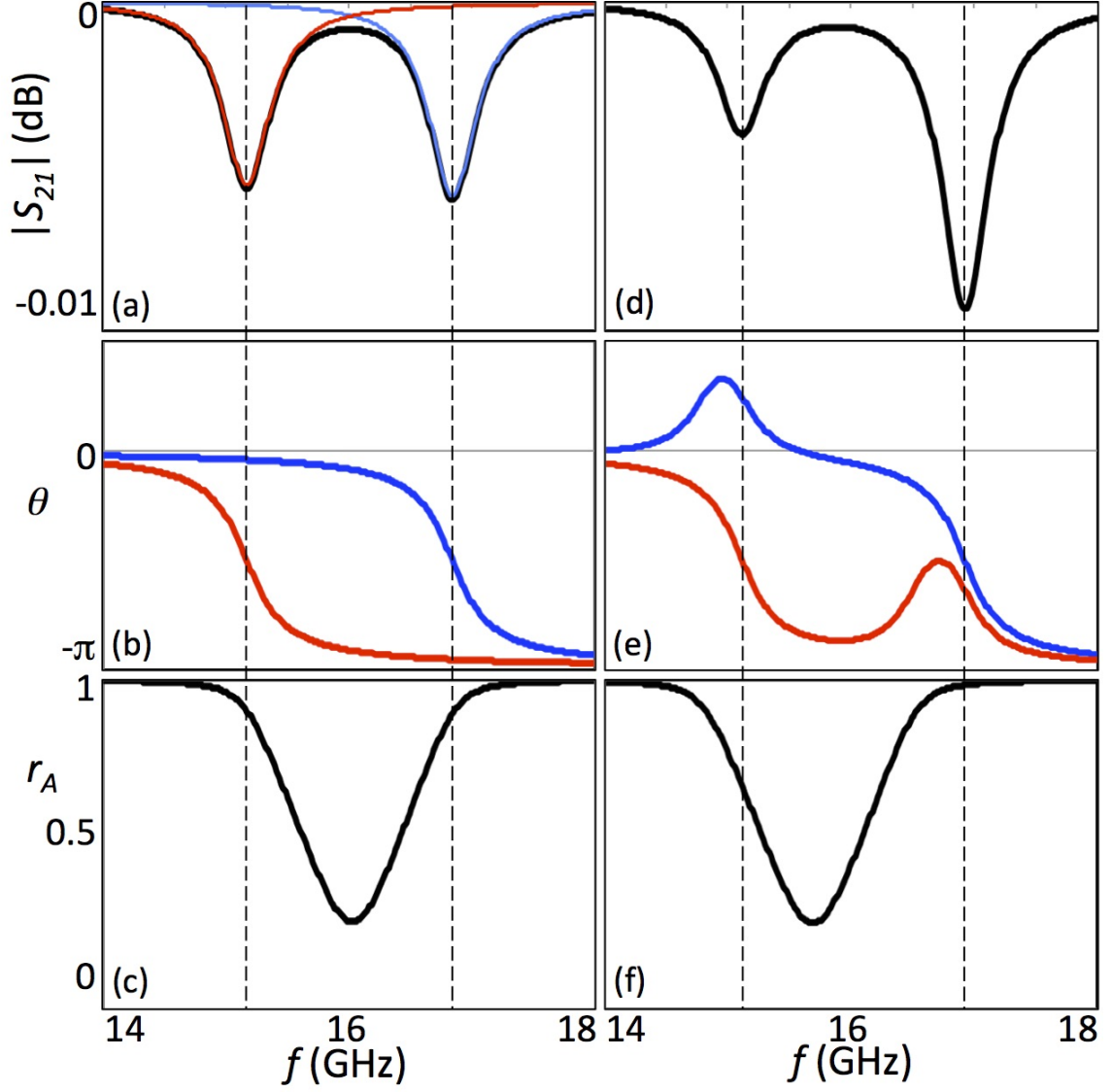


Figure 5.2: Simulated transmission, phase of oscillation, and coherence for two identical SQUIDs with different dc flux bias, one with $\Phi_{dc}/\Phi_0 = 0$ and the other $\Phi_{dc}/\Phi_0 = 1/4$. (a-c) The SQUIDs are uncoupled. (d-f) The SQUIDs are strongly coupled, $|\kappa_0| = 0.06$.

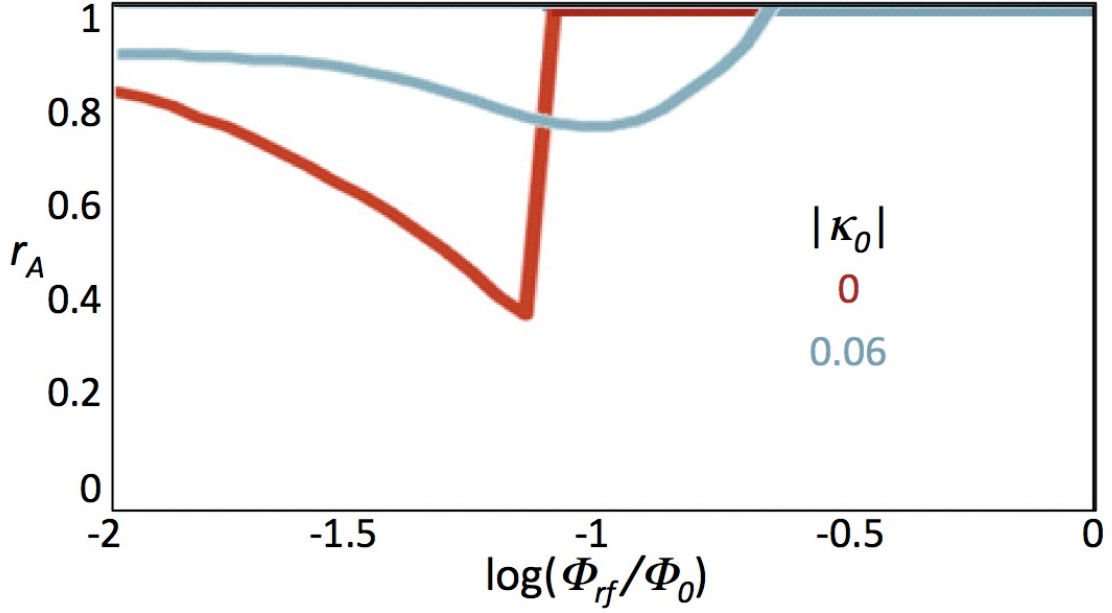


Figure 5.3: Simulated coherence as a function of rf flux for two identical SQUIDs for two values of coupling at the frequency that the lower mode dominates in the limit $\Phi_{rf}/\Phi_0 \ll 1$.

where both S_{21} values are evaluated on resonance at associated rf flux driving levels. The coupling strength does not affect the magnitude of transparency, Fig. 5.4 (a). The effective coupling, *i.e.* the ratio of flux from the neighboring SQUID to the rf driving flux, is low in the transparent region (where rf flux is high) regardless of the strength of the coupling in the low flux limit. Transparency is observed in single SQUIDs and with low effective coupling the SQUIDs behave individually.

Coupling between the SQUIDs affects the range of rf flux over which transparency occurs. Figure 5.4 (a) shows that coupling does not strongly affect the

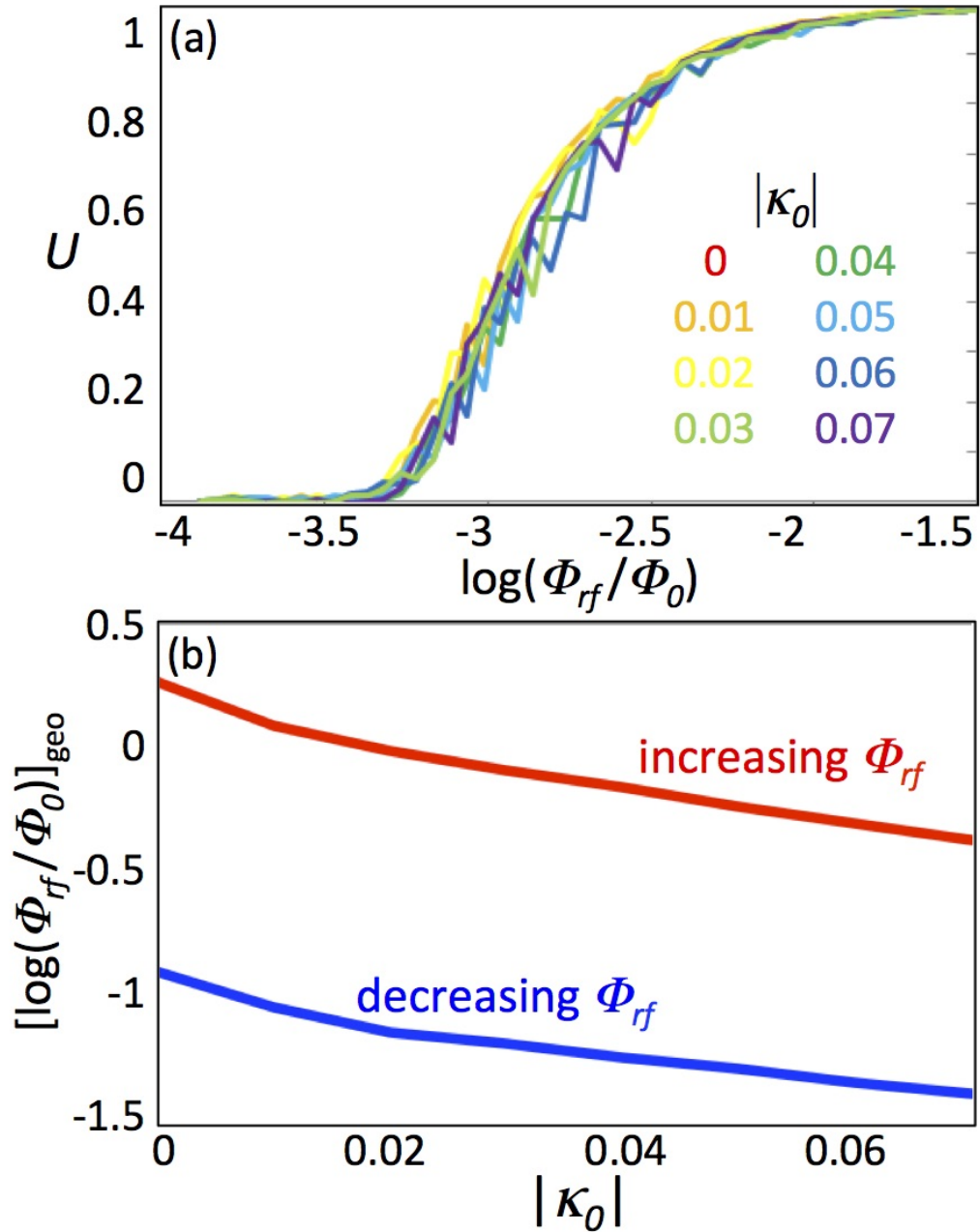


Figure 5.4: (a) Simulated transparency as a function of rf flux for two identical SQUIDs for various coupling values. (b) The onset of the geometric resonance for increasing and decreasing rf flux as a function of coupling.

onset of transparency, but it does affect the onset of the geometric resonance, Fig. 5.4 (b). When the coupling between SQUIDs is larger, the onset of the geometric resonance occurs at lower rf flux, decreasing the range of rf flux over which transparency occurs. The width of the hysteresis loop (the difference between the red and blue curves in Fig. 5.4 (b)) also decreases with coupling. For further analysis of a pair of rf SQUIDs in the case of higher rf flux see Sec. E.2.

5.2 rf SQUID Arrays

A 2D rf SQUID array (like a single SQUID) tunes with dc flux, temperature, and rf flux. The temperature dependence of dc flux tuning for the 27x27 rf-SQUID array is similar to what was observed in the single-SQUID case; compare Fig. 5.2 with Fig. 4.3. The resonant frequency tunes periodically with dc flux and there is a reduction in dc flux tunability with increased temperature, Fig. 5.2 (a); tuning is reduced from > 6.5 GHz at 6.5 K to 2.5 GHz at 7.9 K. The resonance can increase or decrease with temperature depending on the dc flux value, Fig. 5.2 (b) and the critical current drops with increased temperature, Fig. 5.2 (c).

The rf flux dependence of the dc flux tunability also resembles the single-SQUID case; compare Fig. 5.6 with Fig. 4.5. The dc flux tunability of the resonance decreases with increased rf flux and saturates at the geometric resonance in the high rf flux limit.

Compared to a single rf SQUID, an array shows a similar response to each tuning parameter but with a stronger signal because the array has a larger filling

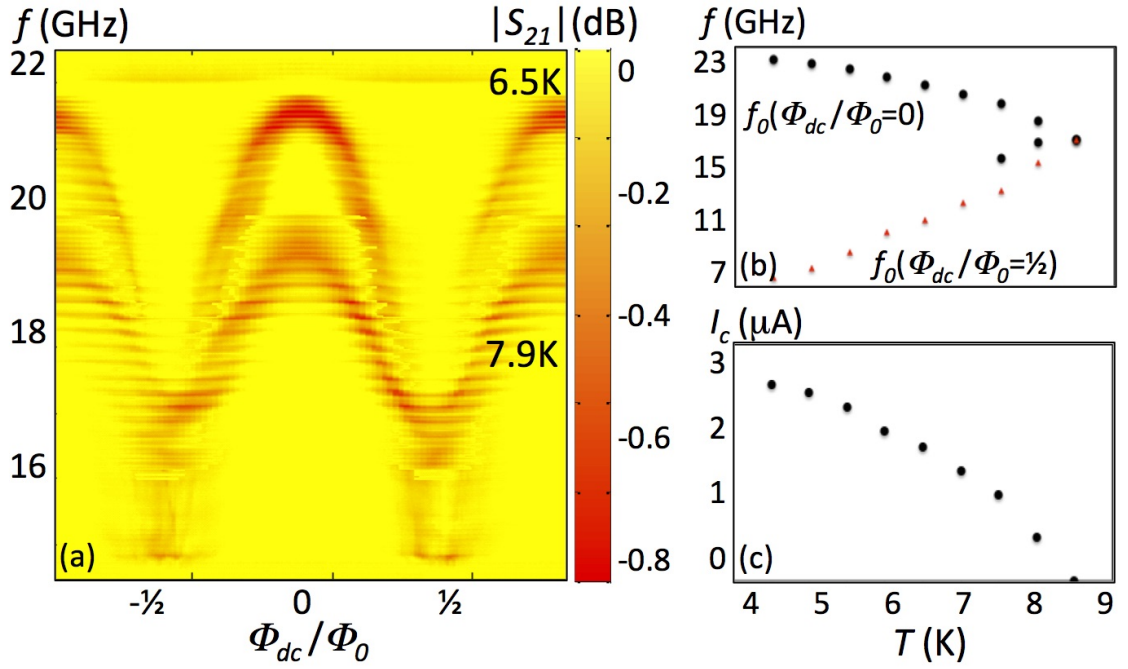


Figure 5.5: (a) Measured transmission of the 27x27 rf SQUID array as a function of frequency and dc flux at two temperatures in the limit $\Phi_{rf}/\Phi_0 \ll 1$. (b) Maximum and minimum resonant frequency as a function of temperature, black dots: extracted from measurement, red triangles: calculated from Eq. 1.14. (c) Critical current extracted from the measured maximum resonant frequency as a function of temperature.

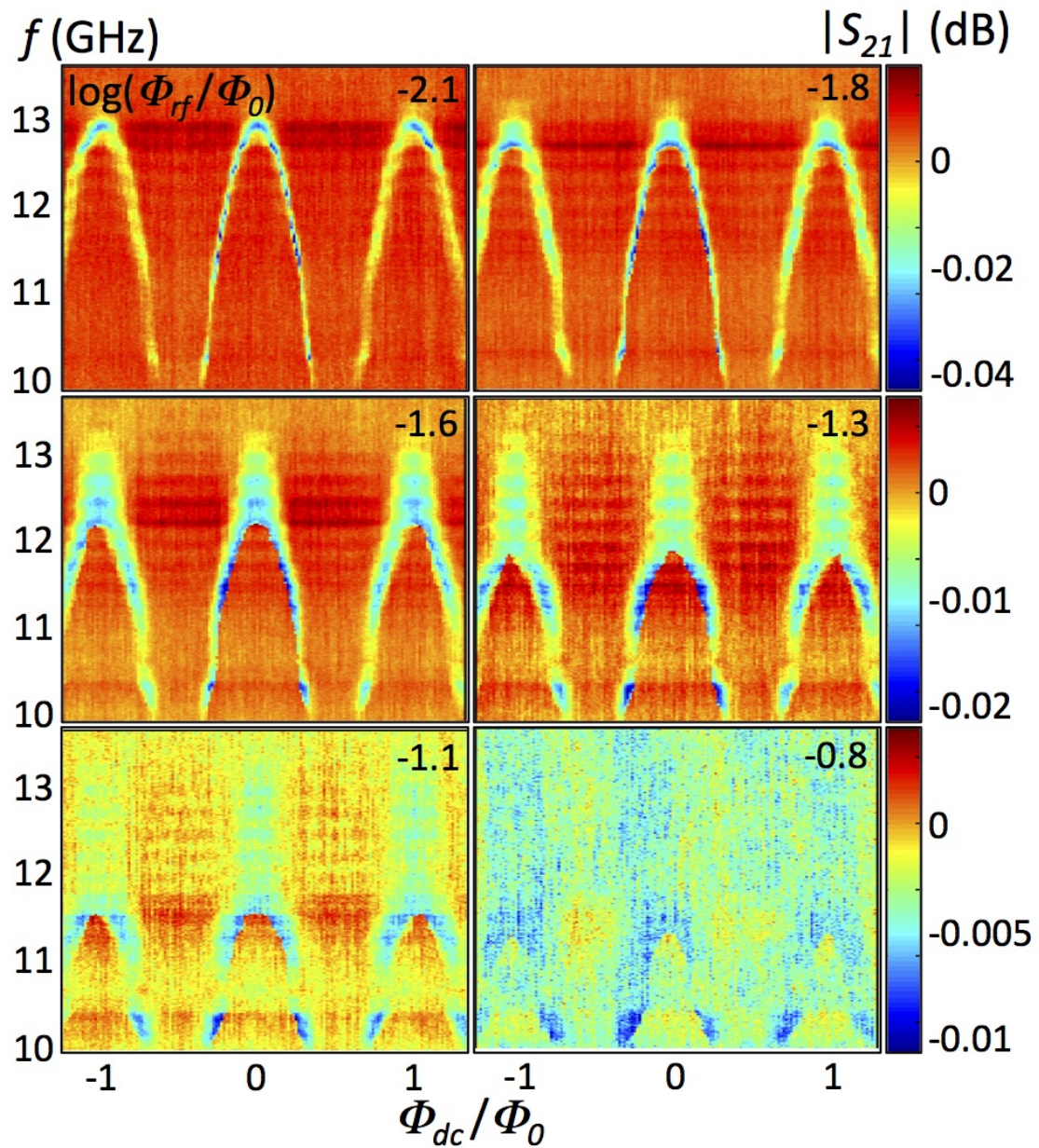


Figure 5.6: Measured transmission of a 21x21 array with $|\kappa_0| = 0.006$ as a function of frequency and dc flux, at various rf flux values.

fraction. However, like the two-SQUID case, there are additional effects to consider in an array *i.e.* coupling between the SQUIDs, additional resonant modes, and the possibility for dc flux disorder.

5.2.1 Coupling

Just as in the two-SQUID case, coupling increases the resonant frequency and deepens the resonance dip, but the effect is stronger with more SQUIDs. It's important to consider coupling between every pair of SQUIDs not just between nearest neighbors as illustrated in Fig. 5.7. Compared to the case of no coupling, nearest-neighbor coupling shifts the frequency by 0.3 GHz and deepens the dip by -0.006 dB. Considering coupling between all pairs shifts the frequency by 0.7 GHz and deepens the dip by -0.02 dB. (The additional minima at lower frequencies are indicative of magneto-inductance resonant modes discussed in Sec. 5.2.2.)

The quality factor Q (and the depth of the $S_{21}(\omega)$ dip) scales with array size and coupling as shown in Fig. 5.8. A similar increase in Q as a function of array size is seen in ASR (asymmetric split ring) arrays driven by a plane wave [109]. According to Fedotov *et al.* the quality of the resonance for a coherent metamaterial scales with the size of the array because larger arrays store more energy in magneto-inductive waves without a proportional increase in radiation losses. A similar mechanism is at play in SQUID arrays.

As in the two-SQUID case, coupling increases the resonant frequency by decreasing the effective inductance $L_{eff} = \kappa_{avg}L$ where κ_{avg} is the sum of the elements

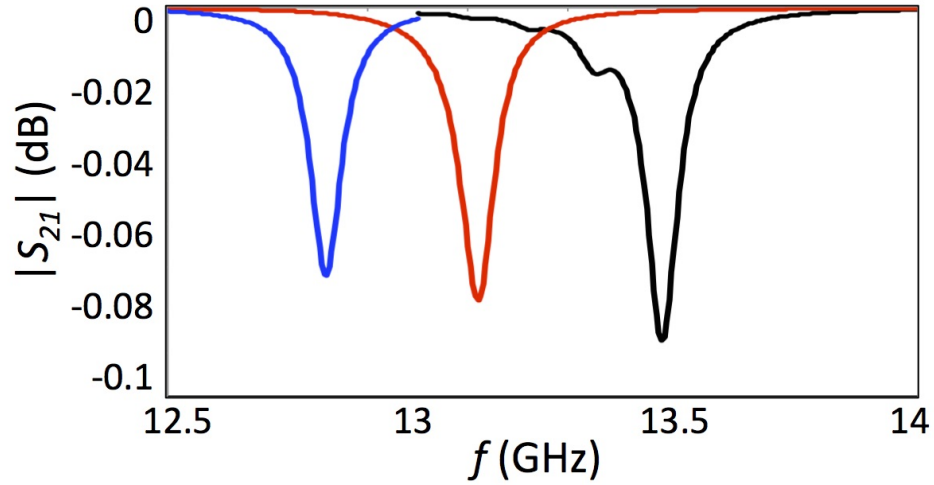


Figure 5.7: Simulated transmission (using the dissipated power method) as a function of frequency for a 21x21 array in the limit $\Phi_{rf}/\Phi_0 \ll 1$ and $\Phi_{dc} = 0$. (blue) no coupling. (red) $|\kappa_0| = 0.02$ with nearest neighbor coupling only. (black) $|\kappa_0| = 0.02$ including coupling between every pair of SQUIDs.

of $\bar{\kappa}/N$, ($0 < \kappa_{avg} \leq 1$. When there is no coupling $\kappa_{avg} = 1$.) Equations 5.3 and 5.4 for the maximum and minimum values of resonant frequency for two coupled SQUIDs can be extended to an array.

$$f_0 \left(\frac{\Phi_{dc}}{\Phi_0} = 0 \right) = f_{geo} \sqrt{\frac{1}{\kappa_{avg}} + \beta_{rf}} \quad (5.6)$$

$$f_0 \left(\frac{\Phi_{dc}}{\Phi_0} = \frac{1}{2} \right) = f_{geo} \sqrt{\frac{1}{\kappa_{avg}} - \beta_{rf}} \quad (5.7)$$

As in the two-SQUID case, increasing coupling decreases the range of dc flux tunability.

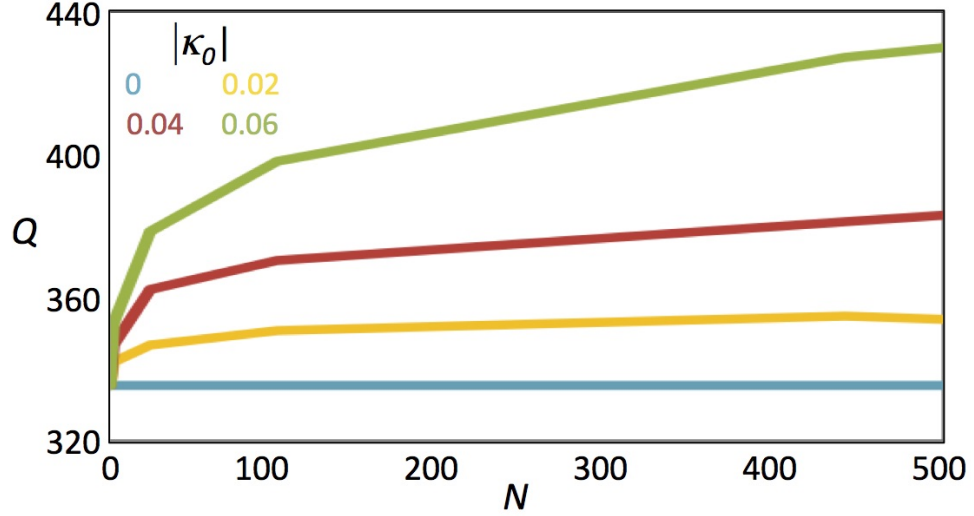


Figure 5.8: Simulated quality of the primary resonance as a function of array size for different values of coupling between the SQUIDs for a 21x21 array in the limit $\Phi_{rf}/\Phi_0 \ll 1$.

The relationship between coupling and resonant frequency for various dc flux is demonstrated in Fig. 5.9 (a). Transmission was measured as a function of frequency and dc flux for both loosely and tightly coupled 21x21 arrays. The resonant frequency was extracted by taking the frequency of the minimum in $S_{21}(\omega)$ at each dc flux value, the black dots in Fig. 5.9 (a). The numerical results (solid lines), extracted from simulated S_{21} (Sec. 2.5.1), agree with these data. As predicted analytically by Eqs. 5.6 and 5.7 (dashed lines in Fig. 5.9 (a)), increased coupling decreases the range of dc flux tunability; at zero coupling there is 8 GHz of tunability and at maximum coupling there is 5 GHz.

Measured, simulated, and analytical results show the relationship between

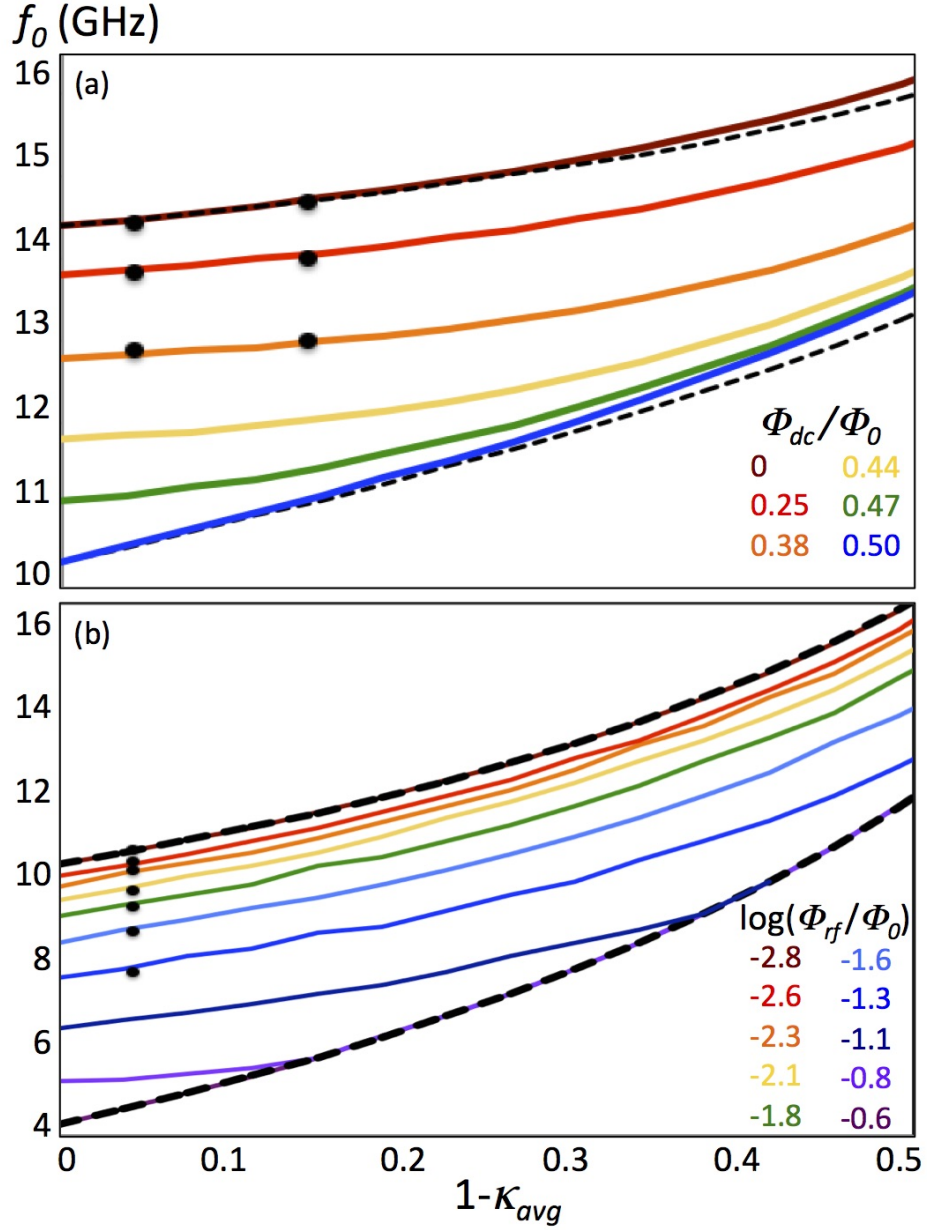


Figure 5.9: Resonant frequency as a function of coupling for 21x21 arrays. The black dots are measured results and the solid lines are numerical results. (a) Various dc flux values in the limit $\Phi_{rf}/\Phi_0 \ll 1$. The dashed lines are solutions to Eq. 5.6 and Eq. 5.7. (b) Various rf flux values and $\Phi_{dc}/\Phi_0 = 0$. The dashed lines are solutions to Eq. 5.6 and Eq. 5.8.

coupling and resonant frequency for various rf flux in Fig. 5.9 (b). Increased coupling decreases the range of rf flux tunability; at zero coupling there is 3 GHz of tuning and at maximum coupling there is only 2 GHz. This is because coupling increases the effective geometric resonant frequency *i.e.* the resonant frequency in the high temperature and rf flux limits.

$$f_{geo,eff} = \frac{f_{geo}}{\sqrt{\kappa_{avg}}} \quad (5.8)$$

The measured effective geometric frequency is 10.5 GHz for the tightly coupled 21x21 array and is < 9.5 GHz (the cutoff of the Ku waveguide) for the the loosely coupled array. (The loosely coupled 21x21 array was also measured in the X band waveguide but the smaller filling fraction made the signal too weak to determine the effective geometric frequency.)

Coupling does not significantly impact the dc flux tunability of the effective permeability, Fig. 5.10. The frequencies shift as described above but the range of tuning (black and grey dashed lines) is unaffected. Coupling complicates the tuning of effective permeability by adding additional minima which arise from the magneto-inductive modes discussed in the following section. The array has a much stronger tuning of effective permeability than an individual rf SQUID because of the larger filling fraction $F = 0.002$; an even larger filling fraction could allow tuning to negative values.

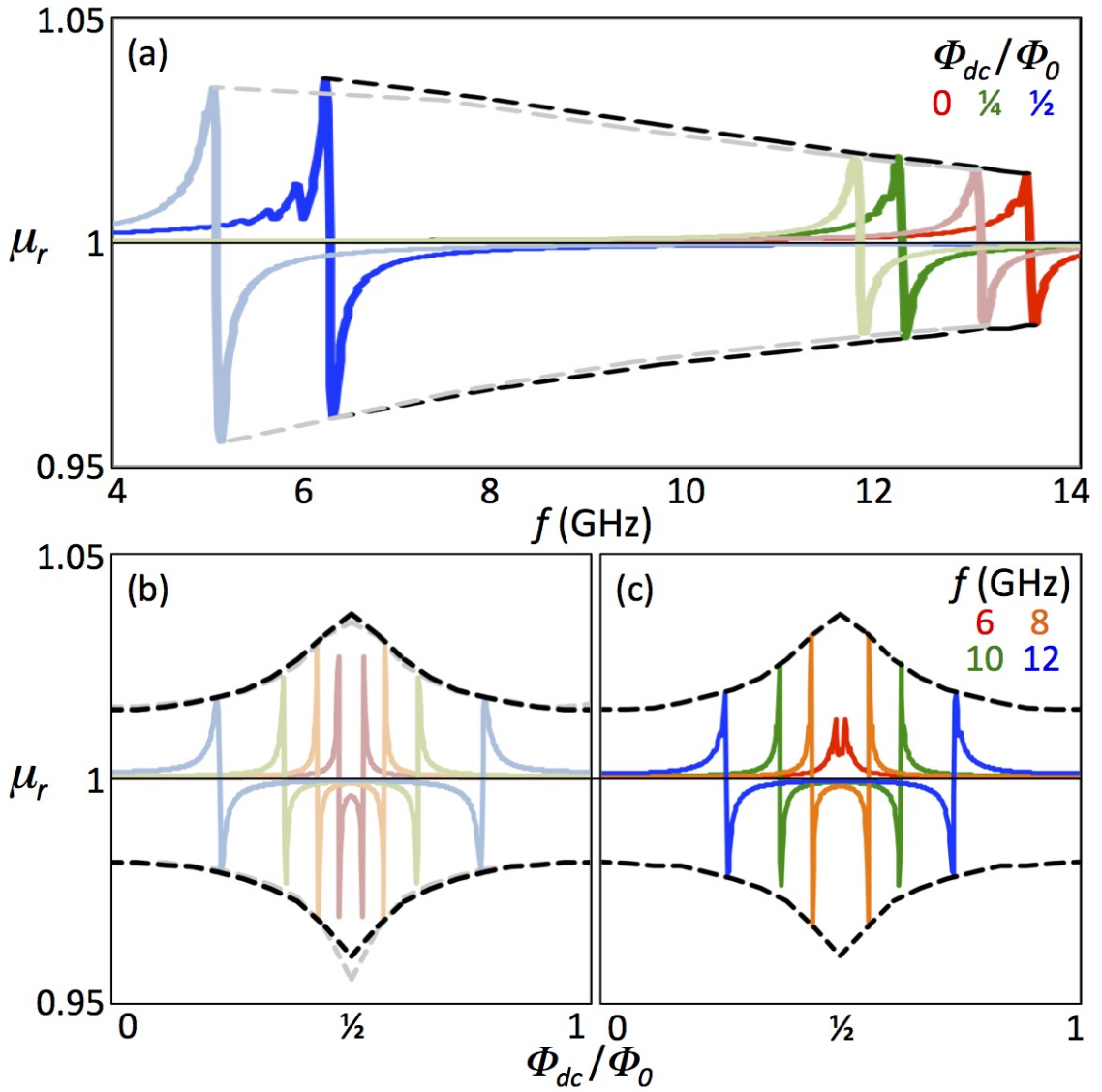


Figure 5.10: (a) Simulated relative effective permeability of 21x21 arrays in the limit $\Phi_{rf}/\Phi_0 \ll 1$ as a function of frequency at fixed dc flux for low coupling $|\kappa_0| = 0.006$ (light colors) and high coupling $|\kappa_0| = 0.02$ (bright colors); (b) as a function of dc flux at fixed frequencies for low coupling (c) and high coupling.

5.2.2 Magneto-Inductive Modes

Unlike the two-SQUID case, multiple distinct resonant modes occur in 2D arrays with uniform applied dc flux; the SQUIDs in an array experience different flux due to coupling (a SQUID on the edge has fewer neighbors to couple flux into its loop than a SQUID in the center). These additional resonances manifest as local minima in $S_{21}(\omega)$, Fig. 5.11 (a). As with the two-SQUID case the highest frequency resonance is coherent $r_A \approx 1$ and has a relatively large magnetic moment so it can be strongly excited by the uniform drive, producing a deep resonance dip. At the edges of the array $\delta(t)$ oscillates with a small amplitude relative to the center as shown in Fig. 5.11 (c). This large variation in amplitude is why the modified Kuramoto order parameter is necessary.

As in the two-SQUID case, the other dips in $S_{21}(\omega)$ represent less coherent resonant modes, closely corresponding to local minima in coherence r_A , Fig. 5.11 (b). These modes have regions where $\delta(t)$ oscillates out of phase by π , Figure 5.11 (d,e). They have a smaller magnetic moment and so interact more weakly with incident microwaves, producing smaller dips in $S_{21}(\omega)$. They occur at lower frequencies because they have a higher effective inductance than the primary resonance.

Lazarides and Tsironis predict the frequencies of MI modes in SQUID arrays in the limit of low dissipation and weak nearest neighbor coupling

$$f_{MI} = f_{geo} \sqrt{\beta_{rf} + \frac{1}{1 + 2\kappa_0 (\cos k_x + \cos k_y)}} \quad (5.9)$$

where k_x and k_y are normalized wavevectors [61]. The solutions to this equation are

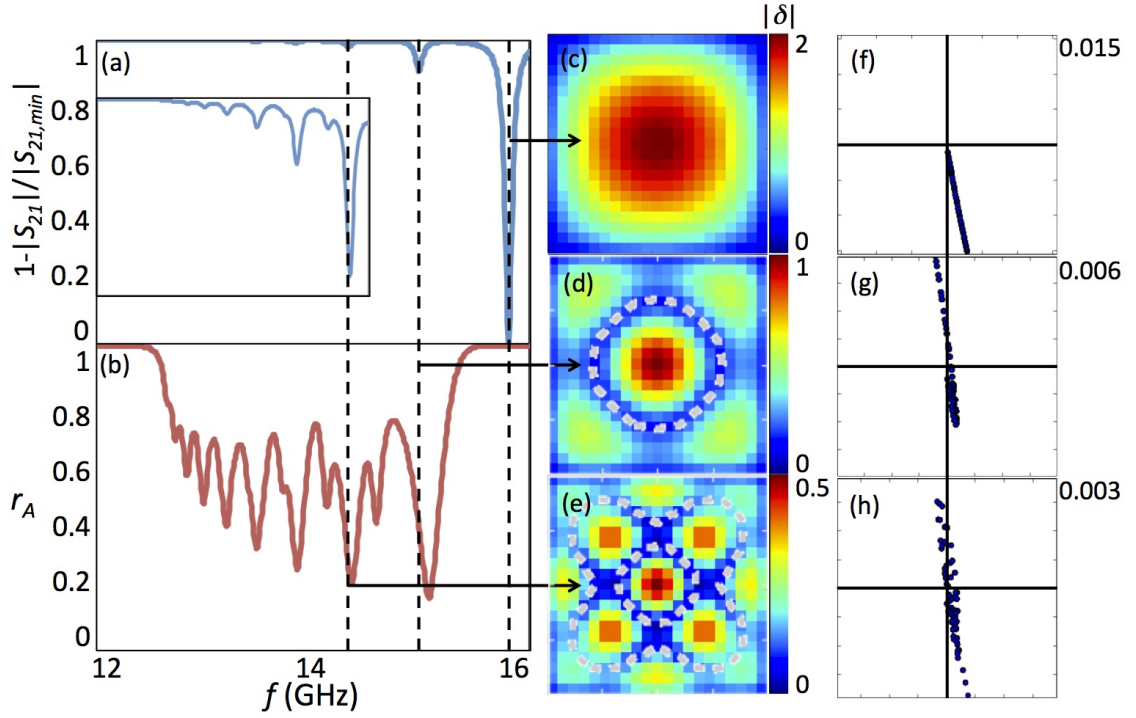


Figure 5.11: (a) Simulated transmission (b) and coherence for 21x21 array with $|\kappa_0| = 0.06$ in the limit $\Phi_{rf}/\Phi_0 \ll 1$. Inset: Enlargement of S_{21} as a function of frequency, showing smaller minima. (c-e) Simulated spatial distribution for the amplitude of $\hat{\delta}$ for the three most prominent modes; dashed white lines show the boundary between regions out of phase by π . (f-h) Scatter plot with the amplitude and phase (relative to the rf drive) of $\hat{\delta}$ in polar coordinates.

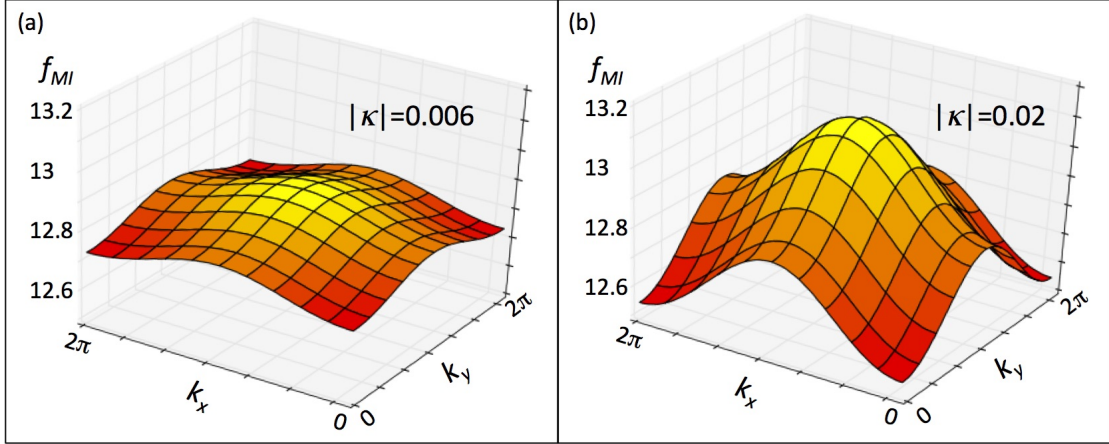


Figure 5.12: (a) Frequency dispersion of magneto-inductive modes, Equation 5.9 for the loosely (b) and tightly coupled 21x21 arrays.

plotted for the 21x21 arrays in Fig. 5.12.

Equation 5.9 cannot be simply extended to take into account the full coupling matrix (for example by replacing κ_0 with κ_{avg}), but it does accurately predict the range of frequencies over which magneto-inductive modes exist assuming only nearest neighbors coupling. The comparison between Eq. 5.9 and simulation results is shown in Fig. 5.13 (a). I used the dissipated power method (Sec. 2.5.1) to calculate transmission S_{21} and coherence r_A in the limit $\Phi_{rf}/\Phi_0 \ll 1$; the highest frequency mode occurs at the minimum in $S_{21}(\omega)$ and the lowest frequency mode occurs when the coherence r_A begins to drop.

When the simulation is repeated using the full coupling matrix (blue line), the modes occur at significantly higher frequencies and over a wider range. Using the

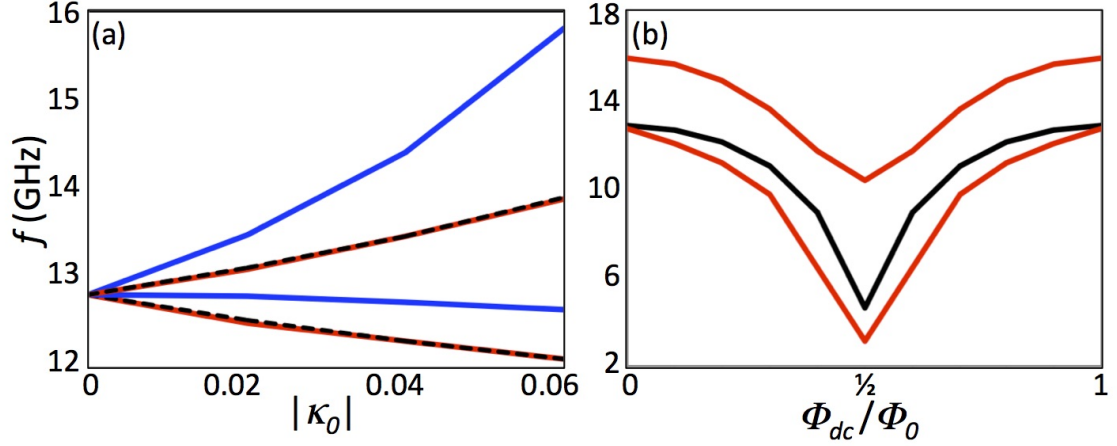


Figure 5.13: (a) The highest and lowest frequency of MI modes in a 21x21 array as a function of coupling for zero dc flux, black: solution to Eq. 5.9, red: simulation results using only nearest neighbor coupling, blue: simulation results using complete coupling matrix. (b) As a function of dc flux using the complete coupling matrix, black: no coupling, red: high coupling with $|\kappa_0| = 0.06$.

full coupling matrix with $\kappa_0 = 0.06$ the linear modes occur over a 3.2 GHz range with the highest frequency mode at 15.8 GHz; when only nearest neighbors are considered there is only a 1.8 GHz range with the highest frequency mode at 13.9 GHz.

Equation 5.9 does not include dc flux dependance of the resonant modes. I illustrate this dependence in simulation for the full coupling matrix in Fig. 5.13 (b). The modes spread such that the range over which MI modes occur is 3 GHz at

$\Phi_{dc}/\Phi_0 = 0$ and the range is 7 GHz at $\Phi_{dc}/\Phi_0 = 1/2$.

I further characterize the resonant modes by considering the eigenvectors of the 2D matrix of the linearized system (Eq. 2.25). These eigenvectors represent solutions for $\hat{\delta}(t)$ for which the response is proportional to the drive. For large coupling $|\kappa_0| = 0.06$, the solutions at the resonant frequencies are composed primarily of a single eigenvector as shown in Fig. 5.14 (b).

On the primary resonance the solution for $\hat{\delta}$ is composed almost entirely of a single eigenvector. For the lower-frequency less-coherent resonant modes the solutions contain a broader mix of eigenvectors, but a single eigenvector still clearly dominates. The third and fifth resonant modes are different from the others in several respects: the dips in $S_{21}(\omega)$ are relatively shallow, the solutions contain a broader mix of eigenvectors, and $\hat{\delta}$ has a larger distribution of phases (the dots in Fig. 5.14 (a) do not all fall as closely along the vertical axis).

When the coupling is lower $|\kappa_0| = 0.02$, the primary resonance is still dominated by a single eigenvector, but this eigenvector continues to be a large component of solutions at the lower resonant frequencies as shown in Fig. 5.15 (b). The lower frequency modes contain a broader mix of eigenvectors and the oscillators have a larger distribution of phases (Fig. 5.15 (a)).

The normal modes of the 2D array can be calculated by a change of variables that separates the second order equations into twice the number of first order

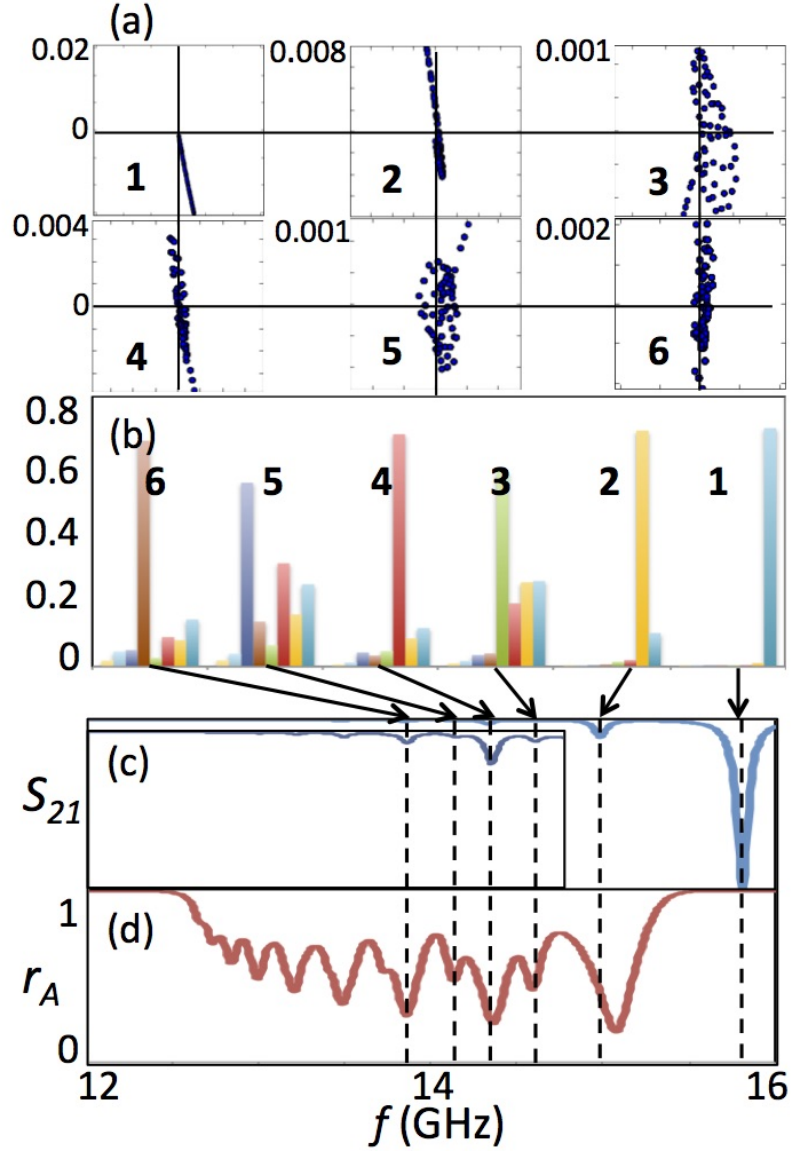


Figure 5.14: Simulation results for the 21x21 array for $|\kappa_0| = 0.06$ at the frequencies of the six highest resonant modes in the limit $\Phi_{rf}/\Phi_0 \ll 1$. (a) Scatter plot for the amplitude and phase of $\hat{\delta}$ in polar coordinates. (b) The dot product of normalized solutions for $\hat{\delta}$ and the first seven eigenvectors of the matrix in Eq. 2.25. (c) Transmission (d) and coherence as a function of frequency.

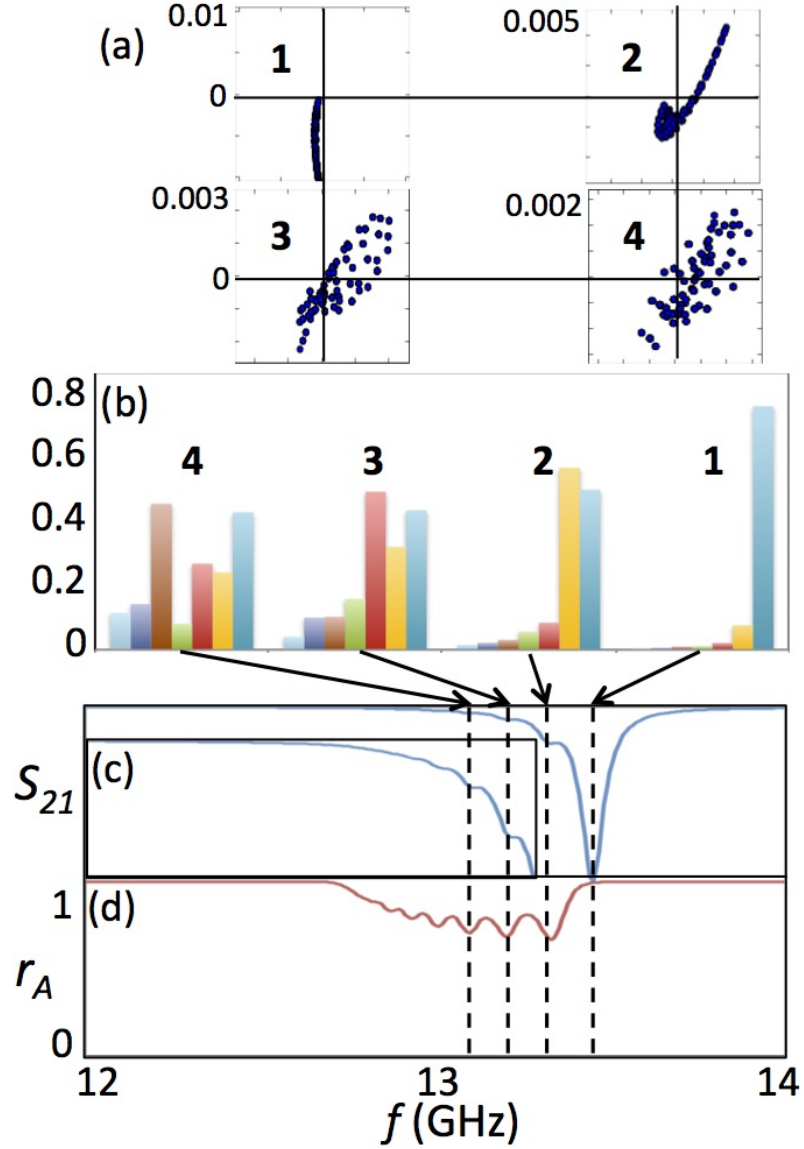


Figure 5.15: Simulation results for the 21x21 array for $|\kappa_0| = 0.02$ at the frequencies of the six highest resonant modes in the limit $\Phi_{rf}/\Phi_0 \ll 1$. (a) Scatter plot for the amplitude and phase of $\hat{\delta}$ in polar coordinates. (b) The dot product of normalized solutions for $\hat{\delta}$ and the first seven eigenvectors of the matrix in Eq. 2.25. (c) Transmission (d) and coherence as a function of frequency.

equations; $\hat{x} = \hat{\delta}$, $\hat{y} = d\hat{\delta}/dt$. With this change of variables Eq. 2.25 becomes

$$\begin{bmatrix} \bar{0} & \bar{I} \\ -(\bar{\kappa}^{-1} + \beta_{rf}\bar{I}) & -\gamma\bar{I} \end{bmatrix} \begin{bmatrix} \hat{x} \\ \hat{y} \end{bmatrix} = \begin{bmatrix} \frac{d\hat{x}}{dt} \\ \frac{d\hat{y}}{dt} \end{bmatrix} \quad (5.10)$$

Assuming periodic solutions of the form $\hat{A}e^{i\omega t}$ the eigenvalues are $i\omega$; the eigenvalues can be used to find the frequencies of the modes.

The eigenvectors of the matrix in Eq. 5.10 are visualized in Fig. 5.16. The red frequencies correspond to the three most prominent $S_{21}(\omega)$ dips in Fig. 5.11 (a) and the corresponding visualization of the eigenvectors resemble Fig. 5.11 (c-e). For these eigenvectors the sum of their elements is greater than zero which means that the modes have a significant magnetic moment and can be excited by the uniform rf flux driving signal.

As in the two-SQUID case, when the rf flux increases at a fixed frequency (within the range of magneto-inductive modes) the primary high-coherence mode eventually dominates regardless of the mode or combination of modes that dominate in the limit $\Phi_{rf}/\Phi_0 \ll 1$. This takeover is demonstrated in Fig. 5.17 by the increase in coherence to $r_A = 1$ with increasing flux as the lower coherence modes are subsumed.

The takeover of the primary resonance can be seen by analyzing the nonlinear solution for $\hat{\delta}$ using the linear eigenvectors of the matrix in Eq. 2.25, Fig. 5.18 (c). When rf flux is increased at the frequency the second mode dominates in the limit $\Phi_{rf}/\Phi_0 \ll 1$, the primary mode becomes more prominent and eventually dominates. Figure 5.18 (b) shows how the center region of the array grows and eventually takes over the whole array. Higher coupling requires higher rf flux for the primary mode

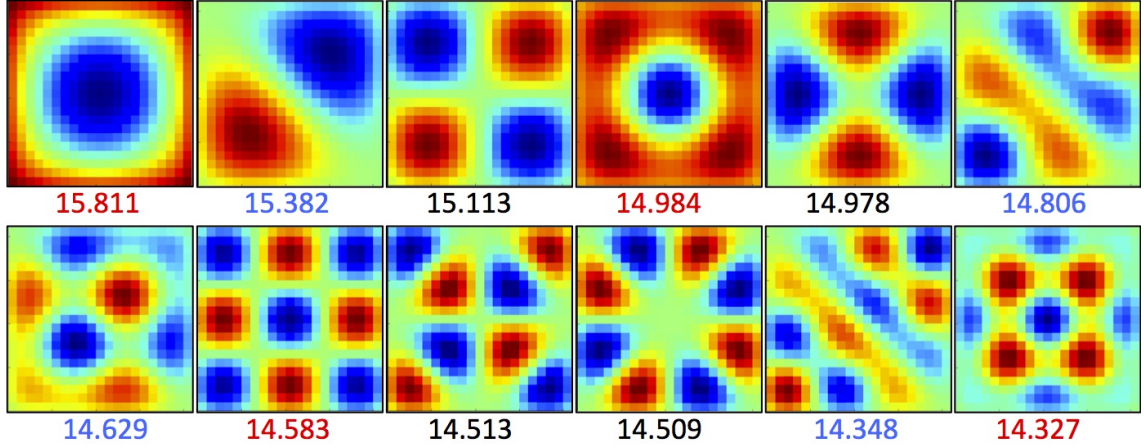


Figure 5.16: Visualization of the eigenvectors of the matrix in Eq. 5.10 for 21x21 array with $|\kappa_0| = 0.06$ corresponding to the highest eigenvalues and their corresponding frequencies in GHz, red and blue represent high magnitude have the opposite sign. Red frequency numbers indicate the mode corresponds to a dip in $S_{21}(\omega)$. Blue frequency numbers indicate the mode is degenerate with another mode rotated by 90° at the same frequency.

to dominate.

In the limit $\Phi_{rf}/\Phi_0 \ll 1$, the frequency range over which MI modes occur is indicated by a suppression of coherence. As the rf flux increases this frequency range is reduced as the upper frequency decreases (the lower frequency remains unchanged), Fig. 5.19 (b). This is more evidence for the takeover of the primary mode; the lower coherence modes do not simply shift to lower frequencies.

When the rf flux is high enough that the resonant frequency is below the

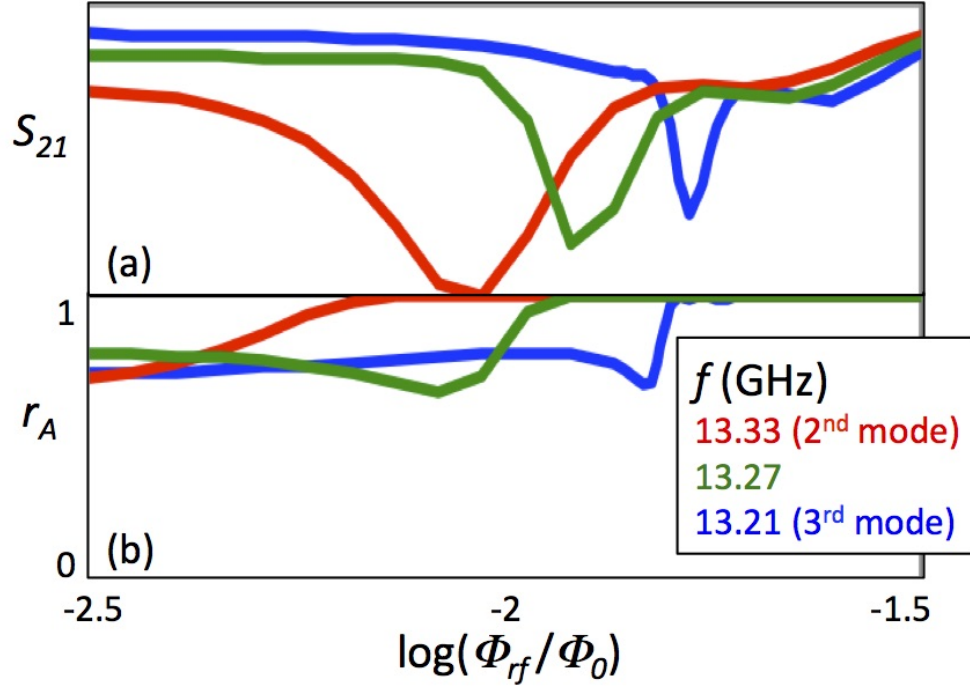


Figure 5.17: (a) Simulated transmission (b) and coherence as a function of rf flux at fixed frequencies the are dominated by low-coherence modes in the limit $\Phi_{rf}/\Phi_0 \ll 1$.

range of MI modes there is a qualitative change in behavior. Coherence is no longer suppressed over an extended range of frequencies, only in a very narrow region just below the resonant frequency, Fig. 5.19 (b). The primary mode no longer dominates on resonance, but the coherence r_A on resonance remains high. At the rf flux value just above the transition, only the corners of the array oscillate on resonance while the rest of the array is still, illustrated in Figure 5.20. As the rf flux increases further these corner regions grow until the whole array oscillates in a manner that resembles the primary mode. This is the opposite of what is seen in linear magneto-inductive

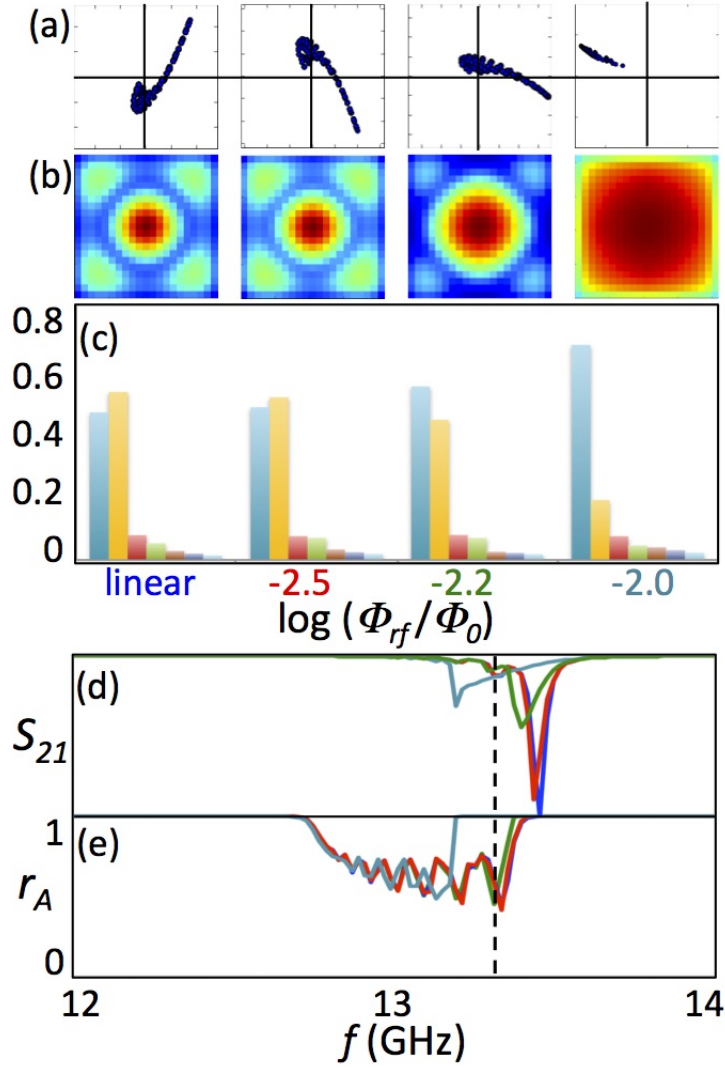


Figure 5.18: Simulation results for the 21x21 array with $|\kappa_0| = 0.02$ at the frequency of the second highest linear mode for various levels of rf flux. (a) Scatter plot for the amplitude and phase of $\hat{\delta}$ in polar coordinates. (b) Spatial distribution of the amplitude. (c) The dot product of normalized solutions for $\hat{\delta}$ and the first seven eigenvectors of the matrix in Eq. 2.25. (d) Transmission (e) and coherence as a function of frequency.

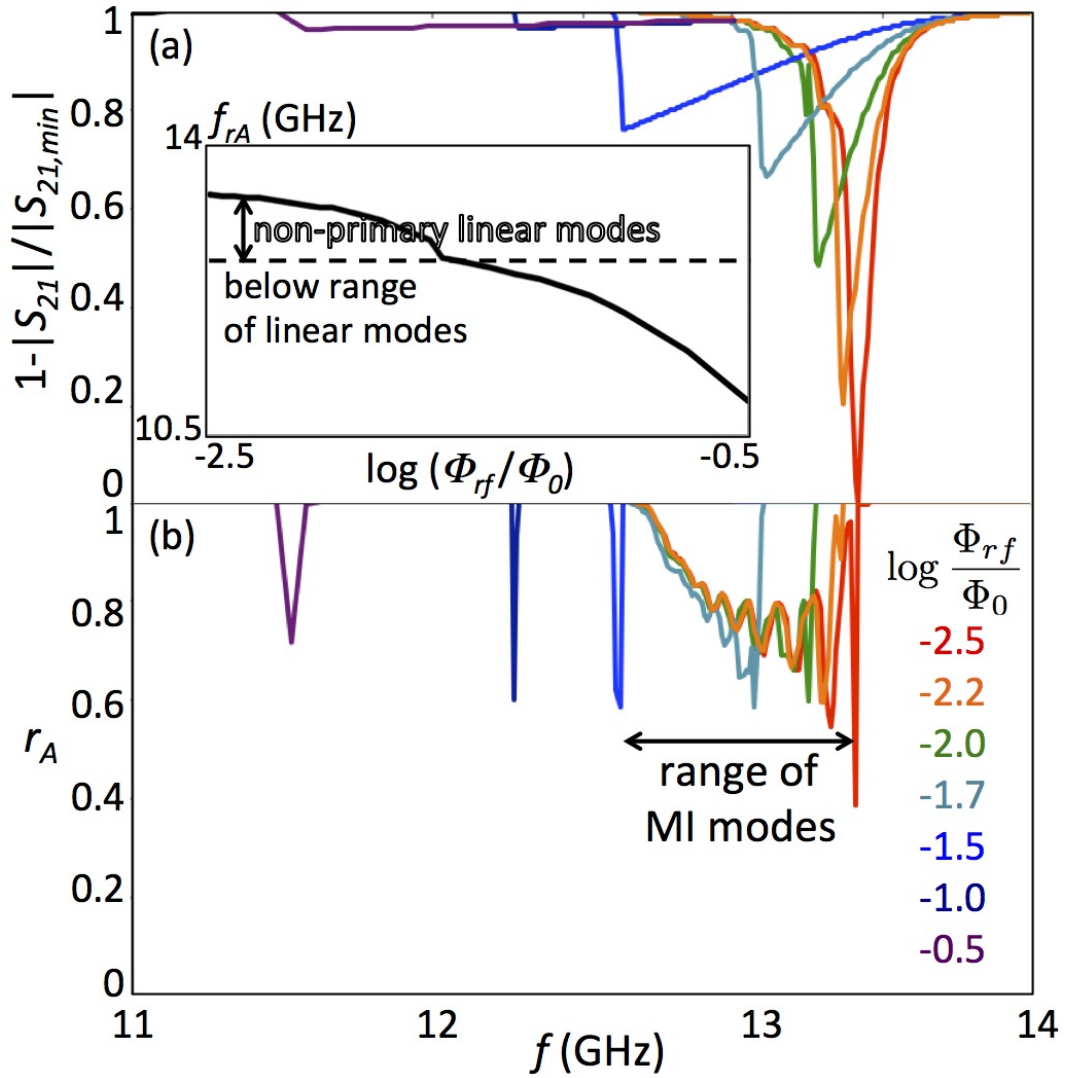


Figure 5.19: (a) Simulated transmission (b) and coherence as a function of frequency for varying amount of rf flux in the 21x21 array with $|\kappa_0| = 0.02$. Solid line in inset shows frequency of the minimum of r_A . Dashed line shows the lower limit of linear MI modes.

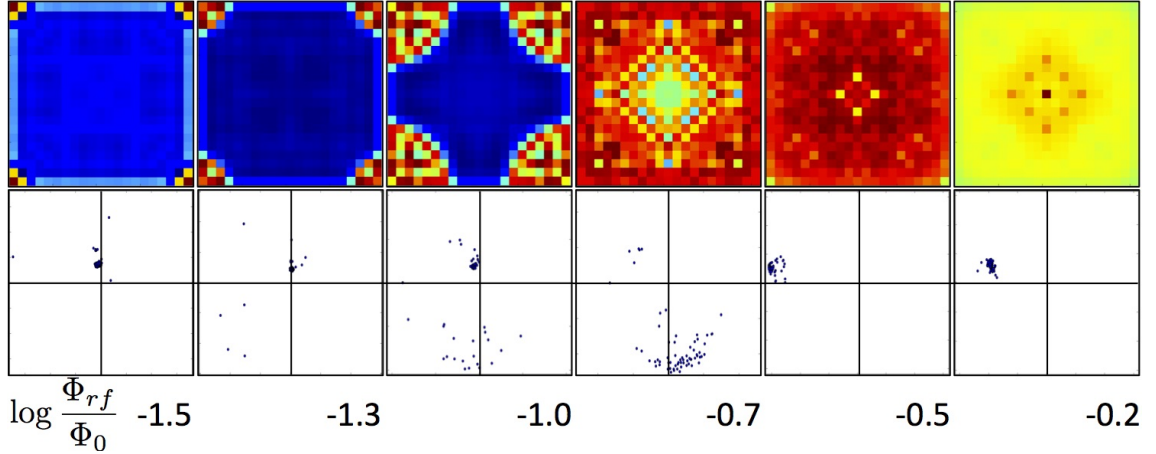


Figure 5.20: Simulation results for the 21x21 array on resonance for various rf flux with $|\kappa_0| = 0.02$. (Top row) spatial distribution of the amplitude of $\hat{\delta}$. (Bottom row) scatter plot for the amplitude and phase (relative to the rf drive) of $\hat{\delta}$ in polar coordinates.

modes (the edges have low amplitude and relative to the center).

5.2.3 dc Flux Disorder

Before considering the effects of dc flux disorder, I will first describe the effect of homogeneous dc flux on coherence. Coupled arrays experience a drop in coherence even when subjected to uniform dc flux as shown in Fig. 5.21 (a). The minimum value of coherence occurs where the Josephson inductance L_{JJ} (Eq. 1.12) diverges (found by substituting $\delta_{dc} = \pi/2$ into 2.10) which for these SQUIDs is at $\Phi_{dc}/\Phi_0 = 0.36$. For this flux value the amplitude of $\delta(t)$ is large at the edges of the array (at $\Phi_{dc}/\Phi_0 = 0$ the amplitude is very small) and out of phase with the center (see

inset of Fig. 5.21 (a)), resulting in a drop in coherence. Although the coherence is lower the transmission dip is deeper, Fig. 5.21 (b); the depth of the dip in $S_{21}(\omega)$ depends on the sum of the amplitudes of $\hat{\delta}$ independent of the phase. The change in coherence and transmission as a function of dc flux is most pronounced when the coupling is high.

The measured results shown in Fig. 5.22 (a) do not show the expected periodicity in dc flux. As dc flux increases the resonance dip becomes wider and shallower, the maximum resonant frequency (when Φ_{dc}/Φ_0 is an integer value) decreases by 0.04 GHz, and there is splitting of the resonance dip as the magneto-inductive modes spread in frequency. (These features are more apparent in measurements of arrays with more egregious disorder, see Sec. B.2.)

These features are reproduced in the simulation and explained by the model when a linear dc flux gradient is applied such that flux at one edge of the array is 90% of that at the other. There is a range of dc flux through the SQUIDs and a corresponding range of resonant response. The resonance dip becomes shallower with increased applied dc flux because fewer SQUIDs participate in the primary resonance and the dip widens because of the broader range of frequency response. The broader range of frequency response also explains the decrease in the maximum frequency (because transmission measures the average response of the SQUIDs and not all of the SQUIDs are at their maximum). This model also predicts an increase in the minimum frequency for the same reason (not visible here because of the waveguide cutoff). The splitting of the modes occurs because the SQUIDs form groups that oscillate at different frequencies. All of these features are a consequence

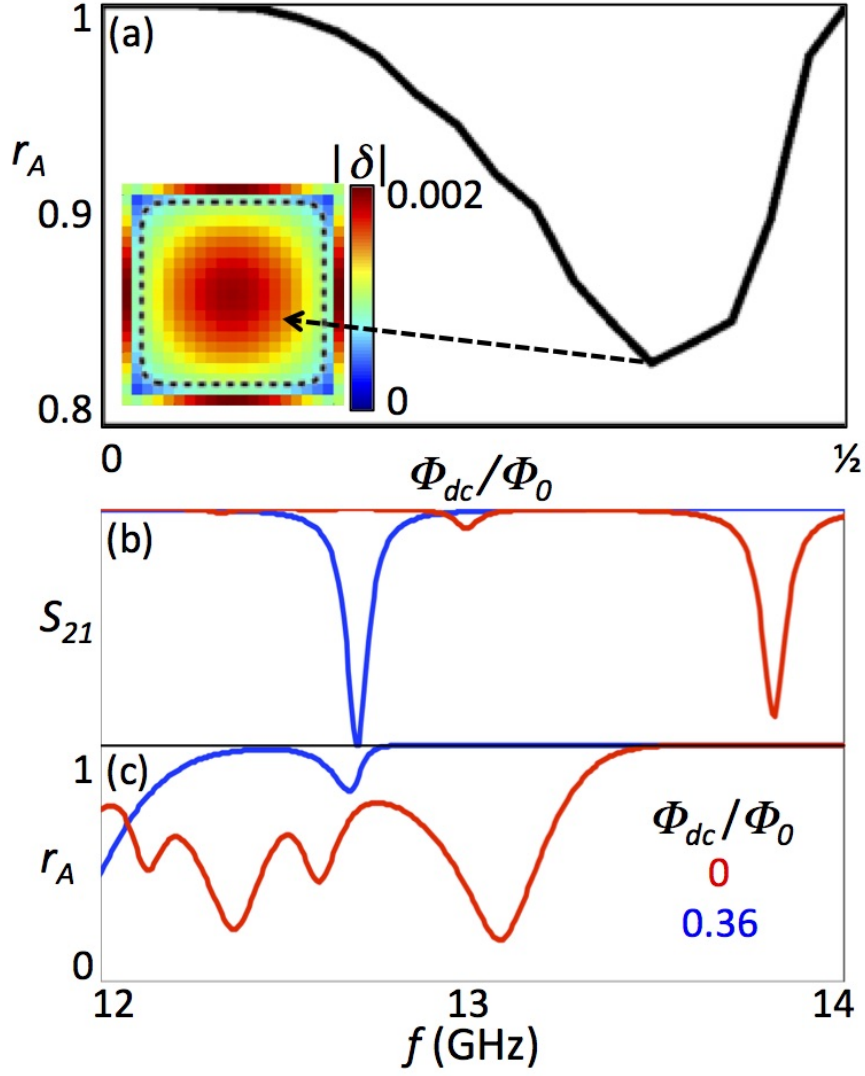


Figure 5.21: (a) Simulated coherence as a function of uniform dc flux in a 21x21 array with $|\kappa_0| = 0.06$ in the limit $\Phi_{rf}/\Phi_0 \ll 1$, Inset: spatial distribution of the amplitude of $\hat{\delta}$ at minimum coherence. Black dashed line indicates boundary of $\pi/2$ phase difference. (b) Simulated transmission (c) and coherence as a function of frequency at maximum and minimum coherence.

of a loss of coherence (different SQUIDs resonate at different frequencies and do not all oscillate in phase with one another), which does not occur in the homogenous flux case (inset curves in Fig. 5.22 (b)). For additional evidence that there is a dc flux gradient in the experiment causing a loss of coherence see Sec. A.

To optimize the performance of the rf SQUIDs as a metamaterial, it is necessary to maximize the coherence r_A . A decrease in coherence (caused by an increase in the dc flux gradient) results in a reduced range of tunability for the effective permeability, Fig. 5.23.

Coherence is also important to the transparency described in Sec. 4.3. Measurements of the single SQUID did not exhibit the hysteretic behavior predicted by the model (Fig. 4.8), but measurements and simulations of the 11x11 array do agree, Fig. 5.24. For increasing rf flux the SQUIDs are in the transparent state and the transparency U increases until the onset of the geometric resonance at high rf flux. For decreasing rf flux the SQUIDs remain in a dissipative state and transparency $U = 0$.

There is no measured hysteresis in the 27x27 array, Fig. 5.25; the SQUIDs are in a dissipative state regardless of the sweep direction and transparency $U = 0$. Lazarides and Tsironis predict that a small amount of disorder in critical currents widens the bistability region (which should make it easier to detect), but further increasing the disorder narrows the region [58]. This might explain why the hysteresis is not evident in the single SQUID and the 27x27 array (which isn't very coherent), but it is in the 11x11 (which has relatively good coherence, see Sec. B.2 for the comparison).

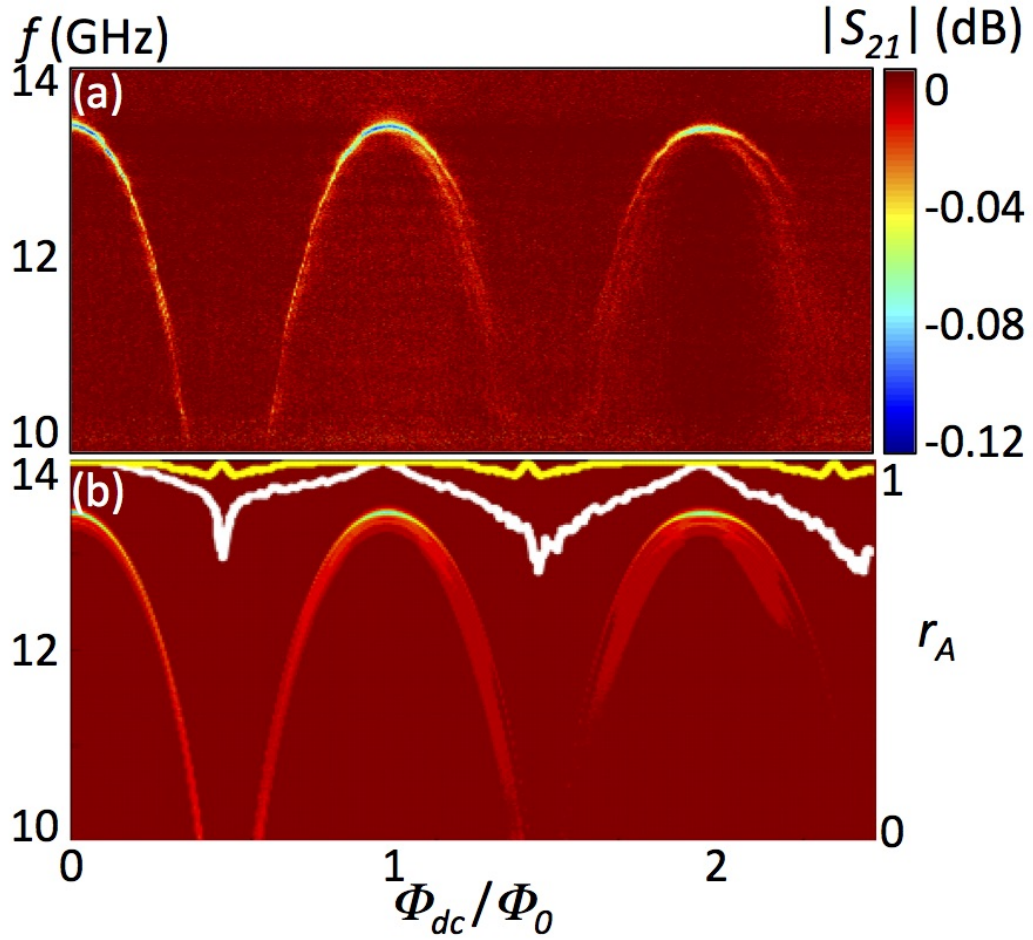


Figure 5.22: (a) Measured (b) and simulated transmission for the 21x21 array with $|\kappa_0| = 0.02$ as a function of frequency and dc flux in the limit $\Phi_{rf}/\Phi_0 \ll 1$. The simulation has a dc flux gradient such that one edge of the array experiences the Φ_{dc}/Φ_0 value shown and the other edge is 90% of that value. Inset curves show simulated coherence r_A as a function of applied dc flux with (white) and without (yellow) the flux gradient.

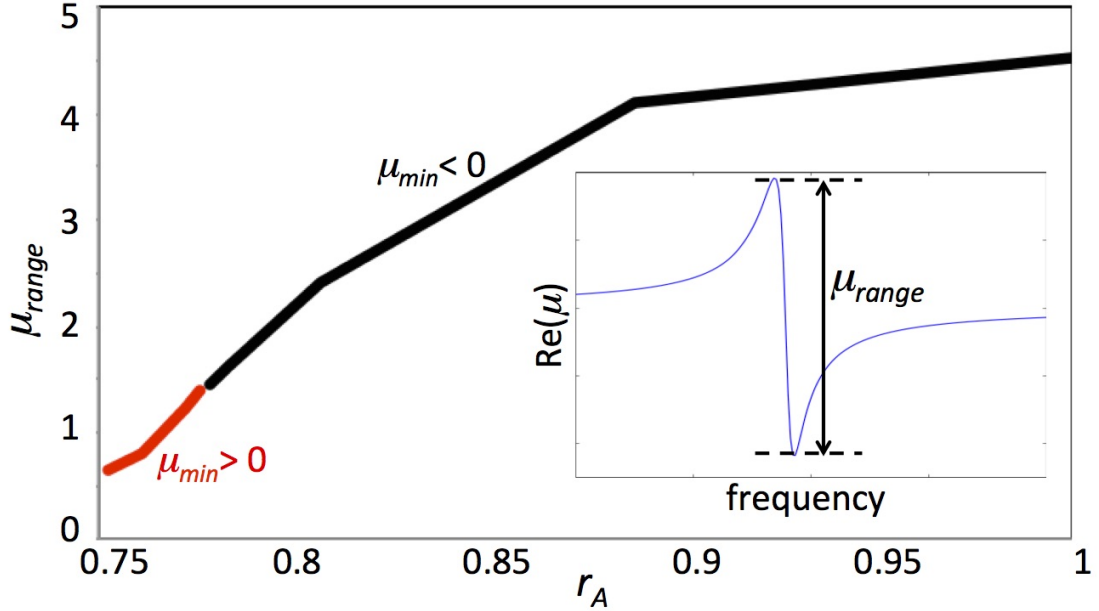


Figure 5.23: Numerical simulation for the range of frequency tunability in the real part of the effective permeability as a function of coherence for eight non-interacting 21x21 arrays with $|\kappa_0| = 0.02$. The coherence was varied by applying a dc flux gradient. The black portion of the curve is where the minimum effective permeability is negative. Inset: simulated real part of effective permeability as a function of frequency illustrating how the range of effective permeability is determined.

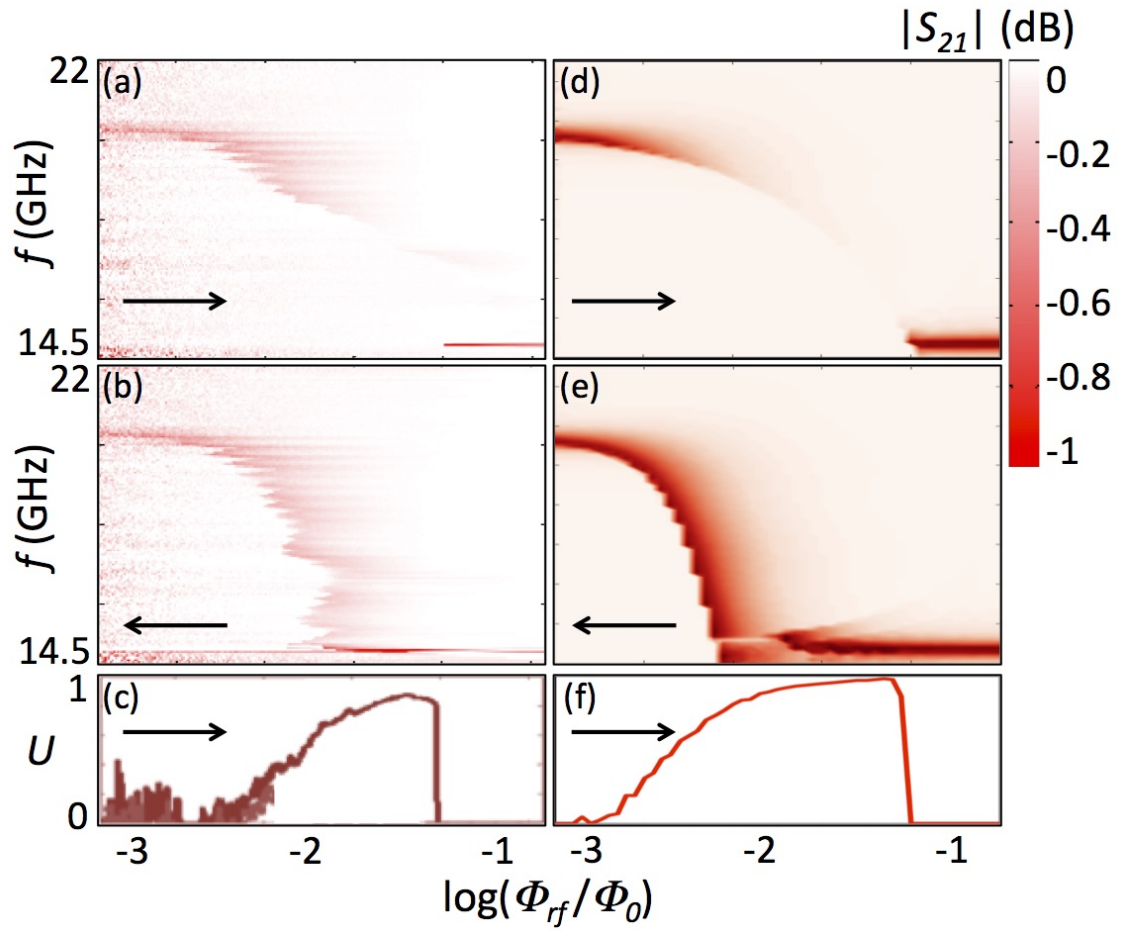


Figure 5.24: (a) Measured transmission in 11x11 array as a function of frequency and for increasing (b) and decreasing rf flux for $\Phi_{dc}/\Phi_0 = 0$ and $T = 4.5$ K. (d) Simulated transmission for increasing (e) and decreasing rf flux. (c) Measured (f) and simulated transparency. Arrows show direction of the Φ_{rf} sweep.

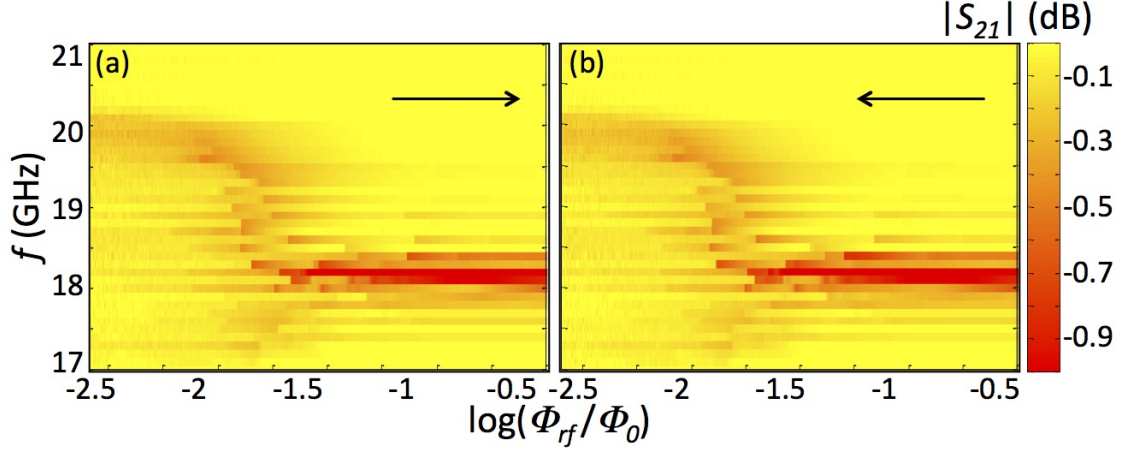


Figure 5.25: (a) Measured transmission in 27x27 as a function of frequency and increasing (b) and decreasing rf flux for $\Phi_{dc}/\Phi_0 = 0$ and $T = 4.5$ K. Arrows show direction of the Φ_{rf} sweep.

According to numerical studies, one way to mitigate the effects of the flux gradient is to increase the coupling between the SQUIDs. When there is no coupling and the dc flux is uniform the oscillators are perfectly coherent $r_A = 1$ with exactly the same amplitude and phase. Increasing coupling causes an initial slight decrease in coherence as shown in the blue curve of Fig. 5.26 (a). This is because the coupling causes the SQUIDs to take on a range of amplitudes and phases consistent with the primary MI mode discussed in Sec. 5.2.2. Further increasing the coupling decreases the phase difference across the array which increases coherence until it saturates at $r_A = 1$.

The tendency for coupling to enhance the coherence persists in the presence

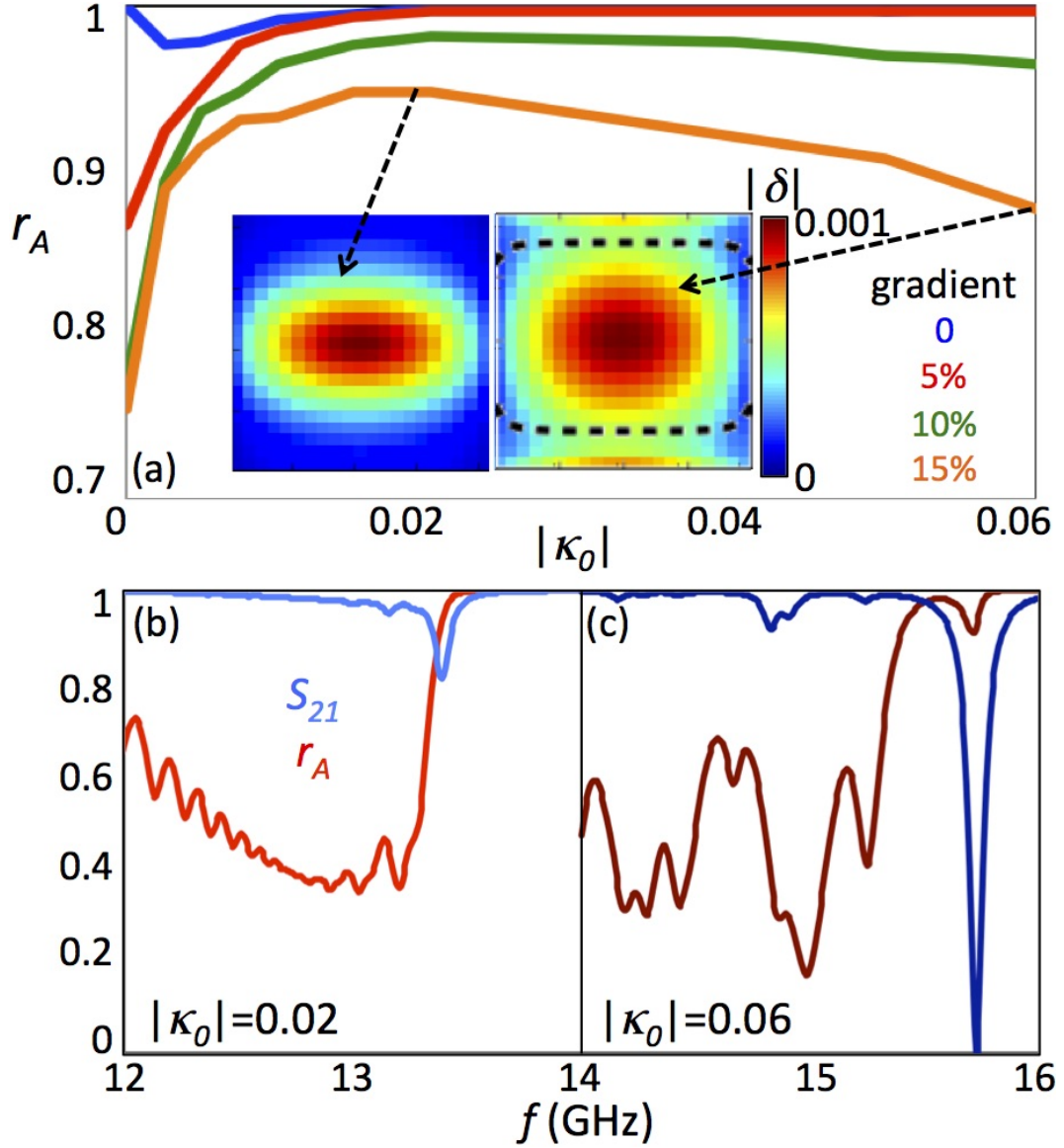


Figure 5.26: Numerically simulated coherence as a function of coupling on the primary resonance at $\Phi_{dc}/\Phi_0 = 2$ for three different flux gradients in the limit $\Phi_{rf}/\Phi_0 \ll 1$. Insets: Simulated spatial distribution of amplitude (color) and phase (contour at $\theta_j = 0$) of $\hat{\delta}(t)$ for a 15% dc flux gradient and two coupling values $|\kappa_0| = 0.02$ and $|\kappa_0| = 0.06$.

of a dc flux gradient. Small amounts of coupling improve coherence regardless of the magnitude of the applied dc flux gradient, (see the low $|\kappa_0|$ part of Fig. 5.26 (a)). However, the coherence as a function of coupling saturates for small flux gradients and actually decreases for larger gradients. This drop occurs because the increased coupling recruits additional SQUIDs to participate in the oscillation, but these SQUIDs are out of phase (an example is shown in the inset of Fig. 5.26 (a)) causing the coherence to decrease. This suggests that there is an optimal value for the coupling; for the 21x21 SQUID arrays this is about $|\kappa_0| = 0.02$.

At higher flux gradients even when the coherence decreases with increasing coupling, the $S_{21}(\omega)$ dip continues to deepen, see Fig. 5.26 (b) and (c). This is because (as discussed above) the depth of the dip in $S_{21}(\omega)$ depends on the sum of the amplitudes of $\hat{\delta}$ independent of the phase.

Another method for mitigating the effects of the dc flux gradient is to decrease the range of dc flux tunability, for example by increasing temperature or rf flux. The decrease in dc flux sensitivity makes the array less sensitive to dc flux disorder, improving coherence. Figure 5.27 shows how the coherence of the array is improved at higher rf flux; the symptoms of the coherence loss with increasing dc flux (*i.e.* the $S_{21}(\omega)$ dip becomes broader, shallower, and splits and the maximum frequency decreases while the minimum frequency increases) are not as pronounced for higher rf flux values.

Of these symptoms the depth of the transmission dip is the easiest to quantify. If the array were coherent there would be no change in the depth of the $S_{21}(\Phi_{dc})$ dip with increased dc flux. However, for low rf flux the dips become substantially

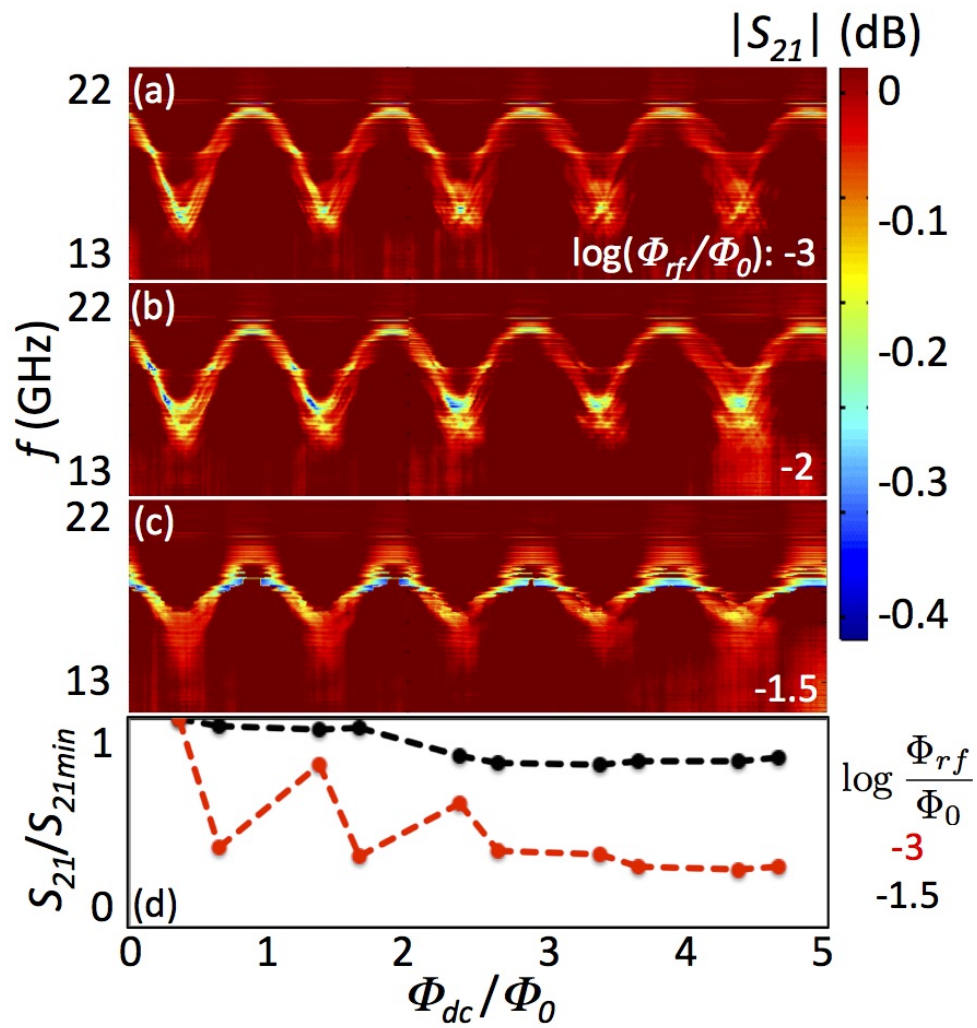


Figure 5.27: (a-c) Measured transmission as a function of frequency and dc flux at three values of rf flux for 27x27 array $T = 7$ K. (d) Local minima in measured transmission as a function of dc flux for two rf flux values.

shallower with increased dc flux indicating a loss of coherence, Fig. 5.27 (d). At the higher rf flux the transmission dips and coherence are not as strongly affected.

Increased temperature also decreases the dc flux sensitivity and improves coherence. Figure 5.28 shows how the coherence is improved for higher temperatures just as it is for higher rf flux. The tradeoff between dc flux tuning and coherence can be adjusted after fabrication with temperature and rf flux, unlike the coupling between SQUIDs which is determined by the array geometry.

5.3 Summary

I have found that relative to a single SQUID, 2D SQUID arrays experience comparable tuning with dc flux, temperature, and rf flux; but the response in arrays is larger because of the increased filling fraction. SQUID arrays differ from individual SQUIDs in the following respects: coupling between the SQUIDs, additional resonant modes, and the possibility of dc flux disorder.

Coupling causes the resonant frequency to deepen and shift to higher frequencies, but does not have a significant effect on the range of dc flux tuning of effective permeability. However, it complicates the tuning of effective permeability by introducing minima due to magneto-inductive modes.

The additional resonant modes occur at lower frequencies (relative to the primary mode), are associated with smaller $S_{21}(\omega)$ dips, and have lower coherence than the primary mode. As rf flux increases the primary high-coherence mode dominates regardless of the mode or combination of modes at that frequency in the limit

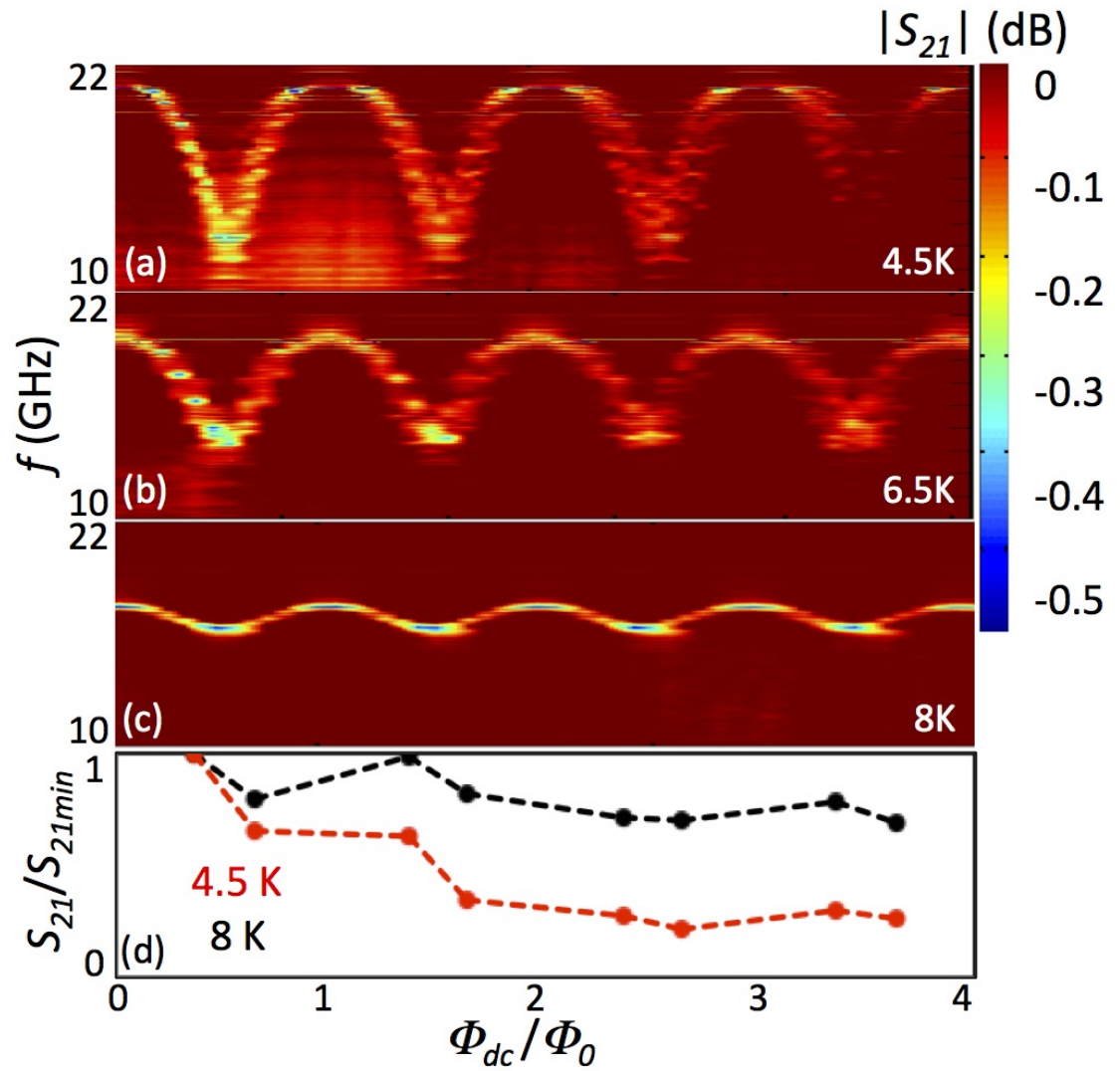


Figure 5.28: (a-c) Measured transmission as a function of frequency and dc flux at three temperatures for 27x27 array $\log \Phi_{rf}/\Phi_0 = -2$. (d) Local minima in measured transmission as a function of dc flux for two temperature values.

$$\Phi_{rf}/\Phi_0 \ll 1.$$

There is a linear dc flux gradient present in the experiment which results in a loss of periodicity in dc flux, a reduction in maximum resonant frequency, a broader and shallower resonant dip, and splitting of the resonance dip at higher dc flux values. These are all symptoms of a loss of coherence. The coherence must be high for the array to have a tunable effective permeability and to exhibit transparent behavior at intermediate rf flux. The coherence can be recovered by increasing coupling, rf flux or temperature.

By using these strategies to maximize coherence and taking steps to minimize uneven dc flux bias, arrays of rf SQUIDs can be tuned coherently. The large-magnitude, high-speed, low-loss tuning behavior that is observed in the single SQUID is also possible in a 2D SQUID metamaterial.

Chapter 6: JJ-Loaded Wire Array Measurements

In this chapter, I show how the transmission and permittivity of a Josephson junction loaded wire array tune in the low rf and dc current limits. I also briefly explore the complicated hysteretic and nonlinear behavior beyond these limits.

6.1 Low dc and rf Current

The JJ-loaded wire arrays are designed to operate in the low dc current and low rf input power regime. The cutoff frequency of the wire array is tunable with temperature and dc bias current, allowing tuning of the effective permittivity and causing a measurable change in transmission.

The measured current dependence of transmission through a waveguide with a single layer of eight wires (Fig. 3.10 (a)) for various frequencies is shown in Fig. 6.1 (a,b). There is a relatively flat region around zero current, but when the dc current approaches the critical current there is a precipitous drop in transmission as δ starts to develop phase slips and the junctions switch into a more dissipative state. The system is hysteretic; the state (dissipative or non-dissipative) the system is in depends on the direction of the current sweep.

The model described in Sec. 2.1 is valid only in the relatively flat region

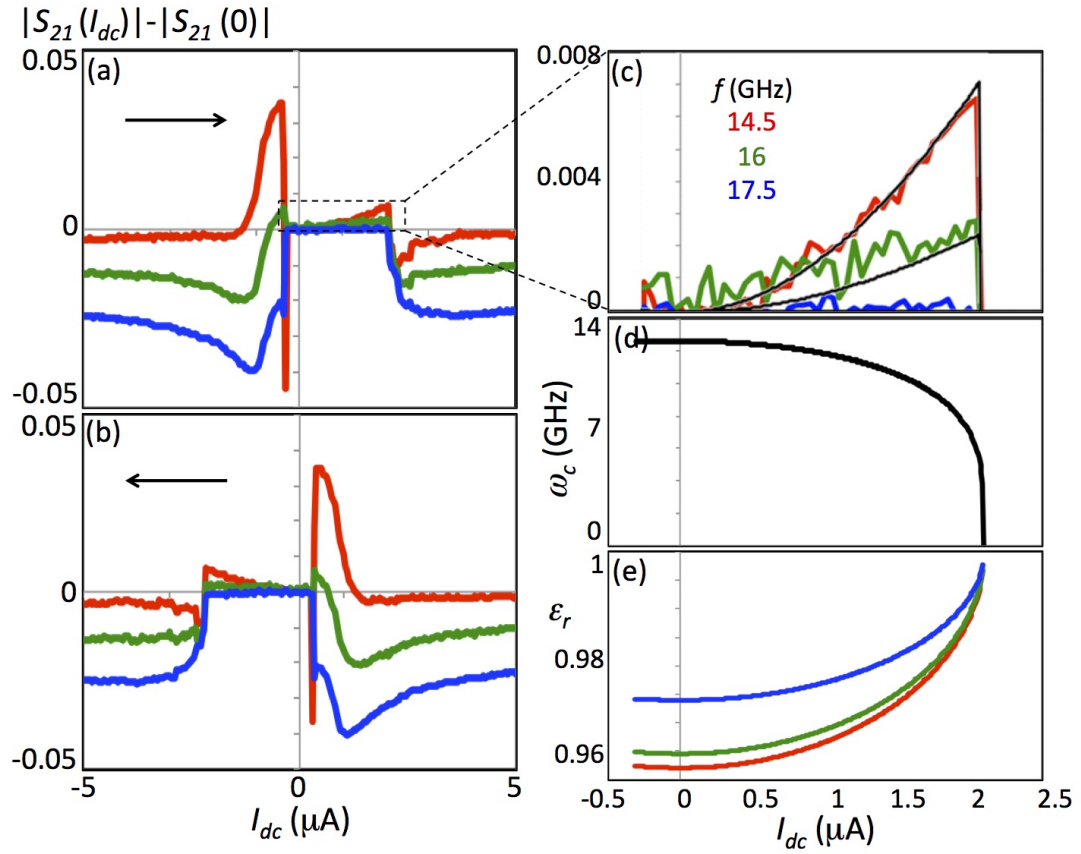


Figure 6.1: (a) Measured transmission (normalized by $S_{21}(I_{dc} = 0)$) as a function of increasing (b) and decreasing dc current for three frequencies (all above the cutoff frequency of the wire array in the waveguide) in the limit $I_{rf} \ll I_c$. (c) Enlargement of the low dc current region. Black lines are calculated from the model. (d) Simulated cutoff frequency (e) and effective relative permittivity as a function of dc current.

at low dc current. The model predicts that the cutoff frequency shifts to a lower frequency as the dc current increases, Fig. 6.1 (d), and this shift causes the increase in transmission at fixed frequency seen in Fig. 6.1 (a). The change in transmission is smaller at higher frequencies, further from the cutoff frequency. The measured transmission shows good agreement with the model's predictions. (For details on how model parameters were chosen to match the data see Sec. C.2.)

The shifting cutoff frequency means the effective permittivity can be tuned with dc current, as shown in Fig. 6.2 (e). The effect is small because there is only one layer of wires with a filling fraction $F = 0.05$. Increasing the filling fraction would increase the tuning.

Figure 6.2 (a,b) shows that the transmission drops (and the junctions transition to the more dissipative state) at lower currents for higher temperatures *i.e.* increasing the temperature lowers the critical current of the junctions, Tab. 6.1. The retrapping current I_r , the current at which the junctions switch from the dissipative to the non-dissipative state, increases with temperature. The low dc current region (where the model is valid) is narrower and less hysteretic.

Table 6.1: Transition currents.

$T(\text{K})$	$I_c (\mu\text{A})$	$I_r (\mu\text{A})$	width of hysteresis loop (μA)
4.5	2.1	0.3	1.8
6	1.85	0.5	1.35
8	1.25	0.7	0.55

The model predicts that increasing the temperature decreases the cutoff fre-

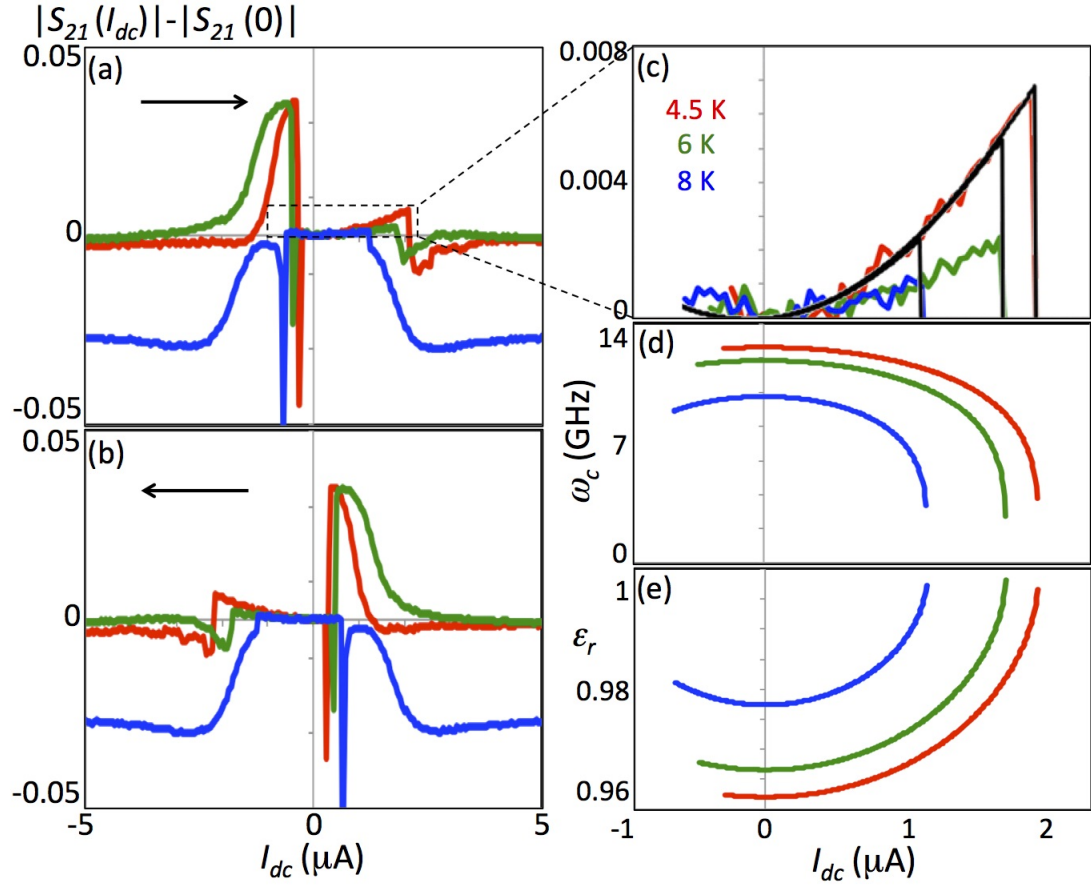


Figure 6.2: (a) Measured transmission (normalized by $S_{21}(I_{dc} = 0)$) as a function of increasing (b) and decreasing dc current for three temperatures at 14.5 GHz in the limit $I_{rf} \ll I_c$. (c) Enlargement of the low dc current region. Black lines are calculated from the model. (d) Simulated cutoff frequency and (e) effective relative permittivity as a function of dc current.

quency (Fig. 6.2 (d)) increasing the transmission, which agrees with the data, Fig. 6.2 (c). Changing temperature is another way to tune the effective permittivity, Fig. 6.2 (e).

6.2 Beyond the Small Current Limits

The change in critical current with temperature can also be measured in the dc voltage drop on the parallel array of eight wires, Fig. 6.3 (a); the critical current is the current at which voltage is no longer zero. The inset shows that the dc voltage increases in discrete steps with increasing dc current. The height of these steps is equal to the gap voltage V_g and each step represents a single junction switching into the dissipative state. The saturation voltage at high current ($10 \mu\text{A}$) is 100 (the number of junctions per wire) times the size of these steps, indicating that all the junctions have switched into the dissipative state. The gap voltage decreases with increasing temperature: 0.274 mV at 4.5 K, 0.268 mV at 6 K, and 0.247 mV at 8 K. The wide range of currents over which these steps occur indicates a large spread of critical currents in the junctions.

When there are no microwaves present there are smaller steps superimposed on these with a height of $20 \mu\text{V}$ and even smaller steps with a height that trends up with increasing dc current as shown in Fig. 6.4. When there are microwaves present there are steps with a height that also trends up with increased dc current. Increasing the frequency decreases the size of the steps; this is the opposite of what is expected for Shapiro steps.

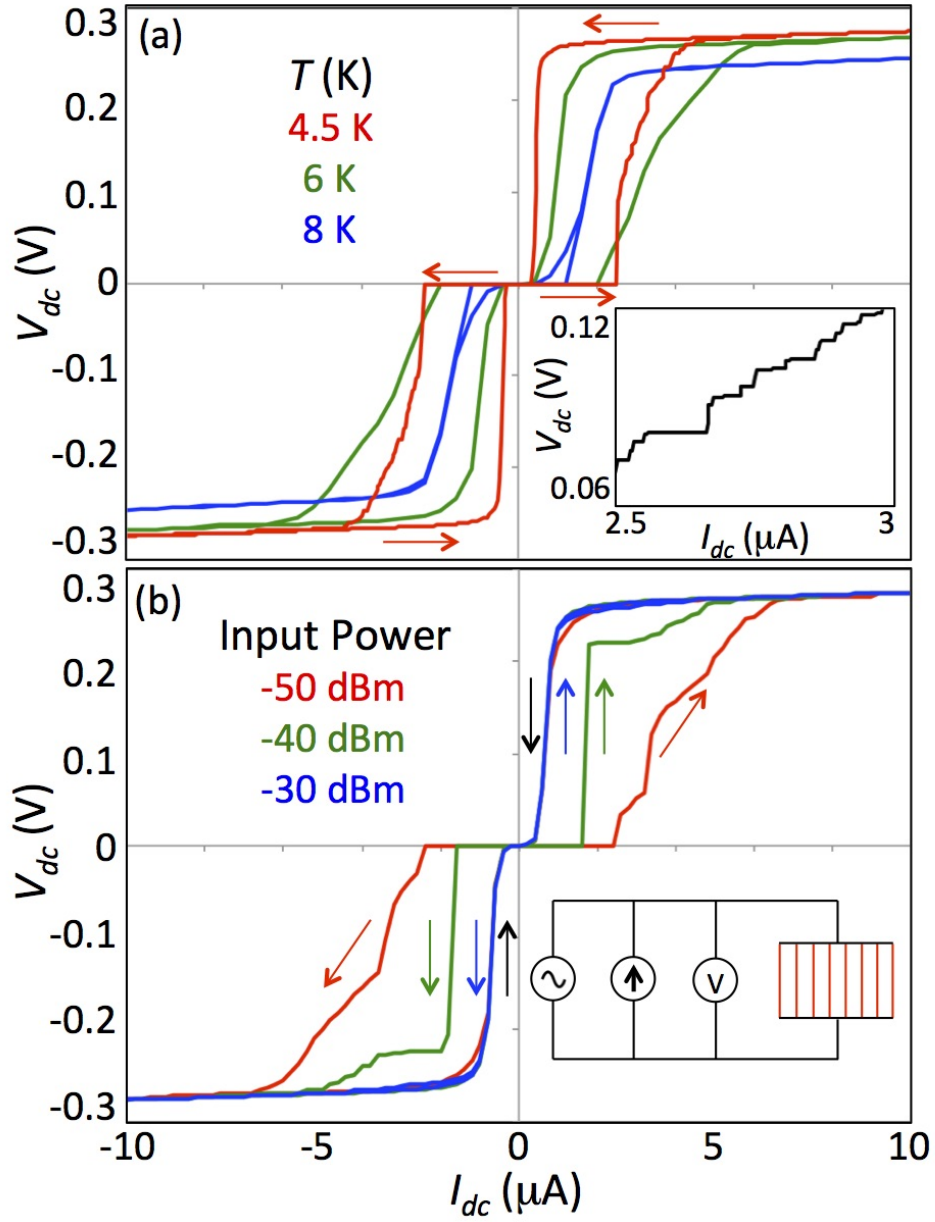


Figure 6.3: (a) Measured dc voltage drop on the wire array as a function of dc current at three temperatures in the limit $I_{rf} \ll I_c$. Inset: Enlargement showing voltage steps. (b) Measured dc voltage as a function of dc current at 20 GHz and three input powers. Inset: circuit diagram with superconducting portions marked in red.

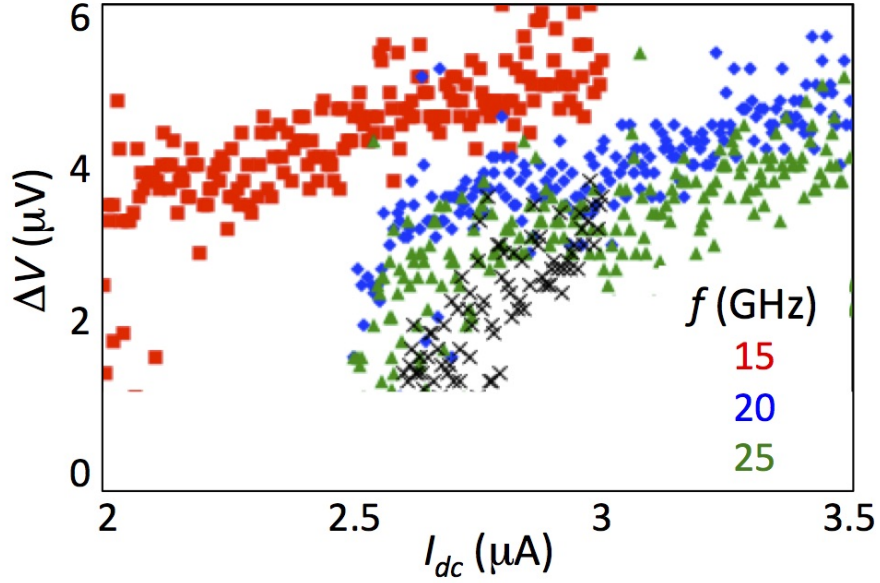


Figure 6.4: Size of the small voltage steps as a function of dc current. black: no microwave power. red: 15 GHz, blue: 20 GHz, green: 25 GHz for -50 dBm microwave input power.

Figure 6.3 (b) shows how the dc voltage as a function of dc current changes with the application of microwave power. The retrapping current is unaffected by microwave power. The critical current decreases with increasing microwave power, narrowing the hysteresis loop until it disappears at high power. The largest steps (with a height of V_g , shown in the inset of Fig. 6.3 (a)) are unaffected by the application of microwave power; the saturation voltage at high dc current is likewise unaffected.

Figure 6.5 shows how the transmission as a function of rf input power and dc current changes for different sweep directions. The sharp vertical lines indicate the

transitions between the dissipative and non-dissipative states, *i.e.* the critical and retrapping currents. The insensitivity of the retrapping current to microwave power shown in Fig. 6.3 (b) can also be seen in Fig. 6.5. However, Figure 6.3 (b) suggests that increasing rf input power decreases the critical current, where Fig. 6.5 shows that the dependence of critical current on microwave power is more complicated and highly hysteretic.

For certain sweep directions (Fig. 6.5 (c)) the critical current does decrease with increasing input power, but for other sweep directions (Fig. 6.5 (a) and (b)) the critical current is insensitive to rf input power. The dc current hysteresis also varies with sweep direction; it is most pronounced in Fig. 6.5 (c), but Fig. 6.5 (a) shows very little. All of the sweeps show that transmission has a complicated non-monotonic dependence on rf input power.

To characterize the nonlinearity I measured intermodulation power by stimulating the sample at two frequencies (as opposed to a single frequency) 10 MHz apart. The frequency spectrum is shown in Fig. 6.6 (a). The central peaks are at the main tone powers; the other peaks occur because the nonlinearity of the material converts some of the power at the main tones to other frequencies. The third order intermods are at 14.985 GHz and 15.015 GHz ($2f_1 - f_2$ and $2f_2 - f_1$). At higher input power the third order intermods (as well as the higher order intermods) are higher relative to the main tone power indicating more nonlinearity in the sample.

Third order intermod power (normalized by the main tone power) as a function of frequency and dc current is shown in Fig. 6.6 (b,c). Like transmission the intermod power has a complicated non-monotonic dependence on input power. The

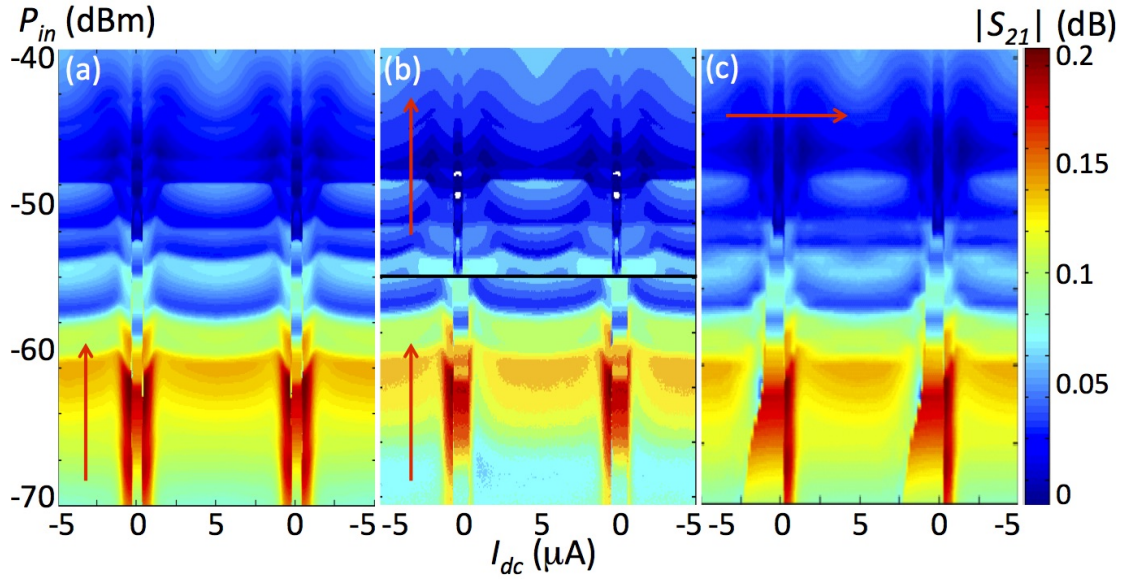


Figure 6.5: Measured transmission as a function of rf input power and dc current (increasing and decreasing) at 15 GHz for different sweep directions. (a) Sweep entire input power range and step current. (b) Sweep half input power range and step current (below the black line), then sweep other power range while stepping current (above the black line). (c) Sweep dc current and step power.

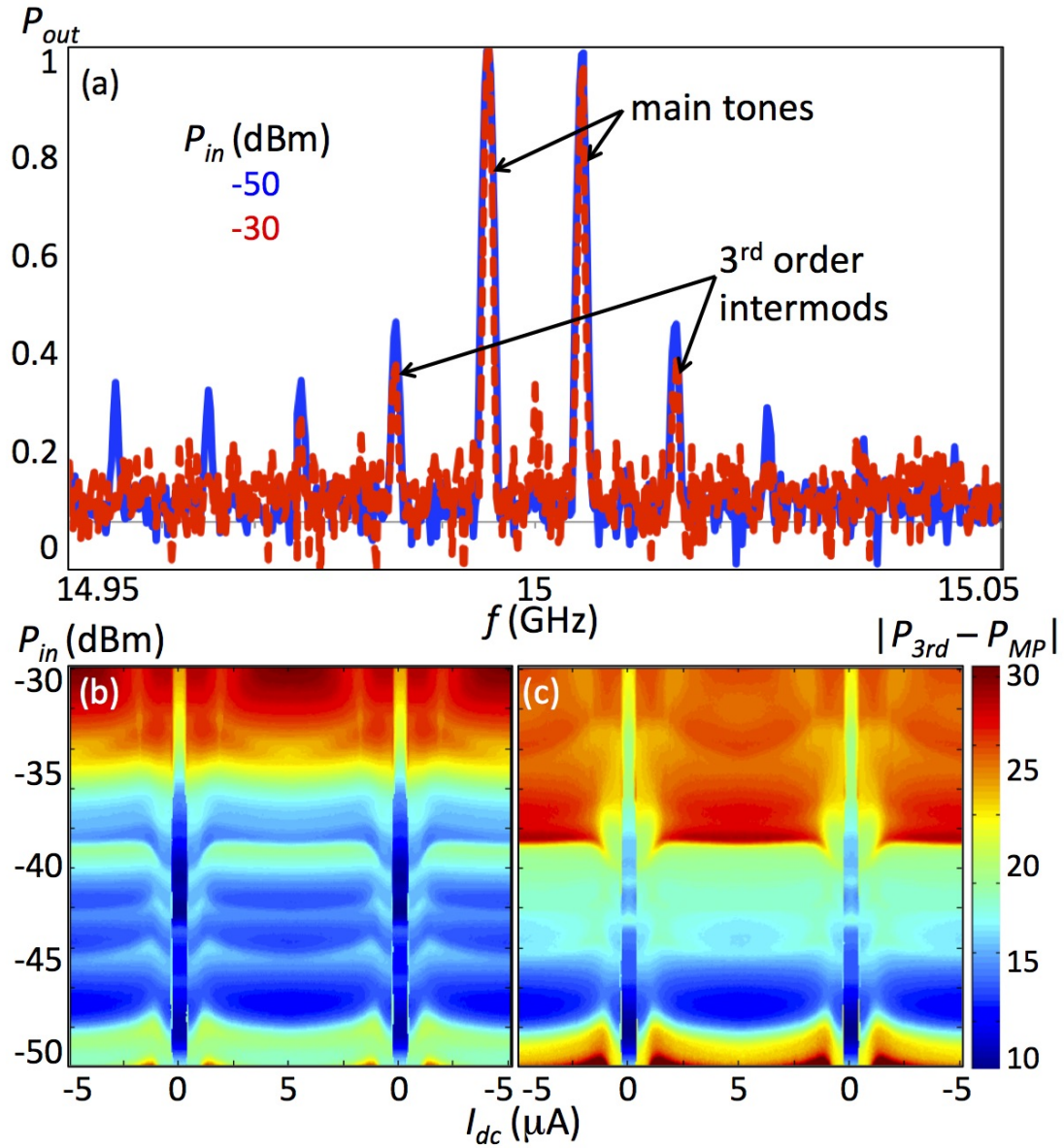


Figure 6.6: (a) Measured output power (normalized to fall between zero and one) as a function of frequency. blue: -50 dBm input power. red: -30 dBm input power. (b) Measured third order intermod power (normalized by main tone power) as a function of input power and both increasing and decreasing dc current with center frequency 15 GHz at lower (c) and higher intermod frequency.

nonlinearity tends to be higher for greater input power and when the junctions are in the dissipative state. These are the regions that the model fails.

6.3 Summary

The JJ-loaded array behaves as expected in the low dc current and low input power regime it was designed to operate in. The measured tuning of transmission indicates the tuning of cutoff frequency and permittivity predicted by the model. I have also observed interesting behavior at higher current and rf input power. The dynamics are very rich, highly hysteretic, and nonlinear.

Chapter 7: Conclusions

In this chapter, I summarize the results of measurements and simulations on a Josephson junction loaded wire array and rf-SQUID metamaterials. I discuss possible applications of these tunable superconducting metamaterials, and suggest directions for future work.

7.1 rf SQUID Metamaterials

I found that individual rf SQUIDs exhibit the overall behavior that I expect. The resonance and effective permeability of an individual rf SQUID tune over a wide range with dc flux, temperature, and rf flux. The dc flux tuning can be achieved at high speeds. 2D SQUID arrays experience comparable tuning with each parameter and the effect is much larger because of the increased filling fraction. An even larger filling fraction should allow negative values of effective permeability. In the future, it will be interesting to examine full 3D SQUID structures and nonplanar coupling between SQUIDs (which can be positive unlike planar coupling which is always negative).

SQUID arrays differ from individual SQUIDs in the following respects: coupling between the SQUIDs, additional resonant modes, and dc flux disorder. Cou-

pling causes the transmission minima to deepen and the resonant frequency to shift to higher frequencies, but does not have a significant effect on the range of dc flux tuning of effective permeability. However, it complicates the tuning of effective permeability by introducing minima due to magneto-inductive modes.

The additional resonant modes occur at lower frequencies (relative to the primary mode), are associated with smaller $S_{21}(\omega)$ dips, and have lower coherence than the primary mode. As rf flux increases the primary high coherence mode dominates regardless of the mode or combination of modes at that frequency in the low rf flux limit. So far the only experimental evidence for these modes is dips in the $S_{21}(\omega)$ which is a measure of their collective response. It would be interesting to measure each SQUID in the array individually with a laser scanning microscope to recreate the simulated results for the spatial distribution of amplitude and phase of δ .

There is a linear dc flux gradient present in the experiment which results in a loss of periodicity in dc flux, a reduction in maximum resonant frequency, a broader and shallower resonant dip, and splitting of the resonance dip at higher dc flux values. These are all symptoms of a loss of coherence. The coherence must be high for the array to work as designed with a tunable effective permeability. The coherence can be recovered by increasing coupling, rf flux, or temperature.

By using these strategies to maximize coherence and taking steps to minimize uneven dc flux bias (*e.g.* by using a coil with a larger radius to apply dc flux bias), arrays of rf SQUIDs can be tuned coherently. The large-magnitude, high-speed, low-loss tuning behavior that is observed in the single SQUID is also possible in a 2D SQUID metamaterial.

The ability to tune the electromagnetic response over a wide range, and on short time scales, is desirable for applications such as software-defined radio [110] and filters for digital rf receivers [111,112]. It is expected that SQUID metamaterials will be able to perform functions similar to galvanically connected SQUID arrays. One possible application takes advantage of the SQUID's extreme sensitivity to magnetic flux to create compact, wideband antennas, sensitive to high frequency magnetic fields [113–116]. Other possible applications include low noise amplifiers for rf sensing and qubit readout [117–119], and highly sensitive magnetometers and filters [120–122].

In addition to the tunable effective permeability I set out to achieve, the individual rf SQUID meta-atom also exhibited a novel transparency feature. Whether this feature also occurs in SQUID array metamaterials could depend on the array coherence. SQUIDs are potentially useful as a power limiter for sensitive front-end receivers [105]. For further details about the mechanism behind transparency see the following references: [53, 58, 95].

7.2 JJ-loaded Wire Array Metamaterials

The JJ-loaded wire array behaves as designed in the low dc current and low input power regime it was designed to operate in. The measured tuning of transmission indicates the tuning of cutoff frequency and permittivity predicted by the model. The effect on permittivity for one layer of eight wires is small but can be enhanced by adding more layers and with sufficient filling fraction achieve negative

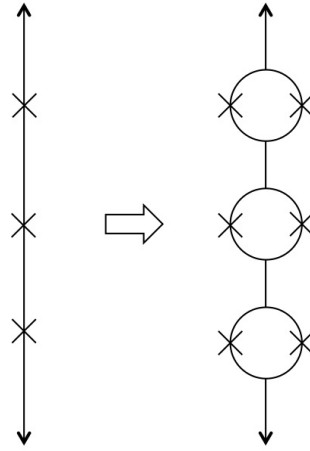


Figure 7.1: The Josephson junctions in the wire arrays could be replaced by dc SQUIDs.

values.

In addition to the desired tunable cutoff frequency and permittivity, I have observed interesting behavior at higher current and rf input power. The dynamics are very rich, highly hysteretic, and nonlinear, but the model is only valid in the limited range I designed these structures to operate. The next step is to develop a more widely applicable model which can be used to understand these results.

The junctions in the wires could be replaced with dc SQUIDs (superconducting loop with two junctions) as shown in Fig. 7.1, allowing the properties of the wires to be tuned with a perpendicular dc magnetic flux. These wire arrays would be sensitive to dc flux disorder and would have to be protected from stray fields by magnetic shielding.

7.3 Combined Metamaterial

One obvious next step is to create a large sample (with significant filling fraction) combining rf SQUID and JJ-loaded wire arrays to demonstrate a tunable refractive index that can achieve near-zero and negative values. Another possibility is taking these structures out of the waveguide geometry and measuring them in free space. For measurements of rf SQUID arrays in a free space geometry see Sec. B.3.

7.4 Josephson Metamaterials in the Quantum Limit

At temperatures much lower than 1 K [123], superconducting loops that include Josephson junctions can exhibit additional quantum properties commonly associated with atoms, *e.g.* quantized energy levels, superposition of states, and entanglement [124]. Superconducting qubits have been studied for their potential use in computing, but they are also interesting as potential meta-atoms because they can be considered true scaled-up versions of natural atoms due to the quantum-mechanical nature of their interaction with the electromagnetic field [125].

2D arrays of rf SQUIDs in the quantum limit (flux qubits) have been considered theoretically [50]. The effective permeability is predicted to tune with microwave power over a large range with low loss and the metamaterial is expected to exhibit transparency similar to EIT. This behavior is qualitatively similar to what we've observed experimentally in the classical limit, except in the quantum limit the states

maintain quantum coherence in the presence of the drive.

One approach to developing a quantum metamaterial is a quantum transmission line (QTL) metamaterial where the meta-atoms are coupled to each other (inductively or capacitively) such that excitations can be exchanged between the discrete energy levels of one meta-atom to the next. For example, flux qubits in a coplanar waveguide have been shown to have collective modes corresponding to coherent oscillations of the meta-atoms [126]. Such structures can be used for single microwave photon detection [127, 128].

In the charging-dominated regime ($E_C \gg E_J$ where E_C is the charging energy and E_J is the Josephson coupling energy), a transmission line containing coupled SQUIDs displays coherent quantum phase slips (CQPS) [129, 130]. CQPS describe the coherent transfer of vortices or fluxes along a superconducting wire and is considered the dual of the Josephson effect. In the opposite limit ($E_C \ll E_J$), a similar structure behaves as a superinductor [131].

Many other structures have been proposed *e.g.* a metamaterial composed of arrays of superconducting islands connected to bulk superconductors by two Josephson junctions in the quantum limit (charge qubits) embedded in a waveguide [132, 133]. This structure is predicted to show interesting behavior including the ability to act as a maser.

The field of quantum metamaterials is still very new and there is a lot more to explore. This is the future of Josephson metamaterials.

Appendix A: Justification of dc Flux Gradient

In Sec. 5.2.3 I assert that a dc flux gradient explains the loss of coherence observed in the experiment. In this appendix, I provide further justification for choosing this type of disorder.

A.1 Other Possible Forms of Disorder

I have simulated other likely types of disorder: a Gaussian-random distribution of coupling, dc flux, critical currents, and dissipation. Each of these (apart from dissipation) is associated with a loss of coherence at certain values of dc flux shown in Fig. A.1. This loss of coherence manifests as a reduction of the magnitude of the $S_{21}(\omega)$ dip which can be compared to measured S_{21} .

When the SQUIDS are identical and the flux is homogenous (no disorder) the coherence depends only slightly on dc flux (black curve in Fig. A.1 and shown in detail in Fig. 5.21). This slight dependence on dc flux depends on coupling between the SQUIDS, so it is not surprising that a gaussian distribution of the coupling exaggerates this effect (green curve in Fig. A.1).

When there is a Gaussian-random distribution of dc flux, the coherence is high at integer flux quanta where the slope of dc flux tuning is small; the coherence

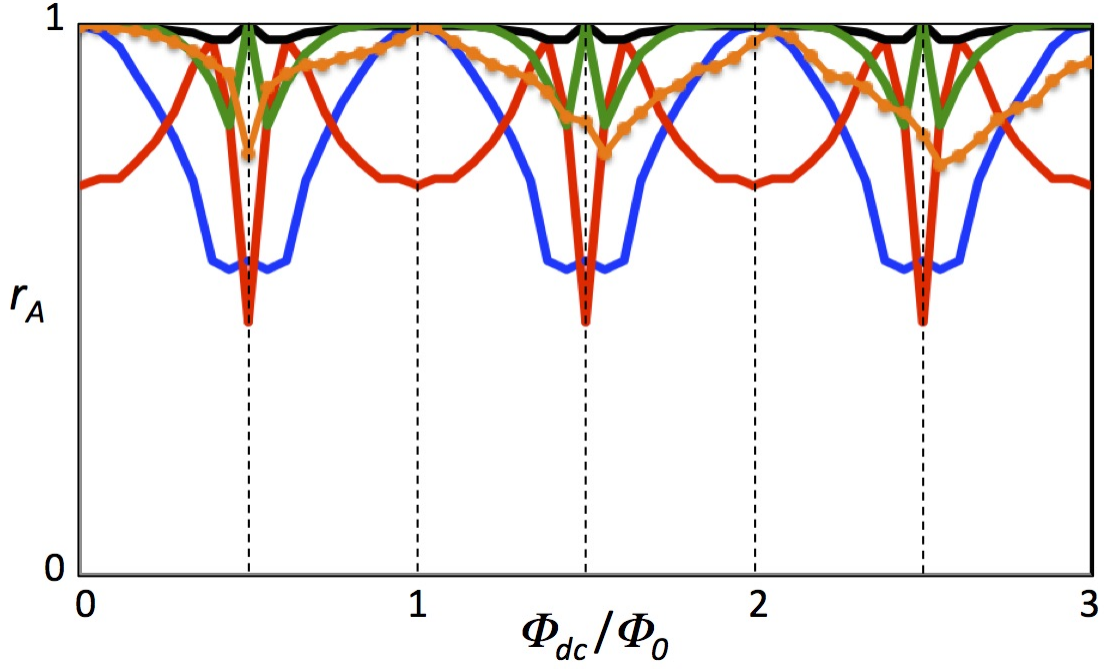


Figure A.1: Numerical simulation of coherence as a function of dc flux for various types of disorder in 21×21 array with $|\kappa_0| = 0.02$. black) no disorder; red) Gaussian distribution of critical currents with a standard deviation of $0.01 \mu\text{A}$; blue) Gaussian distribution of Φ_{dc}/Φ_0 with a standard deviation of 0.01; green) Gaussian distribution of coupling between SQUIDs with standard deviation of 0.015; orange) 10% dc flux gradient.

is lower for other flux values where the resonant frequency is more sensitive to dc flux (blue curve). Introducing a distribution of critical currents causes a loss of coherence near integer and half integer flux quanta, where the critical current has the strongest effect on the Josephson inductance and thus the resonant frequency; the coherence is unaffected at $\Phi_{dc}/\Phi_0 = 0.36$ where L_{JJ} diverges (red curve). A gaussian distribution of dissipation γ has no effect on coherence because dissipation affects the depth of the resonance dip but has no effect on its frequency.

All these possibilities are periodic in dc flux and show a suppression of coherence (and associated reduction of S_{21} dip) for dc flux values not seen in the experiment. To replicate the data the disorder must get worse with additional applied dc flux bias. The linear dc flux gradient is the only kind of disorder considered which replicates the loss of periodicity in dc flux, the reduction in maximum resonant frequency, the broader and shallower resonant dip, and splitting of the resonance dip at higher flux values.

A.2 Additional Gradient Worsens Coherence

If the array is perfectly aligned in the center of the coils used to apply dc bias field, I estimate that the edges should see 97% of the flux at the center. If the array is tilted or off-center there will be a greater distribution of flux across the array. This gradient causes the progressive loss of coherence at higher dc flux values we see in the experiment. The field could be made more uniform, for example by increasing the radius of the coil used to apply dc flux and this should improve the coherence.

Applying an additional gradient should make the coherence worse, which is shown in Fig. A.2. Figure A.2 (a) shows the familiar progressive loss of coherence with additional dc flux. In Fig. A.2 (b) there is an additional non-uniformity in the applied dc flux from a current through a straight along the short side of waveguide. The S_{21} curve is broader, shallower, and shows more splitting consistent with having lower coherence.

A.3 Direction of dc Flux Gradient

I also considered in simulation the direction of the linear flux gradient. When the gradient is along the edge of the array (as opposed to at a diagonal) the resonant dips are most distinct and most closely resemble the data; compare the local minima in $S_{21}(\omega)$ in Fig. A.3 with Fig. 5.22 at $\Phi_{dc}/\Phi_0 = 2.1$.

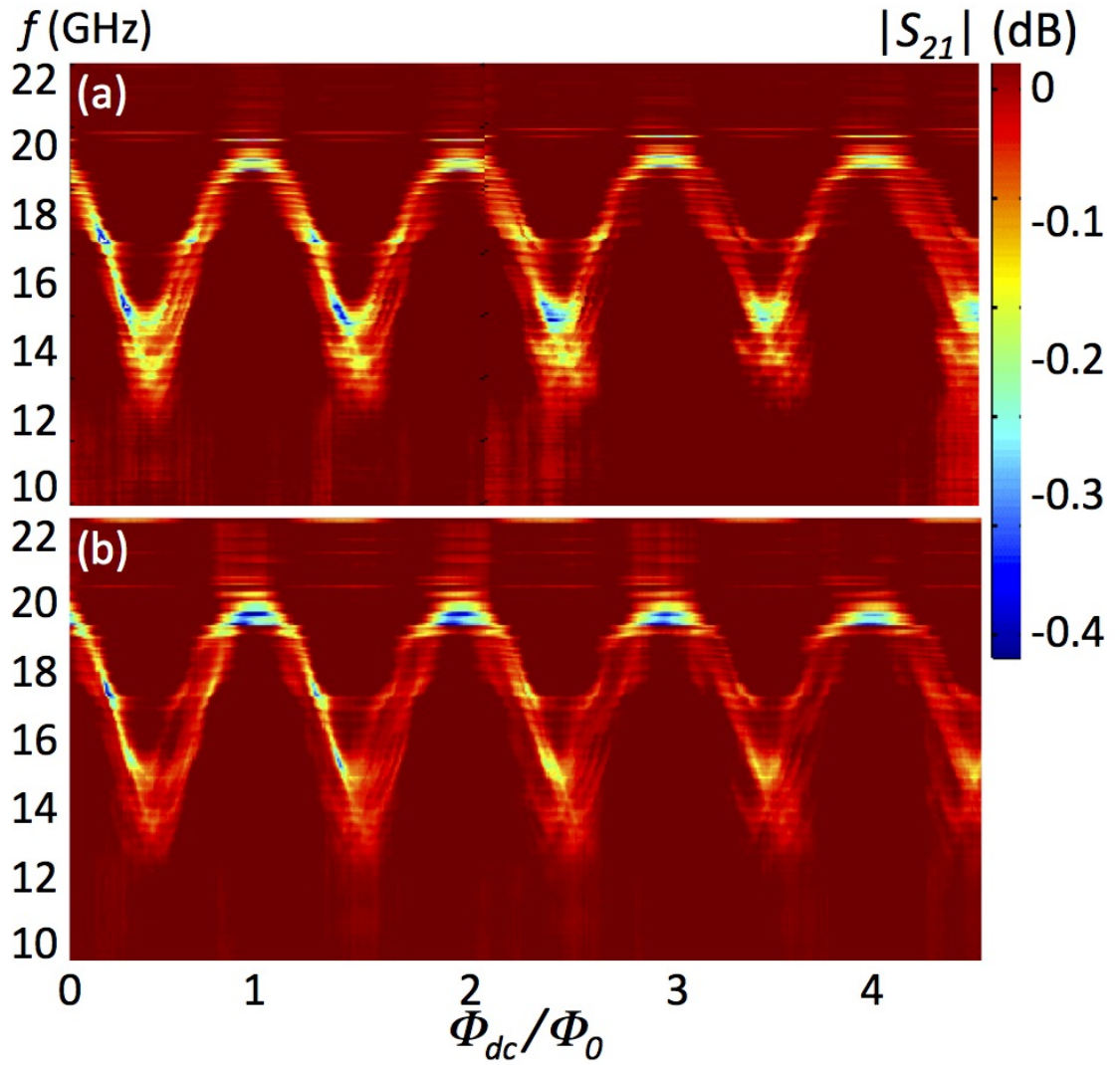


Figure A.2: Transmission as a function of frequency and dc flux in the 27x27 array with (a) no additional applied dc flux gradient (b) 30 mA through a straight along the short side of waveguide introduces an additional non-uniformity in the applied dc flux.

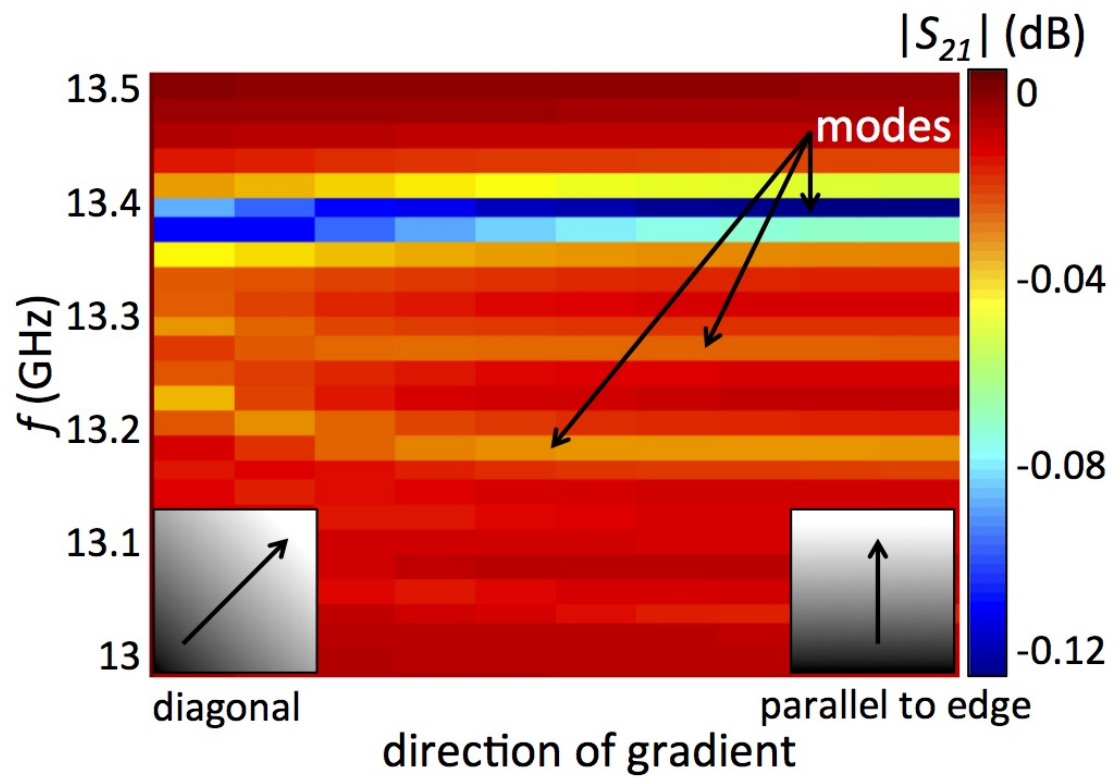


Figure A.3: Transmission as a function of frequency and direction of 10% linear dc flux gradient at $\Phi_{dc}/\Phi_0 = 2.1$ in 21x21 array with $|\kappa_0| = 0.02$.

Appendix B: Other Samples

A number of additional samples have been prepared, which have yet to produce any results worthy of publication. In this appendix, I summarize the design of these samples, and discuss some preliminary experimental results.

B.1 Individual SQUIDs

I designed (and Hypres prepared) a variety of individual SQUID samples of various sizes and ranges of the tunability. When studying the individual SQUID I focused on the largest design that took up the largest portion of the waveguide and presumably produced the strongest signal. The smaller individual SQUID designs were never measured. Their design parameters are listed in Tab. B.1. They all have vortex pinning holes in the superconducting layers.

In addition to the arrays discussed in Sec. 3.1.1 there were two other arrays prepared by Hypres: a 2x2 array of the same rf SQUIDs that were measured individually and a 7x7 array of the rf SQUIDs listed in the third entry of Tab B.1. Both of these arrays are shown in Fig. B.3.

Table B.1: Unmeasured individual rf SQUID design parameters

r_{in} (μm)	r_{out} (μm)	r_{JJ} (μm)	L (nH)	I_c (μA)	C (pF)	f_{min} (GHz)	f_{max} (GHz)	β_{rf}	Fig.
30	40	2	0.12	3.7	0.84	5.2	22	0.89	3.2 (b)
60	100	1.5	0.21	2.1	0.49	5.5	22	0.88	B.1 (c)
100	200	1.2	0.32	1.4	0.31	5.6	22	0.88	B.3
135	450	1.1	0.39	1.1	0.26	5.3	22	0.89	B.2
60	100	1.3	0.21	1.6	0.55	8.7	19	0.66	B.1 (a)
60	100	1.4	0.21	1.8	0.52	7.4	20	0.77	B.1 (b)
60	100	1.6	0.21	2.4	0.42	0	24	1.0	B.1 (d)
60	100	1.7	0.21	2.7	0.37	0	27	1.1	B.1 (e)

B.2 Arrays with Low Coherence

The 27x27 array and the 2x2 array show far worse coherence than the 21x21 arrays (discussed in Sec. 5.2.3), Fig. B.4. The 2x2 array in Fig. B.4 (a) is so incoherent that the tuning curves of each of the four SQUIDs are distinct. The different periods of dc flux tuning (but the same SQUID area) indicate the presence of a dc flux gradient.

The 27x27 array has some of the features seen in the 21x21 array, Fig. B.4 (b) *i.e.* the response is not periodic in dc flux, the maximum frequency decreases with increasing dc flux and the curve widens and fades, but these effects are much more dramatic here. A linear flux gradient such that one edge of the array is 75% of the other was necessary for the simulation to match the data.

In contrast, the measurements of the 11x11 array show some of the best co-

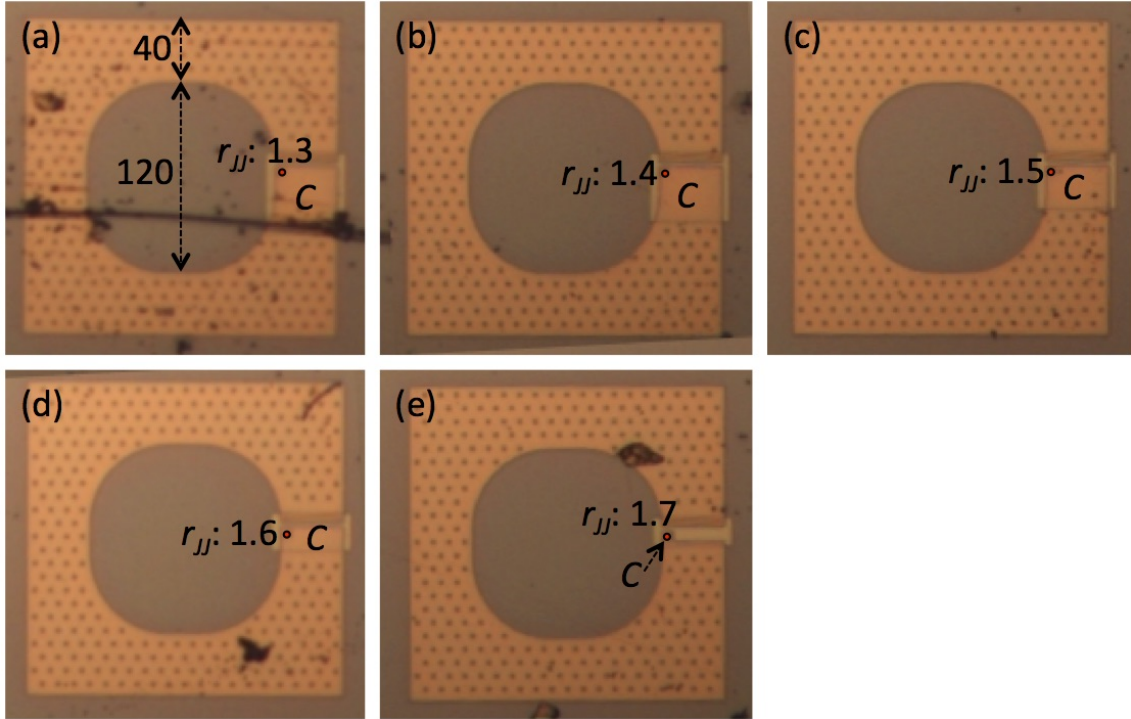


Figure B.1: Five individual rf SQUIDs listed in Tab. B.1 that have the same loop dimensions (but different areas of junction and overlap capacitance). All dimensions in μm .

herence of all the measured arrays, Fig. B.4 (c). A linear flux gradient such that one edge of the array is 95% of the other matched the simulation to the data. The resonant response as a function of dc flux is much more periodic.

An array of rf SQUIDs with a distribution of areas (similar to a SQIF, superconducting quantum interference filter), would have the same effect as a homogenous array with a dc field gradient; for the same applied field different amounts of flux are applied to the SQUIDs.

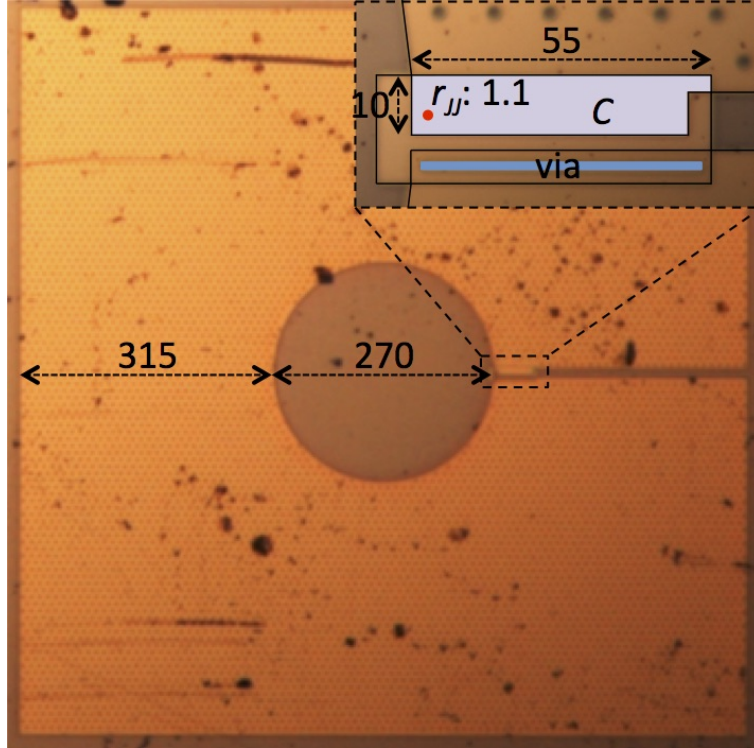


Figure B.2: Largest SQUID listed in Tab. B.1 (fourth entry). Inset: Enlargement of the area containing the junction (red) and the overlap capacitance (purple). All dimensions in μm .

B.3 SQUID Arrays: mm-Wave Free Space Measurements

The goal of the collaboration with the N. Zheludev group at University of Southampton was to measure rf SQUID metamaterials using their mm-wave setup shown in Fig. B.5. This setup accesses a higher frequency range (75-110 GHz) and uses a free space geometry (the samples are not constrained by a waveguide). The network analyzer generates microwaves which a frequency converter shifts to a

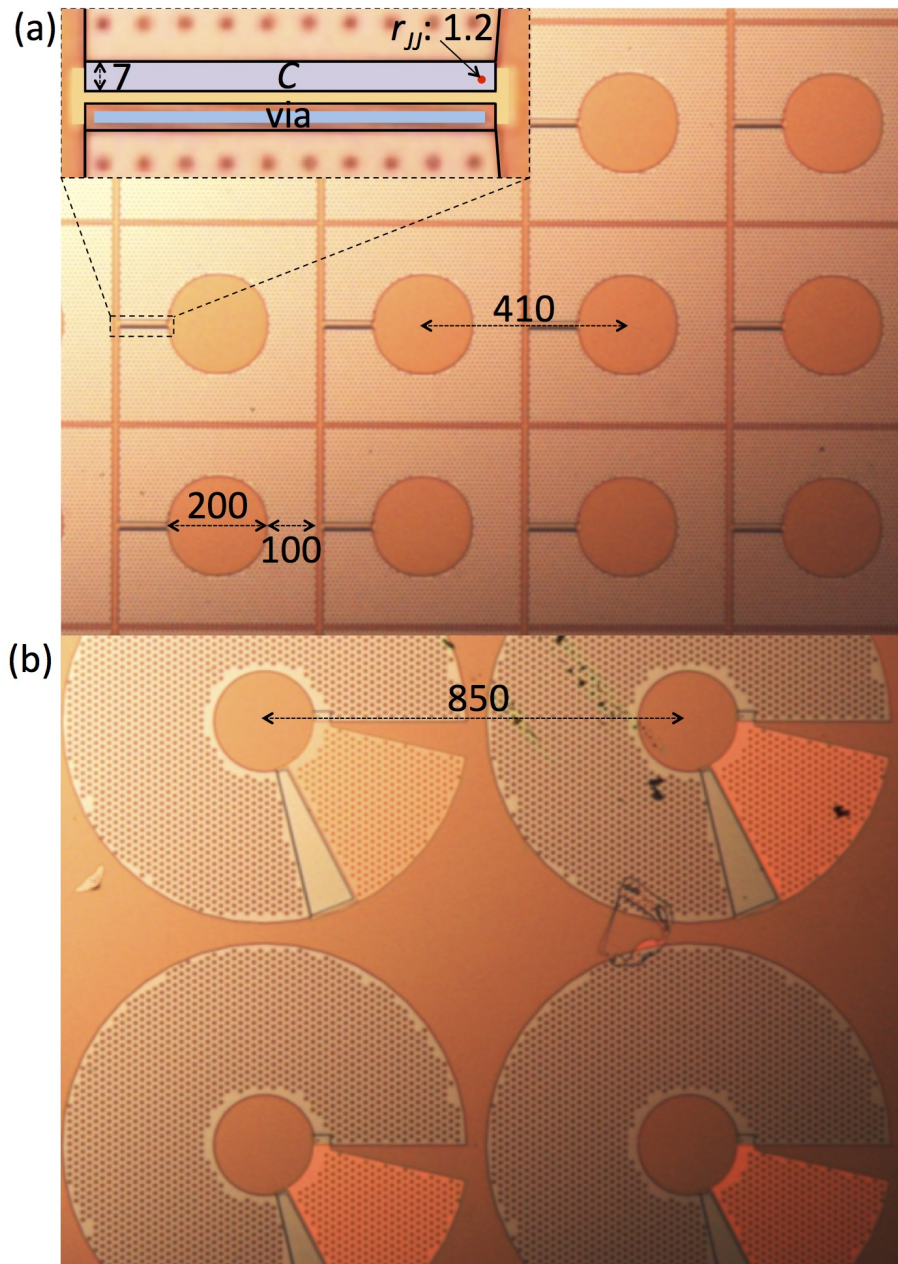


Figure B.3: (a) 7x7 rf SQUID array. Inset: Enlargement of the area containing the junction (red) and the overlap capacitance (purple). (b) 2x2 array (for details of individual SQUID see Fig. 3.1). All dimensions in μm .

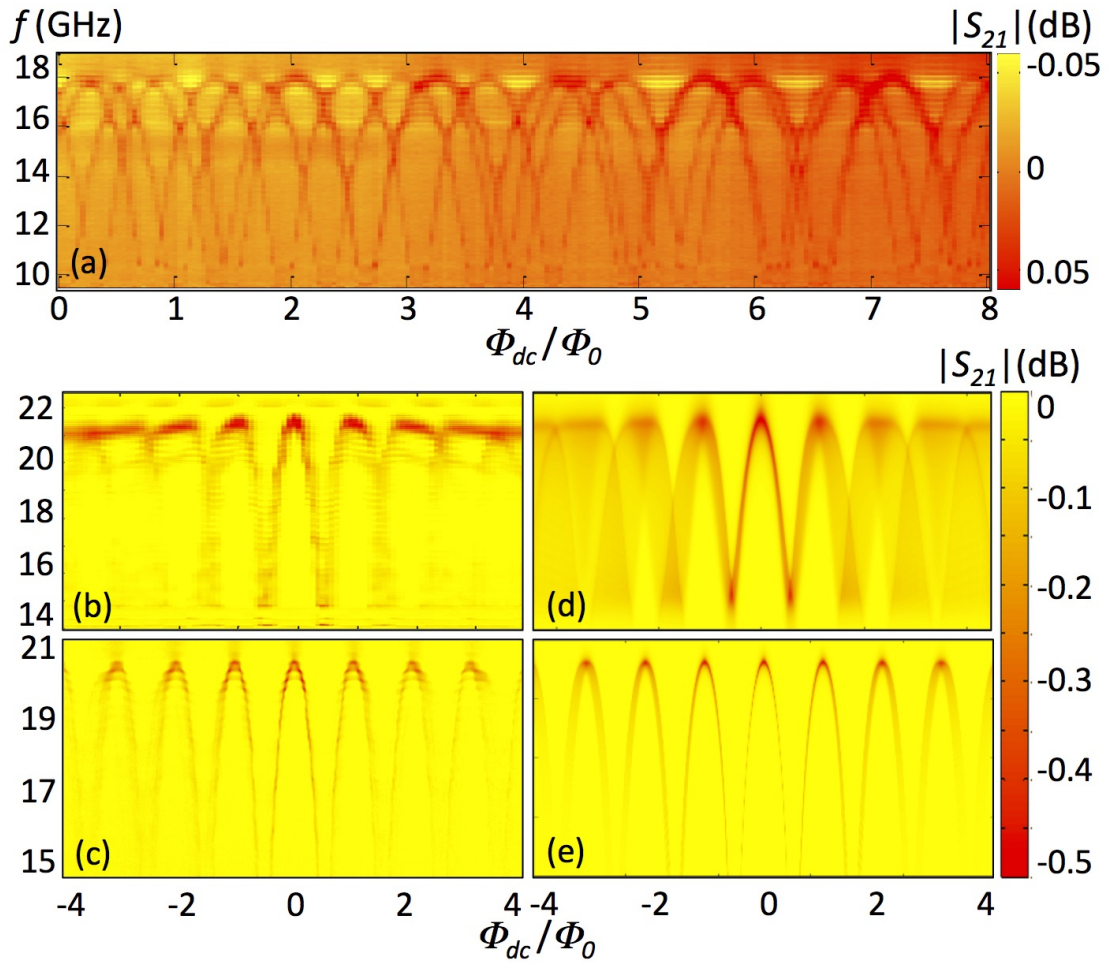


Figure B.4: (a) Measured transmission of 2x2 array, (b) 27x27 array, (c) and 11x11 array as a function of frequency and dc flux in the limit $\Phi_{rf}/\Phi_0 \ll 1$. (d) Simulated transmission in the 27x27 array with one edge of the array seeing 75% of the dc flux the other experiences. (e) Simulated transmission in the 11x11 array with one edge of the array seeing 95% of the dc flux the other experiences.

higher frequency range between 75 and 100 GHz. They pass through a horn antenna into free space and illuminate the sample which is in a cryostat with optical windows. On either side there are Brewster windows to reduce standing waves between these two windows. The signal is collected by another horn antenna and converted back to frequencies the network analyzer can measure.

The sample is attached with GE varnish to the mount, a 3 cm diameter sapphire wafer with two protruding rectangular blocks, shown in Fig. B.5 (d). The sample is mounted on the side of one of these blocks so that the mm-wave magnetic fields are perpendicular to the plane of the SQUIDs. The wafer is clamped along with a ring of indium between two pieces of OFHC copper. A magnetic coil is used to apply a dc magnetic field and a mu metal shield (with a hole to allow mm-waves to pass through the sample) manufactured by Amuneal protects the sample from stray fields.

The sample is a tightly coupled 50x50 array on a 4 mm silicon chip (four nominally identical copies) prepared by IREE, shown in Fig. B.6. To maximize the size of the signal, the number of SQUIDs and the coupling between them ($\kappa_0 = -0.02$) were made as large as possible. The SQUIDs are nonhysteretic and expected to be highly tunable with dc flux, $\beta_{rf} = 0.83$. The parameter values are as follows: $L = 136$ pH, $C = 25$ fF, $I_c = 2$ μ A, $R = 1.5$ k Ω .

Included in the run that produced these samples were SQUID samples that are designed for measurement in the usual setup, but the first batch of samples did not perform as expected; the dc flux tuning and geometric resonance were very different from what was expected from designed values. Unsurprisingly the samples

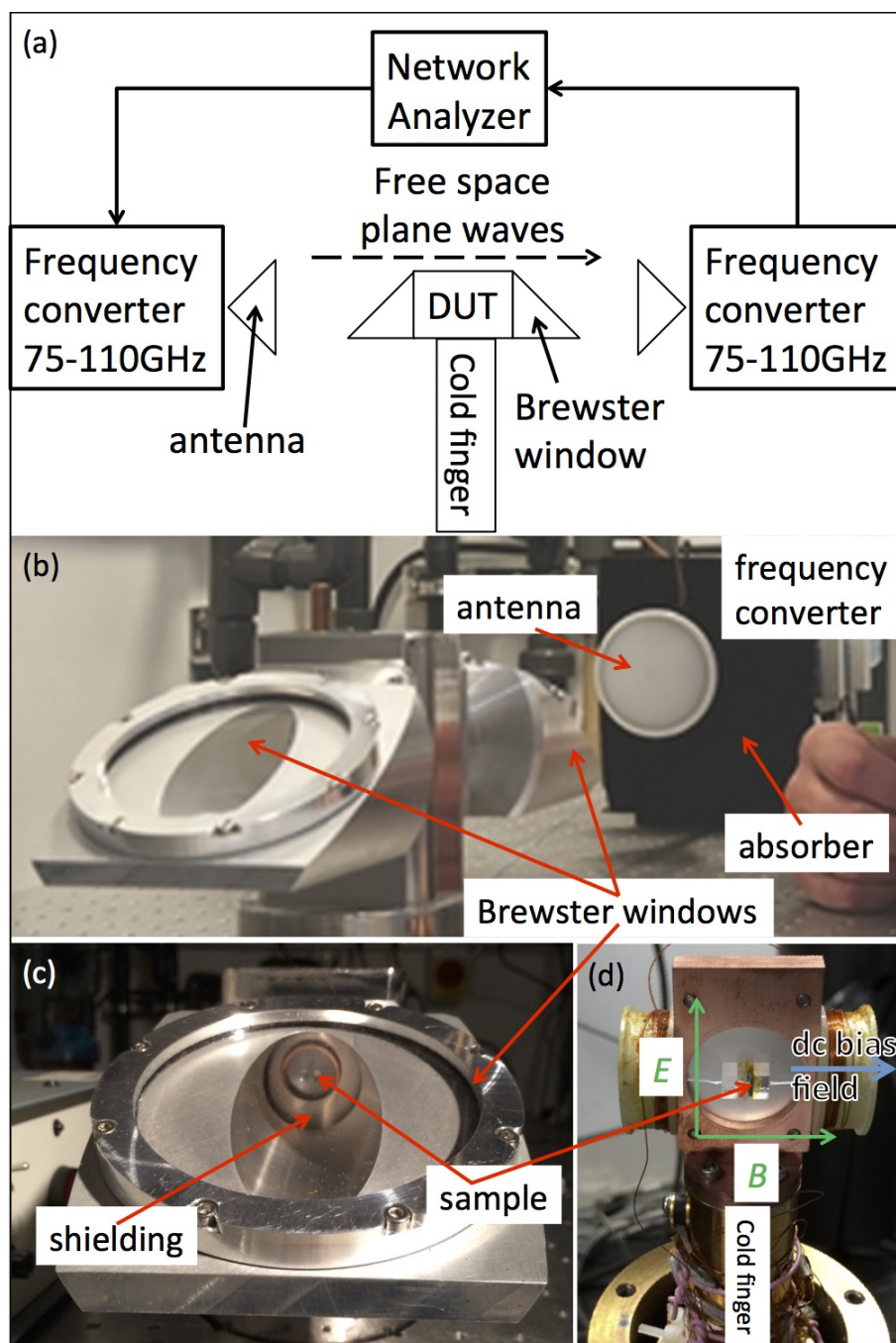


Figure B.5: mm-wave experimental setup

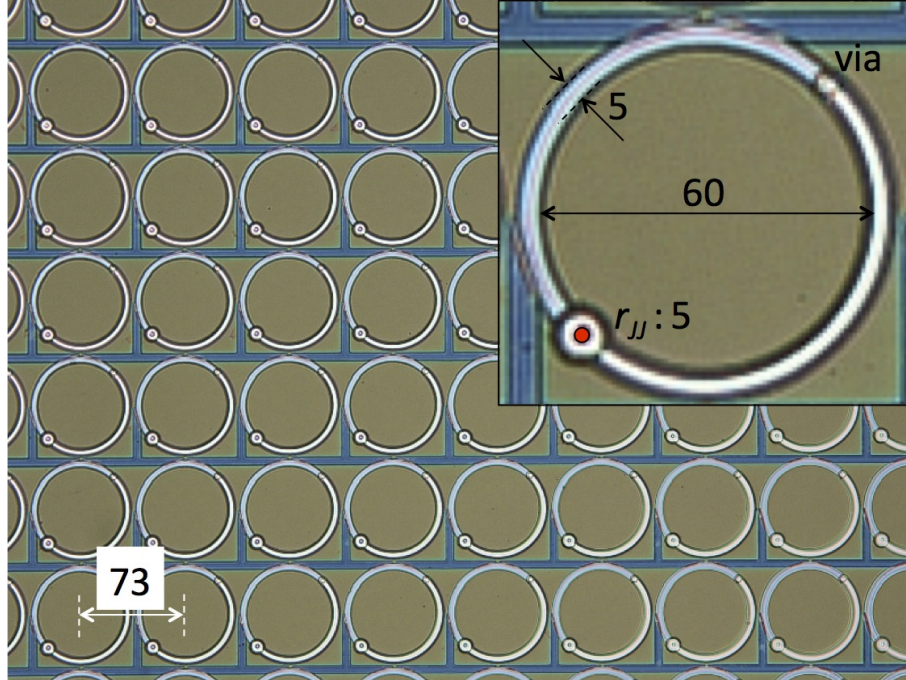


Figure B.6: Tightly coupled 50x50 array designed for the mm-wave experiment. Inset: Enlargement of the SQUID. All dimensions in μm .

measured in the mm-wave setup did not perform as designed either. The second batch was much better and behaved as designed in the usual setup. However, I was still unable to find a measurable signal in the mm-wave setup.

Figure. B.7 shows the predicted tuning behavior for this sample in response to dc and rf flux. I looked for features in transmission S_{21} and reflection S_{11} at low temperatures that disappear above the critical temperature; in particular I was searching for the geometric resonance around 90 GHz since it is a strong feature that appears at high input power so should be easily distinguished from the noise. I also looked for features that tuned with dc flux at various temperatures.

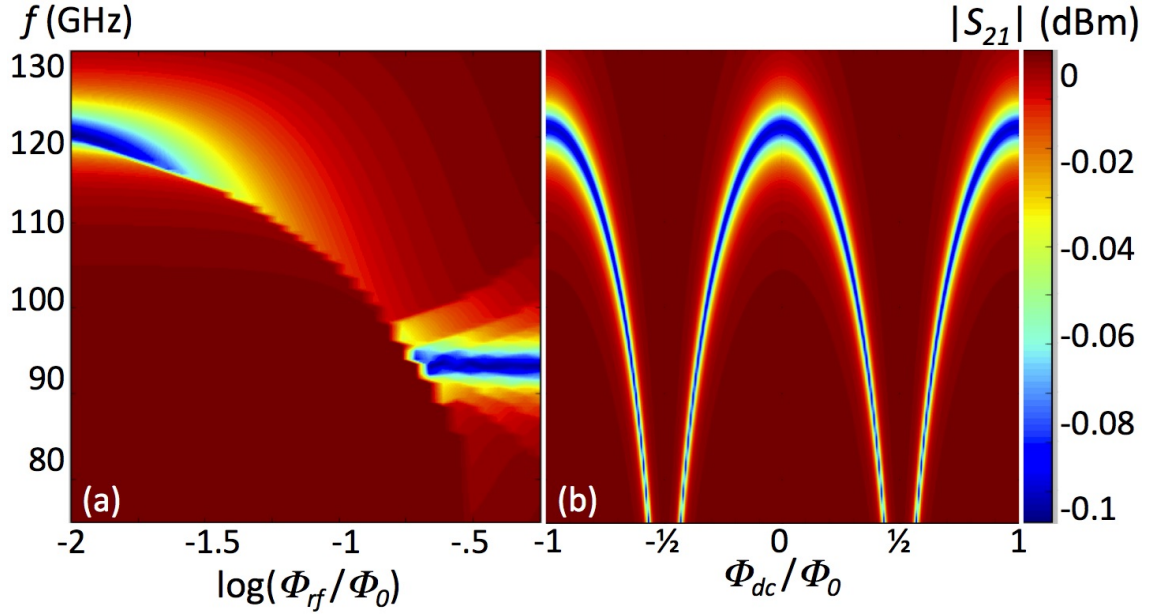


Figure B.7: (a) Simulated transmission using dissipated power calculation as a function of frequency and rf flux for $\Phi_{dc} = 0$ (b) and dc flux in the limit $\Phi_{rf}/\Phi_0 \ll 1$.

Two possible reasons that I could not detect the expected response are that the sample did not get cold enough or that it didn't interact strongly enough with the incident waves. If the sample was not cold enough to be below the superconducting transition there would be no signal from the SQUIDs. The thermometer on the cold finger was at 4 K but the sample was farther up and separated by several thermal interfaces. This could be tested with a four-point resistance measurement to determine if sample goes superconducting under the same mounting conditions as the mm-wave transmission measurements. One way to get the sample colder would be to design a sample holder to clamp directly onto the chip for better thermal

contact that does not rely on GE varnish.

Another possible reason I did not detect the expected response is that the sample doesn't interact strongly enough with the incident waves. The setup has successfully measured metamaterials patterned on 3 cm diameter wafers coupled to the electric field; the SQUID array is significantly smaller and rotated to couple to the magnetic field. I tried measuring all four chips (one on each side of a sapphire block) and narrowed the opening to magnetic shielding with aluminum foil so that a greater proportion of the transmitted waves interacted with the sample. Larger samples, possibly in a full three dimensional structure, would have a more significant impact on incident mm-waves.

Another possibility for the future is to design a version of the JJ-loaded wire arrays to fill a 3 cm diameter wafer and operate in this frequency range. These samples couple to electric field and so are more like samples the Zheludev group usually measures with this setup.

B.4 First Generation JJ-Loaded Wire Arrays

The first generation array of JJ-loaded wires was manufactured by Hypres. It consisted of 5 wires, 6 μm wide, spaced 1 mm apart. There were 30 junctions with 2 μm diameter equally spaced along the wire. The crucial difference between these samples and the second generation is the absence of contact pads. They were measured in the X band waveguide floating in Rohacell. The wires did not span the full height of the waveguide and did not electrically contact it.

Without contact pads there was no way to apply dc bias current so temperature was the only method of tuning the junctions. There was no distinguishable difference between transmission S_{21} measured at base temperature (4.5 K) and measured above T_c . In an attempt to make the tuning more dramatic additional layers were added so that eight chips (four layers) were measured at once, but this still did not produce any results.

Appendix C: Assigning Simulation Parameters

This appendix describes how the parameters in the simulation were chosen: whether they were calculated analytically or numerically or they were fit to agree with measurements.

C.1 rf SQUIDS

C.1.1 Input Flux

The rf flux through the SQUID loop was calculated from the magnetic field in the waveguide

$$\Phi_{rf} = 2\pi A_{loop} \sqrt{\frac{4P_0 k_0 \mu_0}{a_{dim} b_{dim} \omega}} \quad (\text{C.1})$$

where A_{loop} is the area of the SQUID loop, P_0 is the input power, a_{dim} is the longer and b_{dim} is the shorter of the two waveguide dimensions, and k_0 is the wave number in the empty waveguide.

To determine the dc flux through the loop, the field from the coil was measured with a gaussmeter as a function of current. The field is converted into a flux using the area of the SQUID loop. Zero dc flux is assigned where the resonant frequency and the coherence are maximum, which typically occurs when the current applied to

the coil is not zero (but less than current necessary to apply one flux quantum). The dc flux gradient is determined by matching the progressive widening of the $S_{21}(\Phi_{dc})$ dip seen in the data.

C.1.2 Mutual and Self-Inductance

The geometric inductance of a superconducting loop can be estimated analytically using the following empirically derived equation [134]

$$L = \mu_0 r_{out} \left[\frac{r_{in}}{r_{out}} - 0.197 \left(\frac{r_{in}}{r_{out}} \right)^2 - 0.031 \left(\frac{r_{in}}{r_{out}} \right)^6 + \left(1 + \frac{r_{in}}{r_{out}} \right) \tanh^{-1} \frac{r_{in}}{r_{out}} \right] \quad (\text{C.2})$$

where r_{in} is the inner radius and r_{out} is the outer radius of the loop.

The inductance can also be calculated numerically using FastHenry simulations [84]. FastHenry takes the geometry of the SQUID and using the two-fluid model it calculates inductance at a given frequency. For more details on the FastHenry calculation see Sec. D. Both analytic and numerical methods yield the same results ($< 2\%$ difference) which can be applied to the samples because the lithographic process to define the SQUIDs has little variation ($< 1 \mu\text{m}$).

The mutual inductance between SQUIDs in an array can also be obtained numerically from a FastHenry calculation or approximated using analytical expressions. The results of FastHenry calculations were used when modeling the two 21x21 arrays that were fabricated and measured. FastHenry was also used to determine the maximum possible coupling for these SQUIDs (when the SQUIDs are as close together as possible without overlapping).

Analytical approximations were used when performing simulations that involve continuously varying SQUID parameters and for simulation of the magneto-inductive modes. The Biot-Savart Law is used to calculate the magnetic field generated by a wire loop (the approximate geometry of an rf SQUID) far from the loop and in the same plane

$$B = \frac{\mu_0}{4\pi} \frac{I\pi r^2}{d^3} \quad (\text{C.3})$$

where I is the current in the loop, d is the distance from the center of the loop, and r is the radius of the loop. It is assumed that the magnetic field at the center of the loop is the same over its entire area. The mutual inductance is calculated with d as the center-to-center distance.

$$M = \frac{BA}{I} = \frac{\mu_0\pi r^4}{4d^3} \quad (\text{C.4})$$

The analytical and numerical calculations do not yield identical results for the coupling matrix $\bar{\kappa}$; in the numerical calculation, the coupling falls off faster with distance. When κ_{avg} is the same, the analytically and numerically determined $\bar{\kappa}$ produce the same results for the frequency and depth of the $S_{21}(\omega)$ dip on the primary resonance. These quantities do not depend on the details of which SQUIDs are oscillating, but on the sum of the amplitude of $\hat{\delta}$.

The magneto-inductive modes are affected by the details of which SQUIDs are oscillating; for the highest coupling case calculated by FastHenry (when the SQUIDs are as close as possible without overlapping) the coupling is different in different directions and this has a strong effect on the MI modes. Compare Fig. C.1 which uses the numerical FastHenry results with Fig. 5.11 which uses the analytical

approximation with $|\kappa_0| = 0.06$ (both have the same κ_{avg}). The primary mode is the same, but the asymmetric coupling breaks the symmetry in the lower frequency modes; there are more MI modes and they have reduced symmetry. These modes have a greater distribution of phases and the solutions for $\hat{\delta}$ are a broader mix of eigenvectors (compare Fig. C.1 with (b) Fig.5.14 (b)).

C.1.3 Fit Parameters

The geometric frequency f_{geo} (Eq. 5.8) measured at high rf flux is used to fit the capacitance C of the SQUID, holding the inductance and coupling fixed at the values described above. The zero dc flux resonant frequency $f_0(\Phi_{dc} = 0)$ (Eq. 5.6) measured in the limit $\Phi_{rf}/\Phi_0 \ll 1$ is used to fit the critical current at that temperature. A comparison of the fit values and the nominal design values can be found in Tab. C.1.

In the dissipated power calculation the resistance R is fit to the depth of the $S_{21}(\omega)$ dip. When using the effective medium calculation there are additional parameters, the filling fraction F and the length of the medium l , that affect the width and depth of the resonance (but not the frequency). These variables are not independent; their ratio F/l is what determines the shape of the resonance dip. The appropriate choice for F and l is not obvious especially when considering a single meta-atom. In practice, l is fixed at the diameter of the rf SQUID or length of the array and then R and F are fit to the width and depth of the resonance dip.

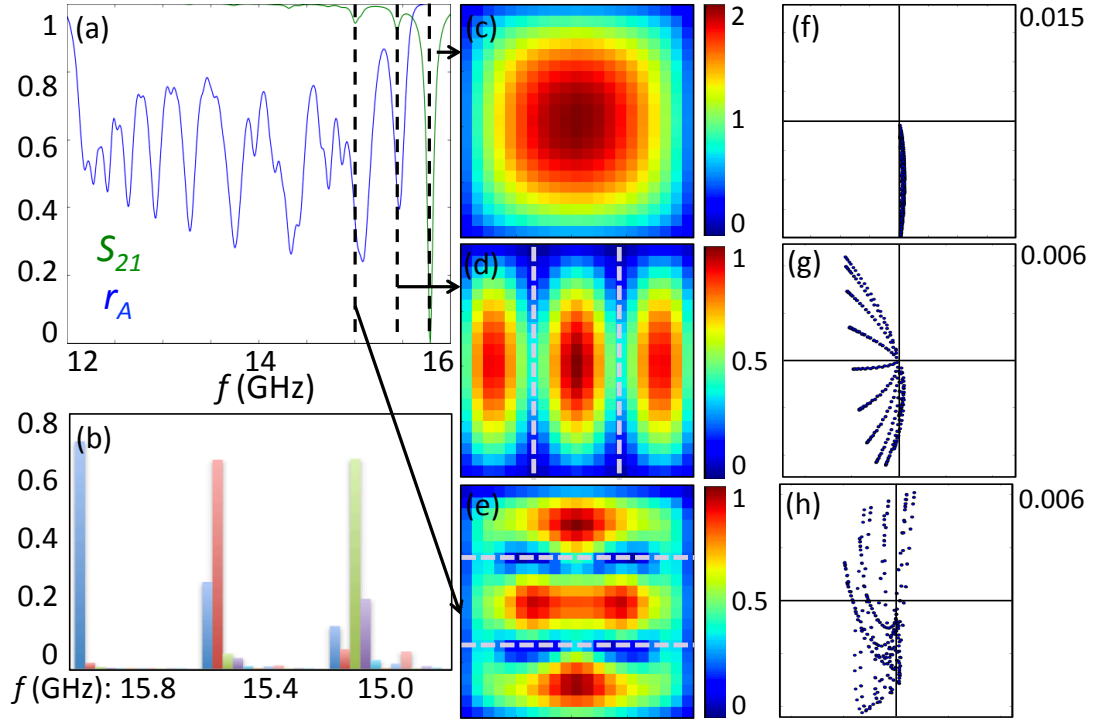


Figure C.1: (a) Simulated transmission and coherence for 21x21 array with maximum coupling ($\bar{\kappa}$ determined by FastHenry simulations) in the limit $\Phi_{rf}/\Phi_0 \ll 1$. (b) The dot product of normalized solutions for $\hat{\delta}$ and the first nine eigenvectors of the matrix in Eq. 2.25. (c-e) Simulated spatial distribution of amplitude of $\hat{\delta}$ for the three most prominent modes; dashed white lines show boundary between regions out of phase by π . (f-h) Scatter plot where the amplitude and phase (relative to rf drive) of $\hat{\delta}$ is represented in polar coordinates.

Table C.1: Comparison of nominal and fit values for capacitance and critical current in the single rf SQUID and arrays.

	C_{nom} (pF)	C_{fit} (pF)	$I_{c,nom}(T = 4.2 \text{ K})$ (μA)	$I_{c,fit}(T = 5.5 \text{ K})$ (μA)
single	0.32	0.42	0.97	0.75
11x11	0.88	2.1	4.5	5.4
21x21	1.8	2.1	1.4	2.0
27x27	0.84	0.93	3.7	2.2

C.2 JJ-Loaded Wire Array

The length of the wires, the spacing between them, and their inductance are determined by the lithographic which has little variation. The inductance is determined analytically

$$L_{geo} = \frac{\mu_0 l \lambda}{a \pi^2} \ln \frac{2a}{b} \left(\frac{\sinh \frac{b}{\lambda}}{\cosh \left(\frac{b}{\lambda} - 1 \right)} - 1 \right) \quad (\text{C.5})$$

where l is the length of the wire, a is the width of the wire, b is the thickness of the film, and λ is the London penetration depth [135].

The critical current for a given temperature can be determined by measuring either the transmission or dc voltage as a function of increasing dc current. The critical current is the current at which the transmission drops and the voltage stops being zero. The critical current of these junctions was designed to be $2 \mu\text{A}$, but the measured value was $0.25 \mu\text{A}$. The other samples from this run also had critical currents that deviated significantly from their design values.

The ratio of resistance and capacitance is determined by the re-trapping cur-

rent, which is measured like I_c but with decreasing dc bias current. The length of the medium is set at twice the spacing of the wires and the filling fraction is adjusted to match the magnitude of the tuning.

Appendix D: Scripts

This appendix provides descriptions of the Python scripts used to simulate 2D rf SQUID arrays and arrays of JJ-loaded wire arrays. The files can be found on the Anlage group backup space: `Melissa/PythonScripts`.

“LinearCalc.py” calculates \hat{a} and \hat{b} (where $\hat{\delta}(t) = \hat{a} \sin \omega t + \hat{b} \cos \omega t$) for a coupled 2D SQUID array in the linear limit $\Phi_{rf}/\Phi_0 \ll 1$ by solving Eq. 2.25. This is used to calculate transmission through the waveguide S_{21} (using either the dissipated power (Sec. 2.5.1) or effective medium (Sec. 2.5.2) method) and coherence r_A as a function of frequency, coupling strength, and/or dc flux through the SQUIDs (including dc flux gradients in any direction). It can also be used to calculate the quality of the resonance Q and the linear eigenmodes of the array.

“NonLinCalc.py” begins by numerically solving the full system of coupled nonlinear differential equations Eq. 2.22, for $\hat{\delta}(t)$ and $\hat{\delta}'(t)$ for a coupled 2D SQUID array. \hat{a} and \hat{b} are extracted from the solutions and as in the linear case used to calculate values of interest.

When solving nonlinear equations the initial conditions must be carefully chosen; rf SQUIDs have been shown to be multistable [57]. At the beginning of the calculation the initial conditions are set to zero $\delta(0) = 0$ and $\delta'(0) = 0$. The sim-

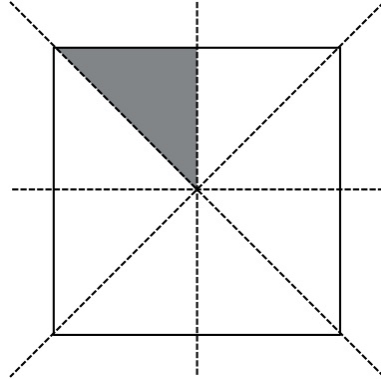


Figure D.1: Dashed lines indicate axes of symmetry in square array. The shaded region indicates the portion of the array that has unique solutions and must be calculated.

ulation runs for sufficient time for the transient behavior to die away. The next calculation in the sweep uses the final state of the previous calculation for its initial conditions. This choice of initial conditions reproduces the hysteric behavior seen in the experiment.

Solving the nonlinear equations takes significantly longer than the linearized form. One technique employed to reduce the calculation time is to take advantage of the symmetry in the array to reduce the number of equations. A 2D array of identical SQUIDs with identical drive has four axes of symmetry allowing the number of nonlinear equations to be reduced by a factor of eight as illustrated in Fig. D.1.

Another technique to reduce calculation time is to parallelize the computation and run it on an HPC (high performance computing) cluster, in this case

Depththought. It is not possible to run all the computations for various frequencies and rf flux values in parallel because of the care that must be given to the initial conditions, but it is possible to assign each sweep to a different node in the cluster. Each frequency sweep (for a fixed rf flux) was submitted to a different node on Depththought as a separate job.

“generatefile.py” creates a file that can be input into FastHenry to determine the self-inductance and mutual inductance of a 2D SQUID array. Given the number of SQUIDs, their size, and separation, this script describes the geometry of the array by defining nodes, connections between them, and ports. The SQUIDs are rectangular like the 21x21 arrays. It also specifies the other variables FastHenry requires: frequency, film thickness, penetration depth, and how many pieces to break the structures into.

“wireEM.py” solves the single junction (Eq. 2.2) for $\delta(t)$ and $\delta'(t)$ choosing initial conditions as described above. The program then calculates transmission S_{21} as outlined in Sec. 2.5.2.

Appendix E: Results for Unmodified Kuramoto Order Parameter

These early calculations only consider coherence using the bare Kuramoto model order parameter r which uses the phase of $\hat{\delta}$ unweighted by the amplitude of oscillation.

E.1 Relationship Between Transmission and Coherence

In an effort to extract coherence from measured transmission, I explored the relationship between these two quantities in simulation. I found a power law relationship between the bare Kuramoto order parameter r and the full width at half max of $S_{21}(\Phi_{dc})$ dips, see Fig. E.1. The relationship does not depend on the magnitude of the applied linear dc flux gradient and the slope is also consistent for different frequencies. Unfortunately, when I started using the modified Kuramoto order parameter r_A which weights the oscillators by their amplitude, this relationship no longer held.

E.2 Pair of SQUIDs in the High rf Flux Limit

I performed simulations on pairs of SQUIDs to understand how coupling and dc flux disorder affect the resonance response in the high rf flux limit without running

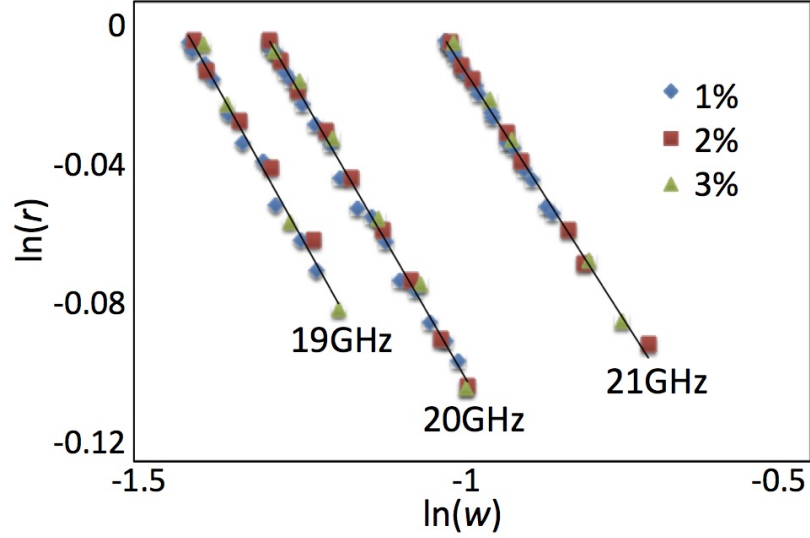


Figure E.1: Simulated coherence (phase only) as a function of full width at half max of $S_{21}(\Phi_{dc})$ dips for 21x21 array with $|\kappa_0| = 0.02$ for various frequencies and dc flux gradients.

intense computations required for larger arrays. Running on the HPC cluster allowed me to run complete 2D array calculations and I never revisited the two-SQUID case after defining the modified order parameter.

E.2.1 Effect of Coupling on Coherence and Transparency

To understand the effect of coupling in the nonlinear regime, I considered a two SQUID case where one SQUID had no dc flux through it and in the other $\Phi_{dc}/\Phi_0 = 0.01$ (This flux difference is small enough that there is still only one resonance dip in $S_{21}(\omega)$). Figure E.2 (a) shows how Δf (which is related to the

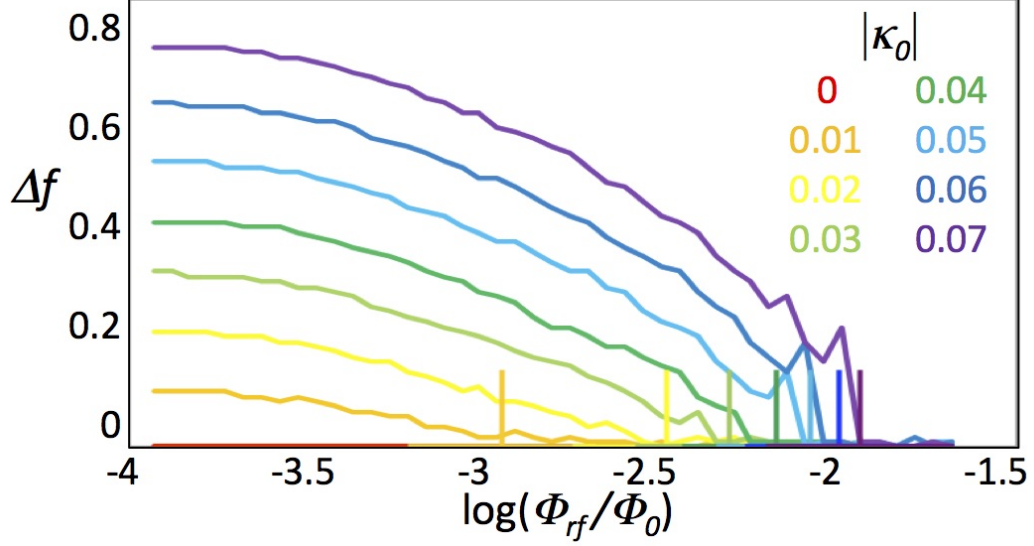


Figure E.2: Numerical results of two SQUIDs with $\Phi_{dc}/\Phi_0 = 0$ and $\Phi_{dc}/\Phi_0 = 0.01$ for the frequency difference between the minimum of $S_{21}(\omega)$ and $r(\omega)$ as a function of rf flux for different values of coupling

coherence on resonance as shown in Sec. 5.1), depends on increasing rf flux for different values of coupling. Consistent with the behavior observed in the limit $\Phi_{rf}/\Phi_0 \ll 1$, when there is no coupling $\Delta f = 0$, but as coupling increases the frequency difference grows and so does coherence on resonance.

As rf flux increases the frequency difference decreases and eventually reaches zero when the effective coupling (defined in Sec. 5.1) is approximately 1/2, marked in Fig. E.2 (a) with the vertical lines. Coherence on resonance decreases with increasing rf flux because of the reduced effective coupling between the SQUIDs.

E.2.2 Effect of Unequal dc Flux on Coherence and Transparency

To understand the effect of unequal flux in the nonlinear regime I considered the case of two uncoupled SQUIDs for various values of dc flux through one of the SQUIDs with the other SQUID fixed at zero flux. The flux separation was kept small enough that only one resonance dip was observed in $S_{21}(\omega)$. Figure E.3 (a) shows how coherence on resonance responds to rf flux for different amounts of flux disorder. At low rf flux the more different the flux is the less coherent the SQUIDs are. If there is any flux difference between the two SQUIDs there is a decrease in coherence with increasing rf flux. At high rf flux the coherence does not depend as strongly on the amount of flux difference. In this uncoupled case the suppression of coherence is directly related to the difference in the resonant frequencies of the two SQUIDs. However, for the coupled arrays considered in Sec. 5.2.3 we find that rf flux increases coherence in the presence of dc flux disorder.

Figure E.3 (b) shows that transparency is unaffected by the dc flux disorder despite the precipitous drop in coherence. This makes sense because the SQUIDs are acting individually and both taken alone are transparent in this regime. In Sec. 5.2.3 we show that in the presence of more substantial disorder the transparency region of arrays is impacted.

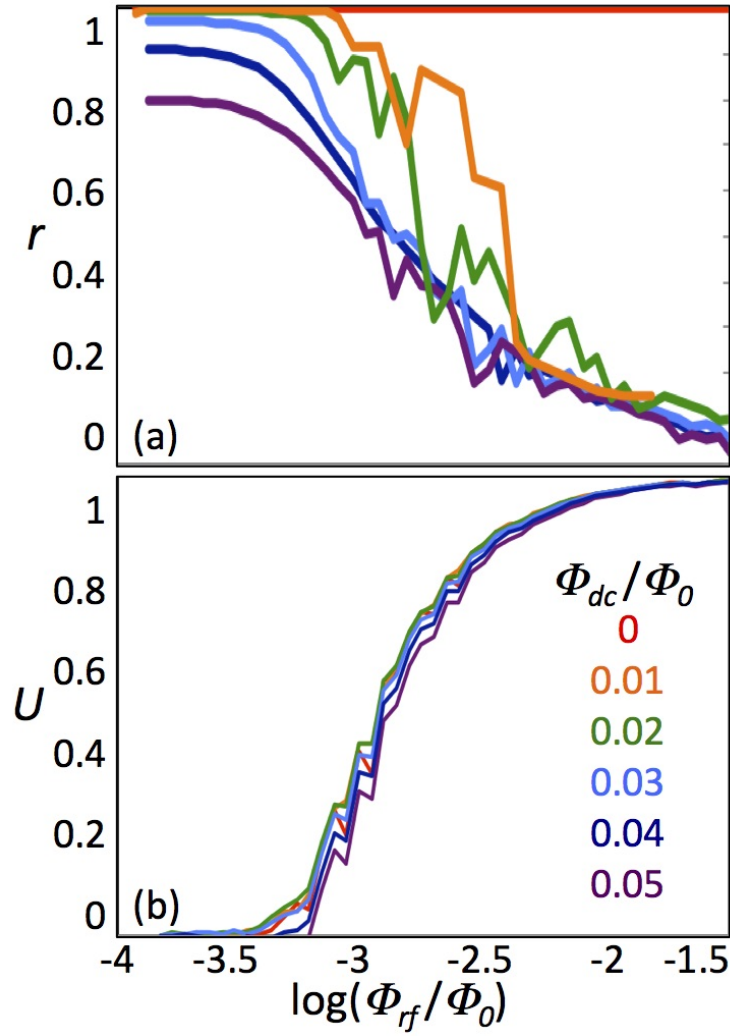


Figure E.3: (a) Simulated coherence (b) and transparency for two uncoupled SQUIDs as a function of applied rf flux for different values of dc flux in one of the SQUIDs. dc flux through the other SQUID was fixed at zero.

Bibliography

- [1] T. P. Orlando and K. A. Delin. *Foundations of Applied Superconductivity*. Addison-Wesley, Reading, MA, 1991.
- [2] M. Tinkham. *Introduction to Superconductivity*. McGraw-Hill, New York, 2nd edition, 1996.
- [3] K. K. Likharev. *Dynamics of Josephson Junctions and Circuits*. Gordon and Breach, New York, 1986.
- [4] C. A. Hamilton, C. Burroughs, and K. Chieh. Operation of NIST Josephson array voltage standards. *J. Res. Natl. Inst. Stand. Technol.*, 95:219–235, 1990.
- [5] V. G. Veselago. Electrodynamics of materials with negative index of refraction. *Phys.-Usp.*, 46(7):764–768, 2003.
- [6] D. R. Smith, W. J. Padilla, D. C. Vier, S. C. Nemat-Nasser, and S. Schultz. Composite medium with simultaneously negative permeability and permittivity. *Phys. Rev. Lett.*, 84(18):4184–4187, 2000.
- [7] R. A. Shelby, D. R. Smith, and S. Schultz. Experimental verification of a negative index of refraction. *Science*, 292(5514):77–79, 2001.
- [8] A. Alu and N. Engheta. Pairing an epsilon-negative slab with a mu-negative slab: Resonance, tunneling and transparency. *IEEE Trans. Antennas Propag.*, 51(10):2558–2571, 2003.
- [9] D. Schurig, J. J. Mock, B. J. Justice, S. A. Cummer, J. B. Pendry, A. F. Starr, and D. R. Smith. Metamaterial electromagnetic cloak at microwave frequencies. *Science*, 314(5801):977–980, 2006.
- [10] J. B. Pendry. Negative refraction makes a perfect lens. *Phys. Rev. Lett.*, 85(18):3966–3969, 2000.
- [11] Z. Jacob, L. V. Alekseyev, and E. Narimanov. Optical hyperlens: Far-field imaging beyond the diffraction limit. *Opt. Express*, 14(18):8247–8256, 2006.

- [12] N. I. Landy, S. Sajuyigbe, J. J. Mock, D. R. Smith, and W. J. Padilla. Perfect metamaterial absorber. *Phys. Rev. Lett.*, 100(20):7402, 2008.
- [13] S. M. Anlage. The physics and applications of superconducting metamaterials. *J. Opt.*, 13(2):024001–024011, 2011.
- [14] P. Jung, A. V. Ustinov, and S. M. Anlage. Progress in superconducting metamaterials. *Supercond. Sci. Technol.*, 27(073001), 2014.
- [15] Z. Liu, N. Fang, T. Yen, and X. Zhang. Rapid growth of evanescent wave by a silver superlens. *Appl. Phys. Lett.*, 83(25):5184–5186, 2003.
- [16] R. Ruppin. Surface polaritons of a left-handed medium. *Phys. Lett. A*, 277:61–64, 2000.
- [17] R. Ruppin. Surface polaritons of a left-handed material slab. *J. Phys.: Condens. Matter*, 13:1811–1819, 2001.
- [18] F. D. M. Haldane. Electromagnetic surface modes at interfaces with negative refractive index make a ‘not-quite-perfect’ lens, 2002.
- [19] D. R. Smith, D. Schurig, M. Rosenbluth, S. Schultz, S. A. Ramakrishna, and J. B. Pendry. Limitations on subdiffraction imaging with a negative refractive index slab. *Appl. Phys. Lett.*, 82(10):1506–1508, 2003.
- [20] T. Koschny, R. Moussa, and C. M. Soukoulis. Limits on the amplification of evanescent waves of left-handed materials. *J. Opt. Soc. Am. B*, 23(3):485–489, 2006.
- [21] R. W. Ziolkowski and A. D. Kipple. Application of double negative materials to increase the power radiated by electrically small antennas. *IEEE Trans. Antennas Propag.*, 51(10):2626–2640, 2003.
- [22] R. W. Ziolkowski and A. Erentok. Metamaterial-based efficient electrically small antennas. *IEEE Trans. Antennas Propag.*, 54(7):2113–2130, 2006.
- [23] A. Schilling, M. Cantoni, J. D. Guo, and H. R. Ott. Superconductivity above 130 K in the Hg-Ba-Ca-Cu-O system. *Nature*, 363(6424):56–58, 1993.
- [24] S. A. Cybart, E. Y. Cho, T. J. Wong, B. H. Wehlin, M. K. Ma, C. Huynh, and R. C. Dynes. Nano Josephson superconducting tunnel junctions in $\text{YBa}_2\text{Cu}_3\text{O}_{7-\delta}$ directly patterned with a focused helium ion beam. *Nature Nanotech.*, 2015.
- [25] R. W. Simon, R. B. Hammond, S. J. Berkowitz, and B. A. Willemsen. Superconducting microwave filter systems for cellular telephone base stations. *Proceedings of the IEEE*, 92(10):1585–1596, 2004.

- [26] J. B. Pendry, A. J. Holden, D. J. Robbins, and W. J. Stewart. Magnetism from conductors and enhanced nonlinear phenomena. *IEEE Trans. Microw. Theory Techn.*, 47(11):2075–2084, 1999.
- [27] A. A. Zharov, I. V. Shadrivov, and Y. S. Kivshar. Nonlinear properties of left-handed metamaterials. *Phys. Rev. Lett.*, 91(3):037401, 2003.
- [28] I. V. Shadrivov, S. K. Morrison, and Y. S. Kivshar. Tunable split-ring resonators for nonlinear negative-index metamaterials. *Opt Express*, 14(20):9344–9349, 2006.
- [29] M. Lapine, I. V. Shadrivov, and Y. S. Kivshar. Nonlinear metamaterials. *Rev. Mod. Phys.*, 86:1093–1123, 2014.
- [30] M. Ricci, N. Orloff, and S. M. Anlage. Superconducting metamaterials. *Appl. Phys. Lett.*, 87(3):034102, 2005.
- [31] M. C. Ricci and S. M. Anlage. Single superconducting split-ring resonator electrostatics. *Appl. Phys. Lett.*, 88(26):264102, 2006.
- [32] J. Q. Gu, R. Singh, Z. Tian, W. Cao, Q. R. Xing, M. X. He, J. W. Zhang, J. G. Han, H. T. Chen, and W. L. Zhang. Terahertz superconductor metamaterial. *Appl. Phys. Lett.*, 97(7):071102, 2010.
- [33] H. Chen, H. Yang, R. Singh, J. F. O’Hara, A. K. Azad, S. A. Trugman, Q. X. Jia, and A. J. Taylor. Tuning the resonance in high-temperature superconducting terahertz metamaterials. *Phys. Rev. Lett.*, 105(247402):1–4, 2010.
- [34] J. Wu, B. Jin, Y. Xue, C. Zhang, H. Dai, L. Zhang, C. Cao, L. Kang, W. Xu, J. Chen, and P. Wu. Tuning of superconducting niobium nitride terahertz metamaterials. *Opt. Express*, 19(13):12021–12026, 2011.
- [35] V. Savinov, V. A. Fedotov, S. M. Anlage, P. A. J. de Groot, and N. I. Zheludev. Modulating sub-THz radiation with current in superconducting metamaterial. *Phys. Rev. Lett.*, 109(243904):1–5, 2012.
- [36] V. Savinov, V. A. Fedotov, P. A. J. de Groot, and N. I. Zheludev. Radiation-harvesting resonant superconducting sub-THz metamaterial bolometer. *Supercond. Sci. Technol.*, 26(084001):1–4, 2013.
- [37] B. G. Ghamsari, J. Abrahams, S. Remillard, and S. M. Anlage. High-temperature superconducting multi-band radio-frequency metamaterial atoms. *Appl. Phys. Lett.*, 102(013503):1–4, 2013.
- [38] B. G. Ghamsari, J. Abrahams, S. Remillard, and S. M. Anlage. High-temperature superconducting spiral resonator for metamaterial applications. *IEEE Trans. Appl. Supercond.*, 23(3):1500304, 2013.

- [39] R. Singh, D. R. Chowdhury, J. Xiong, H. Y., A. K. Azad, A. J. Taylor, Q. X. Jia, and H. Chen. Influence of film thickness in THz active metamaterial devices: A comparison between superconductor and metal split-ring resonators. *Appl. Phys. Lett.*, 103(061117):1–5, 2013.
- [40] N. K. Grady, B. G. Perkins, H. Y. Hwang, N. C. Brandt, D. Torchinsky, R. Singh, L. Yan, D. Trugman, S. A. Trugman, Q. X. Jia, A. J. Taylor, K. A. Nelson, and H. Chen. Nonlinear high-temperature superconducting terahertz metamaterials. *New J. Phys.*, 15(105016):1–12, 2013.
- [41] S. M. Anlage, H. J. Snortland, and M. R. Beasley. A current controlled variable delay superconducting transmission-line. *IEEE Trans. Magn.*, 25(2):1388–1391, 1989.
- [42] C. Zhang, B. Jin, J. Han, I. Kawayama, H. Murakami, J. Wu, L. Kang, J. Chen, P. Wu, and M. Tonouchi. Terahertz nonlinear superconducting metamaterials. *Appl. Phys. Lett.*, 102(081121):1–4, 2013.
- [43] C. Zhang, B. Jin, J. Han, I. Kawayama, H. Murakami, X. Jia, L. Liang, L. Kang, J. Chen, P. Wu, and M. Tonouchi. Nonlinear response of superconducting NbN thin film and NbN metamaterial induced by intense terahertz pulses. *New J. Phys.*, 15(055017):1–17, 2013.
- [44] S. Tahara, S. M. Anlage, J. Halbritter, C. B. Eom, D. K. Fork, T. H. Geballe, and M. R. Beasley. Critical currents, pinning, and edge barriers in narrow $\text{YBa}_2\text{Cu}_3\text{O}_{7-\delta}$ thin-films. *Phys. Rev. B*, 41(16):11203–11208, 1990.
- [45] M. C. Ricci, H. Xu, R. Prozorov, A. P. Zhuravel, A. V. Ustinov, and S. M. Anlage. Tunability of superconducting metamaterials. *IEEE Trans. Appl. Supercond.*, 17(2):918–921, 2007.
- [46] B. Jin, C. Zhang, S. Engelbrecht, A. Pimenov, J. Wu, Q. Xu, C. Cao, J. Chen, W. Xu, L. Kang, and P. Wu. Low loss and magnetic field-tunable superconducting terahertz metamaterial. *Opt. Express*, 18(16):17504–17509, 2010.
- [47] C. Kurter, A. P. Zhuravel, J. Abrahams, C. L. Bennett, A. V. Ustinov, and S. M. Anlage. Superconducting RF metamaterials made with magnetically active planar spirals. *IEEE Trans. Appl. Supercond.*, 21(3):709–712, 2011.
- [48] C. Kurter, A. P. Zhuravel, A. V. Ustinov, and S. M. Anlage. Microscopic examination of hot spots giving rise to nonlinearity in superconducting resonators. *Phys. Rev. B*, 84(10):104515, 2011.
- [49] A. P. Zhuravel, C. Kurter, A. V. Ustinov, and S. M. Anlage. Unconventional rf photoresponse from a superconducting spiral resonator. *Phys. Rev. B*, 85(13):134535, 2012.
- [50] C. Du, H. Chen, and S. Li. Quantum left-handed metamaterial from superconducting quantum-interference devices. *Phys. Rev. B*, 74(11):113105, 2006.

- [51] N. Lazarides and G. P. Tsironis. rf superconducting quantum interference device metamaterials. *Appl. Phys. Lett.*, 90:163501, 2007.
- [52] J.-G. Caputo, I. Gabitov, and A.I. Maimistov. Electrodynamics of a split-ring Josephson resonator in a microwave line. *Phys. Rev. B*, 85(20):205446, 2012.
- [53] P. Jung, S. Butz, S. V. Shitov, and A. V. Ustinov. Low-loss tunable metamaterials using superconducting circuits with Josephson junctions. *Appl. Phys. Lett.*, 102(06):062601, 2013.
- [54] M. Trepanier, D. Zhang, O. Mukhanov, and S. M. Anlage. Realization and modeling of metamaterials made of rf superconducting quantum-interference devices. *Phys. Rev. X*, 3(04):041029, 2013.
- [55] S. Butz, P. Jung, L. V. Filippenko, V. P. Koshelets, and A. V. Ustinov. Protecting SQUID metamaterials against stray magnetic fields. *Supercond. Sci. Technol.*, 26(09):094004, 2013.
- [56] S. Butz, P. Jung, L. V. Filippenko, V. P. Koshelets, and A. V. Ustinov. A one-dimensional tunable magnetic metamaterial. *Opt Express*, 21(19):22540–8, Sep 2013.
- [57] P. Jung, S. Butz, M. Marthaler, M. V. Fistul, J. Leppäkangas, V. P. Koshelets, and A. V. Ustinov. Multistability and switching in a superconducting metamaterial. *Nat Commun*, 5:3730, 2014.
- [58] N. Lazarides and G. P. Tsironis. Multistability and self-organization in disordered SQUID metamaterials. *Supercond. Sci. Technol.*, 26(8):084006, 2013.
- [59] N. Lazarides and G.P. Tsironis. Driven linear modes: Analytical solutions for finite discrete systems. *Phys. Lett. A*, 374:2179–2182, 2010.
- [60] G. P. Tsironis, N. Lazarides, and I. Margaritis. Wide-band tuneability, nonlinear transmission, and dynamic multistability in SQUID metamaterials. *Appl. Phys. Lett.*, 117:579–588, 2014.
- [61] Nikos Lazarides and George P. Tsironis. Nonlinear localization in metamaterials. In *Nonlinear, Tunable and Active Metamaterials*, pages 281–301. Springer International Publishing, 2015.
- [62] N. Lazarides, G. Neofotistos, and G. P. Tsironis. Chimeras in squid metamaterials. *Phys. Rev. B*, 91(054303):1–8, 2015.
- [63] J. B. Pendry, A. J. Holden, W. J. Stewart, and I. Youngs. Extremely low frequency plasmons in metallic mesostructures. *Phys. Rev. Lett.*, 76(25):4773–4776, 1996.
- [64] R. M. Walser, A. P. Valanju, and P. M. Valanju. Comment on “Extremely low frequency plasmons in metallic mesostructures”. *Phys. Rev. Lett.*, 87:119701, Aug 2001.

- [65] M. C. Ricci. *Superconducting Artificial Materials with a Negative Permittivity, a Negative Permeability, or a Negative Index of Refraction*. PhD thesis, University of Maryland, 2007. <http://drum.lib.umd.edu/handle/1903/7176>.
- [66] D. R. Tilley. Superradiance in arrays of superconducting weak links. *Phys. Lett. A*, 33(4):205–206, 1970.
- [67] D. Rogovin and M. Scully. Superconductivity and macroscopic quantum phenomena. *Phys. Rep.*, 25(3):175–291, 1976.
- [68] J. A. Acebrón, L. L. Bonilla, C. J. Pérez Vicente, F. Ritort, and R. Spigler. The Kuramoto model: A simple paradigm for synchronization phenomena. *Rev. Mod. Phys.*, 77:137–185, 2005.
- [69] S. A. Marvel and S. H. Strogatz. Invariant submanifold for series arrays of Josephson junctions. *Chaos*, 19(1):013132, Mar 2009.
- [70] A. K. Jain, K. K. Likharev, J. E. Lukens, and J. E. Sauvageau. Mutual phase-locking in Josephson junction arrays. *Phys. Rep.*, 109(6):309–426, 1984.
- [71] S. P. Benz and C. J. Burroughs. Coherent emission from two-dimensional Josephson junction arrays. *Appl. Phys. Lett.*, 58(19):2162–2164, 1991.
- [72] P. Barbara, A. B. Cawthorne, S. V. Shitov, and C. J. Lobb. Stimulated emission and amplification in Josephson junction arrays. *Phys. Rev. Lett.*, 82(9):1963, 1999.
- [73] S. P. Benz, M. S. Rzchowski, M. Tinkham, and C. J. Lobb. Fractional giant Shapiro steps and spatially correlated phase motion in 2D Josephson arrays. *Phys. Rev. Lett.*, 64(6):693, 1990.
- [74] R. L. Kautz and R. Monaco. Survey of chaos in the rf-biased Josephson junction. *J. Appl. Phys.*, 57(3):875–889, 1985.
- [75] C. M. Falco. Phase-space of a driven, damped pendulum (Josephson weak link). *Am. J. Phys.*, 44:733, 1976.
- [76] E. W. Jacobs, A. R. Bulsara, and W. C. Schieve. Homoclinic and chaotic transitions in the rf SQUID. *Physica D: Nonlinear Phenomena*, 34(3):439–448, 1989.
- [77] D. R. Smith, D. C. Vier, W. Padilla, S. C. Nemat-Nasser, and S. Schultz. Loop-wire medium for investigating plasmons at microwave frequencies. *Appl. Phys. Lett.*, 75(10):1425–1427, 1999.
- [78] J.A. Acebrón and R. Spigler. Uncertainty in phase-frequency synchronization of large populations of globally coupled nonlinear oscillators. *Phys. D*, 141:65–79, 2000.

- [79] M. Marodi, F. d'Ovidio, and T. Vicsek. Synchronization of oscillators with long range interaction: Phase transition and anomalous finite size effects. *Phys. Rev. E*, 66:011109, 2002.
- [80] S. Shinomoto and Y. Kuramoto. Phase transitions in active rotator systems. *Progr. Theoret. Phys.*, 75(5):1105–1110, 1986.
- [81] J. A. Acebrón and R. Spigler. Adaptive frequency model for phase-frequency synchronization in large populations of globally coupled nonlinear oscillators. *Phys. Rev. Lett.*, 81(11):2229–2232, 1998.
- [82] B. Chesca. Theory of RF SQUIDs operating in the presence of large thermal fluctuations. *J. Low Temp. Phys.*, 110(516):963–1001, 1998.
- [83] S. Bermon and T. Gheewala. Moat-guarded Josephson SQUIDs. *IEEE Trans. Magn.*, 19(3):1160–1164, 1983.
- [84] Whiteley Research. <http://www.wrcad.com/>.
- [85] D. Yohannes, S. Sarwana, S. K. Tolpygo, A. Sahu, Y. A. Polyakov, and V. K. Semenov. Characterization of HYPRES' 4.5 kA/cm² & 8 kA/cm² Nb/AlO_x/Nb fabrication processes. *IEEE Trans. Appl. Supercond.*, 15(2):90–93, 2005.
- [86] D. Yohannes, A. Kirichenko, S. Sarwana, and S. K. Tolpygo. Parametric testing of HYPRES superconducting integrated circuit fabrication processes. *IEEE Trans. Appl. Supercond.*, 17(2):181–186, 2007.
- [87] S. K. Tolpygo and D. Amparo. Fabrication-process-induced variations of Nb/Al/AlO_x/Nb Josephson junctions in superconductor integrated circuits. *Supercond. Sci. Technol.*, 23(034024):1–9, 2010.
- [88] V. P. Koshelets, A. N. Matlashov, I. L. Serpuchenko, L. V. Filippenko, and Y. E. Zhuravlev. DC-SQUID preamplifier for DC-SQUID magnetometer. *IEEE Trans. Magn.*, 25(2):1182–1185, 1989.
- [89] V. P. Koshelets, S. A. Kovtonyuk, I. L. Serpuchenko, L. V. Filippenko, and A. V. Shchukin. High quality Nb-AlO_x-Nb junctions for microwave receivers and SFQ logic device. *IEEE Trans. Magn.*, 27(2):3141–3144, 1991.
- [90] P. N. Dmitriev, A. B. Ermakov, A. G. Kovalenko, V. P. Koshelets, N. N. Iosad, A. A. Golubov, and M. Y. Kupriyanov. Niobium tunnel junctions with multi-layered electrodes. *IEEE Trans. Appl. Supercond.*, 9(2):3970–3973, 1999.
- [91] L. V. Filippenko, S. V. Shitov, P. N. Dmitriev, A. B. Ermakov, V. P. Koshelets, and J.-R. Gao. Submillimeter superconducting integrated receivers: Fabrication and yield. *IEEE Trans. Appl. Supercond.*, 11(1):816–819, 2001.

- [92] P. N. Dmitriev, I. L. Lapitskaya, L. V. Filippenko, A. B. Ermakov, S. V. Shitov, G. V. Prokopenko, S. A. Kovtonyuk, and V. P. Koshelets. High quality Nb-based tunnel junctions for high frequency and digital applications. *IEEE Trans. Appl. Supercond.*, 13(2):107–110, 2003.
- [93] Coax. <http://www.coax.co.jp/>.
- [94] I.P. Nevirkovets, J. B. Ketterson, and J. M. Rowell. Modified superconductor-insulator-normal metal-insulator-superconductor Josephson junctions with high critical parameters. *J. Appl. Phys.*, 89(7):3980–3985, 2001.
- [95] D. Zhang, M. Trepanier, O. Mukhanov, and S. M. Anlage. Tunable broadband transparency of macroscopic quantum superconducting metamaterials. *arxiv:1504.08301*, 2015.
- [96] M. D. Reed, L. DiCarlo, B. R. Johnson, L. Sun, D. I. Schuster, L. Frunzio, and R. J. Schoelkopf. High-fidelity readout in circuit quantum electrodynamics using the Jaynes-Cummings nonlinearity. *Phys. Rev. Lett.*, 105(17):173601, 2010.
- [97] S. Novikov, J. E. Robinson, Z. K. Keane, B. Suri, F. C. Wellstood, and B. S. Palmer. Autler-Townes splitting in a three-dimensional transmon superconducting qubit. *Phys. Rev. B*, 88(6):060503, 2013.
- [98] L. S. Bishop, E. Ginossar, and S. M. Girvin. Response of the strongly driven Jaynes-Cummings oscillator. *Phys. Rev. Lett.*, 105(10):100505, 2010.
- [99] V. A. Fedotov, M. Rose, S. L. Prosvirnin, N. Papasimakis, and N. I. Zheludev. Sharp trapped-mode resonances in planar metamaterials with a broken structural symmetry. *Phys. Rev. Lett.*, 99(14):147401, 2007.
- [100] N. Papasimakis, V. A. Fedotov, N. I. Zheludev, and S. L. Prosvirnin. Metamaterial analog of electromagnetically induced transparency. *Phys. Rev. Lett.*, 101(25):253903, 2008.
- [101] P. Tassin, L. Zhang, T. Koschny, E. N. Economou, and C. M. Soukoulis. Low-loss metamaterials based on classical electromagnetically induced transparency. *Phys. Rev. Lett.*, 102:053901, 2009.
- [102] C. Kurter, P. Tassin, L. Zhang, T. Koschny, A. P. Zhuravel, A. V. Ustinov, S. M. Anlage, and C. M. Soukoulis. Classical analogue of electromagnetically induced transparency with a metal-superconductor hybrid metamaterial. *Phys. Rev. Lett.*, 107(4):043901, 2011.
- [103] C. Kurter, P. Tassin, A. P. Zhuravel, L. Zhang, T. Koschny, A. V. Ustinov, C. M. Soukoulis, and S. M. Anlage. Switching nonlinearity in a superconductor-enhanced metamaterial. *Appl. Phys. Lett.*, 100(12):121906–3, 2012.

- [104] A. A. Abdumalikov, O. Astafiev, A. M. Zagoskin, Y. A. Pashkin, Y. Nakamura, and J. S. Tsai. Electromagnetically induced transparency on a single artificial atom. *Phys. Rev. Lett.*, 104(19):193601, 2010.
- [105] O. Mukhanov, D. Gupta, A. Kadin, and V. Semenov. Superconductor analog-to-digital converters. *Proc. of the IEEE*, 92(10):1564–1584, 2004.
- [106] V. Savinov, A. Tsiatmas, A. R. Buckingham, V. A. Fedotov, P. A. J. de Groot, and N. I. Zheludev. Flux exclusion superconducting quantum metamaterial: towards quantum-level switching. *Sci Rep*, 2:450, 2012.
- [107] F. G. Paauw, A. Fedorov, C. J. P. M Harmans, and J. E. Mooij. Tuning the gap of a superconducting flux qubit. *Phys. Rev. Lett.*, 102(9):090501, 2009.
- [108] X. Zhu, A. Kemp, S. Saito, and K. Semba. Coherent operation of a gap-tunable flux qubit. *Appl. Phys. Lett.*, 97(10):102503, 2010.
- [109] V. A. Fedotov, N. Papasimakis, E. Plum, A. Bitzer, M. Walther, P. Kuo, D. P. Tsai, and N. I. Zheludev. Spectral collapse in ensembles of metamolecules. *Phys. Rev. Lett.*, 104(223901):1–4, 2010.
- [110] E. B. Wikborg, V. K. Semenov, and K. K. Likharev. RSFQ front-end for a software radio receiver. *IEEE Trans. Appl. Supercond.*, 9(2):3615–3618, 1999.
- [111] D. K. Brock, O. A. Mukhanov, and J. Rosa. Superconductor digital RF development for software radio. *IEEE Communications Mag.*, 39(2):174–179, 2001.
- [112] O. A. Mukhanov, D. Kirichenko, I. V. Vernik, T. V. Filippov, A. Kirichenko, R. Webber, V. Dotsenko, A. Talalaevskii, J. C. Tang, A. Sahu, P. Shevchenko, R. Miller, S. B. Kaplan, S. Sarwana, and D. Gupta. Superconductor digital-RF receiver systems. *IEICE Trans. Electron.*, E91-C(3):306–317, 2008.
- [113] J. Luine, L. Abelson, D. Brundrett, J. Burch, E. Dantsker, K. Hummer, G. Kerber, M. Wire, K. Yokoyama, D. Bowling, M. Neel, S. Hubbell, and K. Li. Application of a DC SQUID array amplifier to an electrically small active antenna. *IEEE Trans. Appl. Supercond.*, 9(2):4141–4144, 1999.
- [114] P. Caputo, J. Tomes, J. Oppenlaender, C. Haeussler, A. Friesch, T. Traeuble, and N. Schopohl. Two-tone response in superconducting quantum interference filters. *IEEE Trans. Appl. Supercond.*, 17(2):722–725, 2007.
- [115] V. Kornev, I. I. Soloviev, N. V. Klenov, A. V. Sharafiev, and O. A. Mukhanov. Array designs for active electrically small superconductive antennas. *Physica C*, 479:119–122, 2012.
- [116] V. K. Kornev, I. I. Soloviev, A. V. Sharafiev, N. V. Klenov, and O. A. Mukhanov. Active electrically small antenna based on superconducting quantum array. *IEEE Trans. Appl. Supercond.*, 23(3):1800405, 2013.

- [117] O. V. Snigirev, M. L. Chukharkin, A. S. Kalabukhov, M. A. Tarasov, A. A. Deleniv, O. A. Mukhanov, and D. Winkler. Superconducting quantum interference filters as RF amplifiers. *IEEE Trans. Appl. Supercond.*, 17(2):718–721, 2007.
- [118] V. K. Kornev, I. I. Soloviev, N. V. Klenov, and O. A. Mukhanov. High-linearity SQIF-like Josephson-junction structures. *IEEE Trans. Appl. Supercond.*, 19(3):741–744, 2009.
- [119] M. A. Castellanos-Beltran, K. D. Irwin, G. C. Hilton, L. R. Vale, and K. W. Lehnert. Amplification and squeezing of quantum noise with a tunable Josephson metamaterial. *Nat Phys.*, 4:929–931, 2008.
- [120] J.T. Jeng, H. C. Hung, C. R. Lin, C.H. Wu, K.L. Chen, J.C. Chen, H.C. Yang, S.H. Liao, and H.E. Horng. Flux-to-voltage transfer function of the series-SQUID array with grain-boundary Josephson junctions. *IEEE Trans. Appl. Supercond.*, 15(2):793–796, 2005.
- [121] A.C. Bruno, M.A. Espy, D. D. Clark, A.N. Matlashov, and R.H. Kraus Jr. Digital spatial filter made from a squid array. *IEEE Trans. Appl. Supercond.*, 13(2):779–782, 2003.
- [122] J. Oppenlander, Ch. Haussler, T. Trauble, P. Caputo, J. Tomes, A. Friesch, and N. Schopohl. Two dimensional superconducting quantum interference filters. *IEEE Trans. Appl. Supercond.*, 13(2):771–774, 2003.
- [123] A. Blais, R.-S. Huang, A. Wallraff, S. M. Girvin, and R. J. Schoelkopf. Cavity quantum electrodynamics for superconducting electrical circuits: An architecture for quantum computation. *Phys. Rev. A*, 69(6):062320, 2004.
- [124] J. Clarke and F. K. Wilhelm. Superconducting quantum bits. *Nature*, 453(7198):1031–1042, 06 2008.
- [125] J. Q. You and F. Nori. Atomic physics and quantum optics using superconducting circuits. *Nature*, 474(7353):589–597, 06 2011.
- [126] P. Macha, G. Oelsner, J.-M. Reiner, M. Marthaler, S. André, G. Schön, U. Hübner, H.-G. Meyer, E. Il'ichev, and A. V. Ustinov. Implementation of a quantum metamaterial using superconducting qubits. *Nat Commun*, 5, 2014.
- [127] B. Peropadre, G. Romero, G. Johansson, C. M. Wilson, E. Solano, and J. J. García-Ripoll. Approaching perfect microwave photodetection in circuit QED. *Phys. Rev. A*, 84(6):063834, 2011.
- [128] Y.-F. Chen, D. Hover, S. Sendelbach, L. Maurer, S. T. Merkel, E. J. Pritchett, F. K. Wilhelm, and R. McDermott. Microwave photon counter based on Josephson junctions. *Phys. Rev. Lett.*, 107(21):217401, 2011.

- [129] O. V. Astafiev, L. B. Ioffe, S. Kafanov, Y. A. Pashkin, K. Y. Arutyunov, D. Shahar, O. Cohen, and J. S. Tsai. Coherent quantum phase slip. *Nature*, 484(7394):355–358, 2012.
- [130] A. Ergül, J. Lidmar, J. Johansson, Y. Azizoglu, D. Schaeffer, and D. B. Haviland. Localizing quantum phase slips in one-dimensional Josephson junction chains. *New J. Phys.*, 15(9):095014, 2013.
- [131] M. T. Bell, I. A. Sadovskyy, L. B. Ioffe, A. Y. Kitaev, and M. E. Gershenson. Quantum superinductor with tunable nonlinearity. *Phys. Rev. Lett.*, 109(13):137003, 2012.
- [132] A. L. Rakhmanov, A. M. Zagoskin, S. Savel’ev, and F. Nori. Quantum metamaterials: Electromagnetic waves in a Josephson qubit line. *Phys. Rev. B*, 77(14):144507, 2008.
- [133] H. Asai, S. Savel’ev, S. Kawabata, and A. M. Zagoskin. Effects of lasing in a one-dimensional quantum metamaterial. *Phys. Rev. B*, 91(13):134513, 2015.
- [134] A. A. Babaei Brojeny and J. R. Clem. Magnetic-field and current-density distributions in thin-film superconducting rings and disks. *Phys. Rev. B*, 68(174514):1–9, 2003.
- [135] R. Meservey and P. M. Tedrow. Measurements of the kinetic inductance of superconducting linear structures. *J. Appl. Phys.*, 40(5):2028–2034, 1969.

MELISSA TREPANIER

34 Sarah Dr. ◊ Merrimack, NH 03054

(603)913-5613 ◊ mctrep@umd.edu

EDUCATION

University of Maryland, College Park 2011 - 2015
Ph.D in Physics: GPA 3.41
Rochester Institute of Technology 2007 - 2011
B.S. in Physics: GPA 3.94

RESEARCH EXPERIENCE

Graduate Research Assistant 2012 - 2015
Steven M. Anlage *University of Maryland, College Park*

- Design, model, and perform low-temperature microwave measurements on tunable non-linear superconducting Josephson junction metamaterials (rf SQUIDs and Josephson-junction loaded wire arrays)

Undergraduate Research Assistant 2010-2011
Linda Barton *Rochester Institute of Technology*

- Produced Heusler alloys and performed four-point resistance measurements as a function of temperature to determine their Curie temperatures

Undergraduate Research Assistant 2010
Rena Zieve *University of California, Davis*

- Performed resistance measurements on CaFe_2As_2 as a function of temperature and uniaxial pressure to observe the material's phase transition.

Undergraduate Research Assistant 2009
Scott V. Franklin *Rochester Institute of Technology*

- Studied the collapse of granular columns as a function of particle aspect ratio. I built the experimental setup, performed the measurements, and analyzed the data.

Undergraduate Research Assistant 2007-2008
Jacob Noel-Storr *Rochester Institute of Technology*

- Performed image processing on infrared data from Spitzer space telescope

SKILLS

Computing: Matlab, Mathematica, Python, HFSS, AutoCAD, Fortran, C, LabView, Deepthought: high performance computing cluster

microwave measurement techniques; vacuum and low temperature techniques

PUBLICATIONS

M. Trepanier, D. Zhang, O. Mukhanov, and S. M. Anlage. “Realization and modeling of metamaterials made of rf superconducting quantum-interference devices.” *Phys. Rev. X*, 3(04):041029, 2013.

M. Trepanier and S. V. Franklin. “Column collapse of granular rods.” *Phys. Rev. E*, 82(01):011308, 2010.

CONTRIBUTED TALKS AND POSTERS

American Physical Society March Meeting San Antonio, TX 2015, Meta-Atom Interactions and Coherent Response in rf SQUID Metamaterials, session L36.012

Metamaterials Copenhagen, Denmark 2014, Coherence in rf SQUID Metamaterials, session Exotic effects

Applied Superconductivity Conference Charlotte, NC 2014, Intermodulation of nonlinear rf-SQUID metamaterials, session 3EPo1B-02 14 & 15 (*invited*)

American Physical Society March Meeting Baltimore, MD 2014, Meta-Atom Interactions and Coherent Response in RF SQUID Metamaterials, session L50.009

American Physical Society March Meeting Denver, CO 2013, Design of Tunable Superconducting Metamaterials, session A20.009

American Physical Society March Meeting Portland, OR 2010, Column Collapse of Rod-like Granular Materials, session L12.013

American Physical Society Division of Fluid Dynamics Meeting Minneapolis, MN 2009, Column Collapse of Rod-like Granular Materials, session BU.00010